NOVA SCHOOL OF SCIENCE & TECHNOLOGY

DEPARTAMENT OF MATERIALS SCIENCE

Daniela Roque Tomé

BSc in Micro and Nanotechnology Engineering

# SHAPE PROGRAMMING OF LIQUID CRYSTAL ELASTOMERS BY TWO-STAGE WAVELENGTH-SELECTIVE PHOTO-POLYMERISATION

MASTER IN MICRO AND NANOTECHNOLOGY ENGINEERING

NOVA University Lisbon

September, 2024

NOVA SCHOOL OF SCIENCE & TECHNOLOGY

DEPARTAMENT OF MATERIALS SCIENCE

# SHAPE PROGRAMMING OF LIQUID CRYSTAL ELASTOMERS BY TWO-STAGE WAVELENGTH-SELECTIVE PHOTOPOLYMERISATION

**Daniela Roque Tomé**

BSc in Micro and Nanotechnology Engineering

**Adviser:** Danqing Liu
Associate Professor, Eindhoven University of Technology

**Co-advisers:** Maria Helena Godinho
Associate Professor, NOVA University Lisbon

Tom Bruining
PhD Candidate, Eindhoven University of Technology

**Examination Committee:**

**Chair:** Hugo Manuel Brito Águas
Associate Professor, NOVA University Lisbon

**Rapporteur:** Dirk Jan Broer
Full Professor, Eindhoven University of Technology

**Advisers:** Danqing Liu
Associate Professor, Eindhoven University of Technology

Maria Helena Godinho
Associate Professor, NOVA University Lisbon

MASTER IN MICRO AND NANOTECHNOLOGY ENGINEERING

NOVA University Lisbon
September, 2024

**Shape Programming of Liquid Crystal Elastomers by Two-Stage Wavelength-Selective Photo-Polymerisation**

Dedico esta tese aos meus familiares e amigos próximos.

# ACKNOWLEDGMENTS

Firstly, I would like to express my sincere gratitude to Prof. Dr. Danqing Liu for your unwavering support and the invaluable discussions we shared throughout my research. Most of all, I am grateful to you for entrusting me with this project, which was highly enriching and allowed me to learn far more than I could've ever predicted. From jumping headfirst into the intricacies of liquid crystal polymer science and learning such a variety of processing and characterisation techniques, to writing a scientific paper, as well as a patent, none of it would have been possible if I were not given this opportunity, and for that I am forever thankful.

I am deeply thankful to PhD candidate Tom Bruining. Your guidance was indispensable for this research. If I had such a great experience during this project, it was mostly thanks to you. Your knowledge, open-mindedness, lack of judgement, and trust in me motivated me to work harder and surpass myself at every turn. As a great chemist yourself, thank you for always taking the time to explain and clarify any doubts I might have had. It was honestly a pleasure working with you on this project.

Gostaria de exprimir a minha gratidão para com a Prof. Dr. Maria Helena Godinho que apesar de não ter acompanho o desenrolar do projeto de perto, foi uma voz crítica e construtiva no aperfeiçoamento desta dissertação de mestrado.

I thank post-doctoral researcher Dr. Quentin Lahondes for coaching me through the 4D printing process, from helping me optimise and become more efficient at computer-assisted design (CAD) to learning how to work with open-loop machines like the Hyrel 3D printer. My ability to print successfully in such a short period of time would not have been possible without your teachings.

I extend my gratitude to Prof. Dr. Dick Broer for sharing with me a small portion of your vast knowledge of liquid crystals. I want to thank you for your insightful lectures and discussions, I was able to learn a great deal from them.

I would like to thank PhD candidate Pengrong Lyu for performing the XRD measurements and PhD candidate Henk Sentjens for carrying out the GPC measurements. As well as PhD candidate Duygu Polat for all the equipment instructions.

I want to express my heartfelt appreciation to everyone from the HIM and SFD groups. I am thankful for the excellent working environment provided by all of you. Listening to your knowledge and experiences opened my horizons and taught me a lot.

I would like to extend my gratitude to the members of the jury committee Prof. Dr. Hugo Águas, Prof. Dr. Dick Broer, Prof. Dr. Danqing Liu, and Prof. Dr. Maria Helena Godinho for their valuable time and insightful feedback.

This work was financed by national funds from FCT - Fundação para a Ciência e a Tecnologia, I.P., in the scope of the projects LA/P/0037/2020, UIDP/50025/2020 and UIDB/50025/2020 of the Associate Laboratory Institute of Nanostructures, Nanomodelling and Nanofabrication – i3N). Moreover, this research was also part of the research program financed by the Dutch Research Council (NWO) (OTP 19440 and Gravity Program 024.005.020 – Interactive Polymer Materials IPM).

I am grateful to the Eindhoven University of Technology (TU/e), particularly the Department of Chemical Engineering and Chemistry, for providing the facilities and resources needed to conduct this research.

I thank NOVA School of Science and Technology | FCT NOVA for being my academic home these last five years. I want to extend my gratitude to every professor and researcher who played a role in enriching my education. I specifically would like to express my appreciation to the Department of Materials Science for incentivising us students to search for these types of international research opportunities.

I shall also acknowledge the crucial role my Erasmus + scholarship provided in terms of financial support for living in a foreign and more expensive country. I am tremendously grateful to the European Union (EU) for funding endeavours that contribute to the active transfer of knowledge from diverse parts of the continent.

I am grateful to all my friends, especially those I met during my academic journey. Thank you for filling my days with sunshine with our jokes and being there for me on my rainy moments. Without you, it wouldn't have been the same thing.

Quero também expressar a minha gratidão ao meu namorado. Obrigada por todo o teu apoio e paciência comigo. A força que me deste ajudou-me a não só completar este percurso universitário com sucesso, como também aproveitá-lo ao máximo.

Por último, mas não menos importante, quero agradecer aos meus pais por todo o apoio que sempre me deram no decorrer do meu percurso académico e não só. O vosso apoio e encorajamento constante tornam-me numa versão melhor de mim mesma cada dia.

"The good thing about science is that it's true whether or not you believe it."
(Neil deGrasse Tyson)

# MOTIVATION

First introduced in 1975 by P. G. de Gennes [1], liquid crystal elastomers (LCEs) are a class of smart soft active polymers consisting of an elastomeric network in which self-organising mesogenic groups are incorporated. Thus, combining liquid-crystalline (LC) order and entropy elasticity properties. Therefore, when under external stimulus, LCEs exhibit outstanding mechanical and optical reversible actuation [2], [3]. LCEs have taken centre stage in a plenitude of technologies, such as mechanical actuators and sensors [4], [5], dynamic surfaces [6], soft-robotics [7], haptics [2], tissue engineering [8], and micro-electromechanical systems (MEMS) [9], among others. For the relevancy of this work, only thermal actuation will be discussed at length. For this, an LC monodomain must be created by uniformly aligning the mesogens along a selected orientation. If sufficiently heated, the LC monodomain will undergo a nematic-to-isotropic phase transition ($T_{NI}$) to decrease the system's free energy [10], resulting in the material's actuation [11]. The most widely used methods to permanently program a monodomain tend to involve a multi-step process [12]. Such is the case with the popular two-stage thiol–acrylate Michael addition and photo-polymerisation (TAMAP) reaction developed by Yakacki *et al*. [13]. TAMAP uses a thiol–acrylate "click" reaction to partially crosslink the LC polydomain into a gel-like state, which is then aligned into a monodomain. Followed by a photo-polymerisation reaction based on the excess acrylate groups remaining unreacted in the first step. This second crosslinking step stabilises the monodomain. This method is not without its flaws. The thiol–acrylate "click" reaction uses a base catalyst, which initiates the reaction as soon as it is introduced to the solution. This is a major disadvantage of this procedure, heavily limiting the time for manoeuvring of the solution before initial crosslinking. Thus, making this method unsuitable for large-scale production and restricting its applicability for multiple coating techniques. Moreover, if the reaction rate exceeds the solvent evaporation rate, another issue might emerge, as the trapping of solvent could lead to irregularities in the LCE film. As an alternative, in this work a two-step wavelength-selective photo-polymerisation (TWSP) reaction is proposed. In this new procedure, the first crosslinking step is done by free-radical polymerisation of acrylates under blue light (400-450 nm) [14] irradiation above $T_{NI}$. Next, the pre-LCE film is aligned below $T_{NI}$. Then, the film, still below $T_{NI}$, is illuminated with ultraviolet (UV) light (< 400 nm) [15], which photo-initiates a cationic ring-opening polymerisation of oxetanes. In the end, a permanently programmed monodomain LCE film capable of large and reversible "hands-free" actuation under thermal stimulus is obtained. The photo nature of this methodology allows for greater spatio-temporal control over both crosslinking steps. Distinguishing this new approach for its remarkable capability of influencing LC behaviour. The simplicity, lack of time-dependency, and scalability of this procedure make it a promising and superior choice for synthesising and programming LCEs.

# ABSTRACT

The stimulus responsiveness properties of liquid crystal elastomers (LCEs) make them prime candidates for actuator applications. Nevertheless, most LCE fabrication methods show critical limitations, such as time-dependency and lack of control due to catalyst-based reactions. This work proposes a novel two-step wavelength-selective photo-polymerisation (TWSP) reaction to synthesise and program thermo-responsive LCEs. By harnessing the power of two photo-initiated reactions, this method provides a higher tailorability control over the LCEs during both crosslinking stages. The independent conversion of ~ 88% acrylates and ~ 26% oxetanes in two separate sequential photo-polymerisation reactions was demonstrated. The LCEs made by TWSP were capable of actuating reversibly over multiple cycles of heating and cooling. It was observed that different alignments can be effectively programmed. Moreover, the usage of different mesogens was viable and led to changes in the LCEs' properties. For instance, RM82-based stretched films suffered a 35.32% strain variation across a 57 ºC window, while C6BAPE-based ones showed a smaller variation of 17.39%, but within a more restricted range of 20 ºC. These contraction-based LCEs were found to be capable of lifting a weight 488.81 times heavier than the film itself. A one-pot approach implementation in TWSP showed promise for surface-switching applications but not for making free-standing films due to lower elasticity. Additionally, the TWSP integration with 4D printing was explored with the goal of programming more complex alignments and investigating the possibility of programming alignment in both crosslinking stages. The alignment from printing was found to be sufficient for actuation. However, a second programming in the alignment direction increased the order parameter, resulting in a larger actuation and sharper transition of the LCEs. Conversely, a second programming in the perpendicular direction to the alignment led the film to actuate from flat to a tunnel-like shape due to the competing alignments.

**Keywords**: liquid crystal elastomers (LCEs), reactive mesogen, alignment, photo-polymerisation, shape memory, reversible actuation.

# RESUMO

Os elastómeros líquidos cristalinos (LCEs) distinguem-se pelas suas propriedades de resposta a estímulos, tornando-os promissores candidatos a atuadores. Contudo, muitos dos métodos de fabrico de LCEs apresentam limitações como a dependência do tempo e o reduzido controlo associado a reações com catalisadores. Este trabalho propõe uma inovadora reação de dois passos para a síntese e programação de LCEs termicamente responsivos, designada foto-polimerização seletiva de comprimento de onda (TWSP). A integração destas reações foto-iniciadas confere a este método maior controlo e manipulação das propriedades dos LCEs durante ambas as fases de reticulação. Observou-se a conversão independente de ~ 88% de acrilatos e ~ 26% de oxetanos em duas reações de foto-polimerização sequenciais separadas. Os LCEs fabricados por TWSP atuaram reversivelmente em múltiplos ciclos de aquecimento e arrefecimento. Diferentes alinhamentos foram programados eficazmente. A utilização de mesogéneos distintos resultou em alterações nas propriedades dos LCEs. Nomeadamente, os filmes esticados à base de RM82 demonstraram 35.32% de variação de forma (deformação) numa janela de 57 ºC, enquanto os filmes à base de C6BAPE atuaram apenas 17.39%, mas numa gama mais restrita de 20 ºC. Ao contrair os LCEs levantaram um peso 488.81 vezes superior ao peso do próprio filme. Combinar a abordagem *one-pot* com o TWSP mostrou-se favorável para aplicações em comutação de superfície, mas não para o fabrico de filmes soltos devido à sua menor elasticidade. Explorou-se a integração do TWSP com a impressão 4D visando programar alinhamentos mais complexos e em ambas as etapas de reticulação. Confirmou-se que o alinhamento por impressão é suficiente para ocorrer atuação. Porém, uma segunda programação no sentido do alinhamento da impressão aumentou o parâmetro de ordem, resultando numa maior atuação dos LCEs. Todavia, uma segunda programação na direção perpendicular ao alinhamento da impressão cria alinhamentos concorrentes levando à atuação do filme em formas mais complexas.

**Palavras chave:** elastómeros liquídos cristalinos (LCEs), mesogéneo reativo, alinhamento, foto-polimerização, memória de forma, atuação reversível.

# CONTENTS

# LIST OF FIGURES

# LIST OF TABLES

# GLOSSARY

**Polymers** A class of materials, of synthetic or natural origin, comprised of very large molecules, called macromolecules, which are linked together into chains by repeating subunits of much simpler chemistry, designated as monomers [16], [17].

**Monomers** A type of small molecules which have the ability to bond together in a repeating pattern to form more complex structures, such as oligomers or polymers [18], [19].

**Mesogen** Rigid rod or disc-like molecule or molecular segment that composes liquid crystal materials [20].

**Entropy** Degree of disorder in a thermodynamic system. In other words, it indicates the unavailability of the thermal energy in the system to be converted into mechanical work [21].

**Actuator** Material or device that in response to an external stimulus exerts mechanical work. In other works, it can convert an input energy (*e.g.*, temperature, electricity, light, air, water, *etc*) into physical movement [22].

**Polydomain** Comprised of two or more domains.

**Monodomain** Composed of just one domain.

**Free energy** The energetic capacity available in a system to perform work [23].

**Wettability** Ability of a liquid to remain in contact with a solid surface. This phenomenon is ruled by the equilibrium reached between cohesive- (liquid-to-liquid) and adhesive-type (liquid-to-solid) molecular interactions [24].

**Anisotropic** A material/molecule which shows variations in physical properties (*e.g.*, geometry) along distinct directions in space (or different molecular axes) [25].

**Mesophases** A phase that occurs across a specific range of temperature, concentration, or pressure within the mesomorphic state (intermediate state between the liquid and crystal states) [26].

# ACRONYMS

| | |
|---|---|
| **LCE** | Liquid crystal elastomer |
| **LC** | Liquid crystal |
| **MEMS** | Micro-electromechanical systems |
| **TAMAP** | Two-stage thiol-acrylate Micheal addition and photo-polymerisation |
| **TWSP** | Two-step wavelength-selective photo-polymerisation |
| **UV** | Ultraviolet |
| **RM82** | 1,4-Bis[4-(6-acryloyloxyhexyloxy)benzoyloxy]-2-methylbenzene |
| **DODT** | 2,2′-(Ethylenedioxy)diethanethiol |
| **C6BAPE** | 4-(6-(acryloyloxy)hexyloxy)phenyl-4-(6-(acryloyloxy)hexyloxy)benzoate |
| **DBU** | 1,8-Diazabicyclo[5.4.0]undec-7-ene |
| **DCM** | Dichloromethane |
| **RT** | Room temperature |
| **THPS** | Triarylsulfonium hexafluorophosphate salts |
| **DP** | Degree of polymerisation |
| **$^1$H-NMR** | Proton nuclear magnetic resonance |
| **GPC** | Gel permeation chromatography |
| **PDI** | Polydispersity index |
| **THF** | Tetrahydrofuran |
| **PDA** | Polydopamine |
| **DSC** | Differential scanning calorimetry |
| **UV-vis** | Ultraviolet-visible spectroscopy |
| **FTIR** | Fourier-transform infrared spectroscopy |
| **DMA** | Dynamic mechanical analysis |
| **POM** | Polarised light microscopy |
| **2D, 3D, 4D** | Two, three, four dimensional |
| **Endo** | Endothermal |
| **Exo** | Exothermal |

| | |
|---|---|
| **LED** | Light-emitting diode |
| **CAD** | Computer-aided design |
| **TEA** | Triethylamine |
| ***olgRM82-1*** | First synthesised oligomer in this work with RM82 as the reactive mesogen |
| ***olgRM82-2*** | Second synthesised oligomer in this work with RM82 as the reactive mesogen |
| ***olgRM82-3*** | Third synthesised oligomer in this work with RM82 as the reactive mesogen |
| ***olgC6BAPE-1*** | Oligomer synthesised in this work with C6BAPE as the reactive mesogen |
| ***ref*** | Stretched LCE sample made with the *olgRM82-2* oligomer, with a 17.9 wt. % crosslinker concentration |
| ***CC11.7wt%*** | Stretched LCE sample made with the *olgRM82-2* oligomer, with a 11.7 wt. % crosslinker concentration |
| ***CC4.3wt%*** | Stretched LCE sample made with the *olgRM82-2* oligomer, with a 4.3 wt. % crosslinker concentration |
| ***TAMAP*** | Stretched LCE sample synthesised and programmed through the TAMAP method |
| ***4DP-1*** | 4D printed LCE sample which was not stretched and fully crosslinked with just the alignment from printing |
| ***4DP-2*** | 4D printed LCE sample which was aligned twice in the same direction (*i.e.,* aligned once by printing and then again though stretching in the same direction) |
| ***4DP-3*** | 4D printed LCE sample which was aligned twice but in perpendicular direction (*i.e.,* aligned once by printing and then again though stretching in the perpendicular direction) |

# SYMBOLS

| | |
|---|---|
| **n** | Director – molecular direction in which the liquid crystal molecules prefer to orient [20]. |
| **S** | Order Parameter – quantifies the degree of order of the system. In other words, it represents the statistical average determined taking into consideration the orientational distribution, meaning the likelihood of a LC molecule to adopt a particular orientation, *i.e.,* director (n) [27]. |
| **O** | Oxygen atom |
| **$O_2$** | Oxygen molecule |
| **$N_2$** | Nitrogen molecule |
| **C** | Carbon atom |
| **H** | Hydrogen atom |
| **π** | Ratio of the circle's circumference to its diameter. Equal to 3.14159265 when rounded to eight places of decimal [28]. |
| **Mn** | Number-averaged molecular weight |
| **Mw** | Weight-averaged molecular weight |
| **$T_g$** | Glass transition temperature |
| **$T_{SN}$** | Smectic-to-nematic transition temperature |
| **$T_{NI}$** | Nematic-to-isotropic transition temperature |
| **G′** | Storage modulus |
| **G″** | Loss modulus |
| **tanδ** | Tan delta |
| **ζ** | Damping ratio |
| $\boldsymbol{\phi}$ | Diameter of the nozzle |
| $\boldsymbol{x}$ | Spacing between the printed lines |
| **$M_{DODT}$** | Molecular mass of DODT |
| $\boldsymbol{I}$ | Intensity |
| $\boldsymbol{\phi}$ | Azimuthal angle |

# 1

# INTRODUCTION

## 1.1 Surface Topographies Dynamics & Shape Memory

Various millenniums have passed since life first emerged on Earth. Natural selection led to the extinction of many living creatures, while others thrived and evolved until the contemporary age. To do so, the more fragile and weak beings underwent multiple evolutions in order to reduce or mask their vulnerabilities from predators. This granted each individual organism adaptive characteristics that best suited its ecosystem. This has filled nature with a variety of unique surfaces made up of distinctive topographic patterns. The dynamism of the surface topographies differs significantly from species to species [29], [30]. Mammals, for instance, tend to present surfaces consisting of more dynamic structures, such as the Pilomotor Reflex on their skin, which acts both as a way for thermal isolation, as well as protection from predators by the illusion of a larger body [31]. On the other hand, the unique static motifs found on the surface of the leaves of the lotus flower give it water- and dirt-repellent properties, thereby conditioning the surface's wettability and making the plant impermeable [32]. For decades, researchers have been replicating these natural phenomena by conceptualising innovative architectures for surface topologies, which are then brought to life with materials whose properties better suit the desired surface characteristics. In recent years, the growing demand for flexibility, controllability, and reliability in next-generation actuation devices has brought soft active materials to the forefront of materials science research [3], [30], [33].

## 1.2 Mechanics of Liquid Crystal (LC) Polymers

### 1.2.1 Background on the Basics of Liquid Crystals (LCs)

Liquid crystals (LC), as the name implies, are a class of materials which possess mesophases, *i.e.*, states of matter intermediate between a solid crystal and an isotropic liquid. As such, they are characterised by exhibiting anisotropy in optical, electric, and magnetic properties similar to crystals and the high fluidity of liquids [34], [35]. In other words, the molecules that compose an LC material show a degree of long-range orientational order along a selected direction, whose unit vector is commonly referred to as the director (n), instead of randomly oriented molecules like a standard liquid would [1]. LC molecules, known as mesogens, are comprised in average of two to three aromatic rings bound together, making up the rigid backbone core of the molecule, and flexible ends in the form of aliphatic carbon chains. This means that mesogens are always anisotropic, regardless of what specific molecular type they belong to. Mesogens show a tendency for self-organisation. This molecular level affinity

is responsible for the order that emerges in LCs even while in a fluid-like state [36]. LC molecules can be categorised into three main types: calamitic, discotic, or bent-core (Figure 1 (A)). Amongst these, calamitic molecules stand out as the most employed type. These are rod-shaped molecules, meaning their anisotropy comes from the length of one molecular axis being greater than the other two [37]. There are essentially two main types of LC mesophases: nematic and smectic. Although in these there can be other sub-phases, such as, for example, cholesteric (chiral nematic), or ferronematic, or smectic A or C, among others. Some LC materials can possess both smectic and nematic mesophases, while others only exhibit a nematic phase. Perhaps for this reason, the nematic phase tends to be the most used and studied. In this phase, mesogens show long-range orientational order but only positional order in the short-range [1], [36], [38]. A vital characterisation parameter for any LC material is the isotropization temperature, which for a nematic is the transition temperature from the nematic to the isotropic phase ($T_{NI}$). LC materials are only in their mesophase state under certain conditions, which are material-specific. Depending on which stimuli lead to phase transition in an LC, that is, which parameter influences the material's order, it can be categorised thermodynamically as: thermotropic (temperature-dependent), lyotropic (dependent on the material's concentration in solution), or phototropic (light-dependent) [37], [39], [40]. In thermotropic LCs, which are of higher relevance for this work, the material undergoes phase transitions with increasing temperature, resulting in the material's order reduction [12]. Figure 1 (B) illustrates these phase transitions. Starting from a solid crystal, where the order parameter (S) is at its highest value (S=1). Then, transitioning to a mesophase, with lower S. Depending on the material type, more than one mesophase might be present at different temperatures since some LC phases are more ordered than others. Finally, above the $T_{NI}$ the material will go to the more fluid and least ordered (S=0) isotropic state.

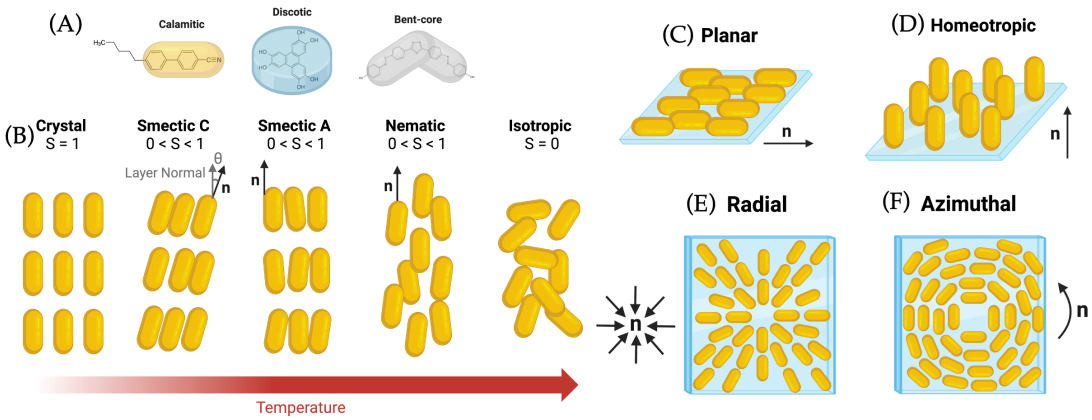


Figure 1 – (A) Main types of LC molecules. (B) Illustration of the phase changes of an LC material under temperature variation. Types of alignment of LC mesogens: (C) planar, (D) homeotropic, (E) radial, and (F) azimuthal.

For further tailoring of LC properties, alignment and surface treatment strategies are commonly employed during the fabrication process. Figure 1 (C) and (D) show the mesogens oriented parallel (planar) or perpendicular (homeotropic) relative to the surface [12], [41]. Planar or homeotropic orientation can be propagated through the film's thickness, or there can be some variations, for example, splay or twisted nematic deformations. These are achieved

by different types of anchoring on two separate surfaces. In the case of a splay alignment, the molecules are anchored homeotropically relative to one surface and planar towards the other. Twisted nematic alignment results from the 90º rotation of one surface relative to the other, but the anchoring orientation in both is the same. Alignment types are not limited to the aforementioned examples. In more complex systems like LCE networks, more intricate alignments can be made, *e.g.,* radial or azimuthal (Figure 1 (E) and (F)) [12], [41].

### 1.2.2 Liquid Crystal Elastomers (LCEs)

First introduced in 1975 by P. G. de Gennes [1], liquid crystal elastomers (LCEs) are a class of smart soft active polymers consisting of an elastomeric network in which self-organising mesogenic groups are incorporated. Thus, combining properties of entropy elasticity and liquid-crystalline (LC) order. When under external stimulus (*e.g.,* heat, light, electric or magnetic field), as a result of these aforementioned properties, LCEs exhibit outstanding reversible actuation, both mechanically (*e.g.,* shape-change and -memory, rubber elasticity, high uniaxial/biaxial actuation strains) and optically (*e.g.,* switchable transparency) [2], [3]. This has brought this class of materials to the forefront of today's materials science research. Thus, LCEs' integration into a plenitude of technologies has been investigated. Some of the most prominent fields include mechanical actuators and sensors [4], [5], dynamic surfaces [6], soft-robotics [7], haptics [2], tissue engineering [8], and micro-electromechanical systems (MEMS) [9], among many others. As stated previously, actuation is dependent on the external stimulus. As such, for the relevancy of this work, only thermal actuation will be discussed at length. For this, an LC monodomain (*i.e.,* anisotropic mesophase) must be created by uniformly aligning the mesogens along a selected orientation, *i.e.,* the director (n). If sufficiently heated, the LC monodomain will undergo a nematic to isotropic phase transition ($T_{NI}$) to decrease the system's free energy [10], resulting in the material's actuation [11].

## 1.3 LCEs Fabrication Strategies

Multiple strategies, such as surface anchoring in a cell or field-assisted alignment, can be used to permanently program a monodomain in the polymeric network. Nevertheless, the most commonly employed methods tend to involve a multi-step process [12].

### 1.3.1 Physics and Chemistry of Photo-polymerisation Reactions

A common feature across these multi-step procedures is the inclusion of at least one photo-polymerisation step. Photo-polymerization reactions offer numerous advantages, including fast cure times, low energy consumption, and precise spatio-temporal control over the polymer's properties [42], [43]. Therefore, a brief introduction to the physics and chemistry of photo-polymerisation reactions is warranted. Free-radical photo-polymerisation reactions are the mainstream choice across the majority of the literature. This polymerisation type can be subdivided into three crucial stages: (i) initiation, (ii) propagation, and (iii) termination. Figure

2 (A) illustrates the chemical interactions that characterise these first two steps. The initiation stage consists of the photo-dissociation of the initiator into radicals when exposed to a wavelength of light in its absorption range. These first radicals, due to their inherent highly unstable nature, will break the carbon-carbon double bonds (C=C) at the tails of the monomers (*e.g.*, acrylate groups) in order to bind to them. Next, by chain-addition and -transfer, the reaction will continue to form the polymer chain. Note that this happens in multiple monomers at once. These simultaneous rapid reactions lead to the extension of the polymer chain. This stage is designated as propagation. Finally, in the termination step, the radicals are inactivated. This inactivation can occur due to multiple phenomena. For instance, due to the recombination of two radicals with each other. Or alternatively, via disproportionation, which consists in the formation of one saturated chain and another unsaturated one, resulting from the transfer of a hydrogen atom from one chain to the other. In spite of being the most well-established type of photo-polymerisation, free-radical reactions still have some characteristic drawbacks, such as: polymerisation shrinkage, which leads to additional stress in the network; Trommsdorff effect, in which the rapid increase of the polymerisation rate (autoacceleration), can result in reaction runaway (*e.g.*, thermal losses), and/or undesirable changes of the forming polymer's properties; Oxygen ($O_2$) inhibition, in which radicals react with $O_2$ from the atmosphere instead of with the monomers, forming peroxides. Some of these issues are always present in photo-polymerisation systems, *e.g.*, the Trommsdorff effect, while others only appear in free-radical systems, *e.g.*, polymerisation shrinkage and $O_2$ inhibition [44], [45], [46], [47].

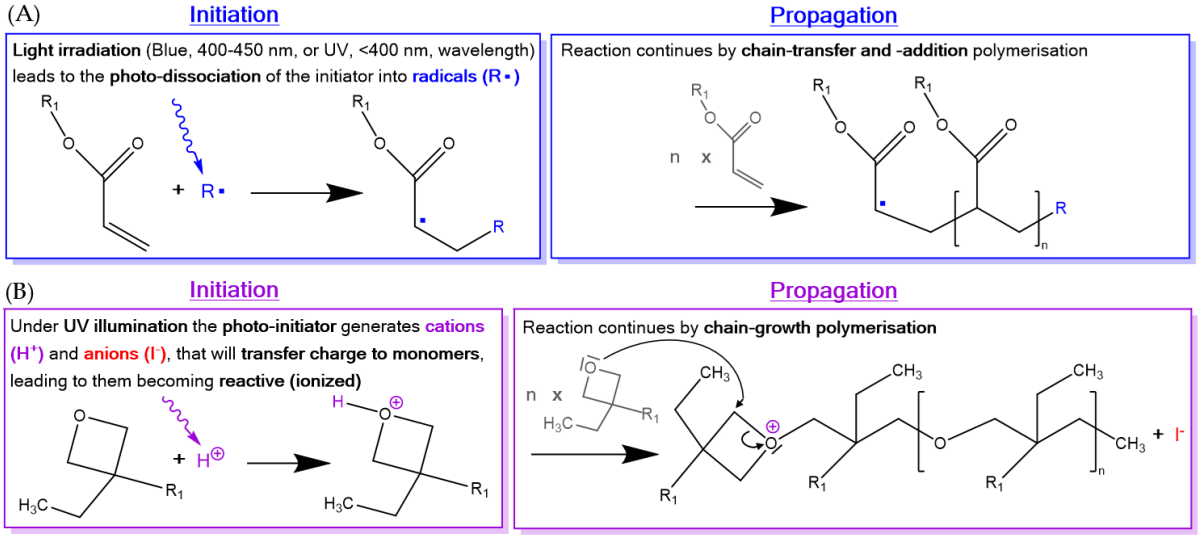


Figure 2 - Reaction mechanisms of (A) free-radical and (B) cationic ring-opening photo-polymerisations.

A conventional alternative is the cationic ring-opening photo-polymerisation (Figure 2 (B)). This type of reaction shows some similarities in kinetics and mechanisms with free-radical polymerisation, in the sense that the first two steps of initiation and propagation can also be used to describe cationic polymerisation. However, in this case, the reactive centres generated by the photo-initiator are not radicals but instead cations. These cations act as charge transfer agents for the cyclic monomers (*e.g.*, oxetanes), making the latter reactive. In order to release the ring strain, the monomers will open their ring configuration and form the longer polymeric

chains. The reaction will then continue (*i.e.*, propagation), this time not by chain-addition but rather via a step-growth polymerisation. It must be noted that the size and structure of the ring play a crucial role in the ability of the monomer to be polymerised. The reaction can meet its end primarily through two routes: (i) either all reactive groups are consumed (run out), or (ii) the reactive groups become sterically hindered, *i.e.*, isolated from each other and unable to react. Note that the majority of photo-initiators used in cationic reactions possess anions as well, whose purpose is to neutralise the charge from the cations [48], [49], [50].

### 1.3.2 Two-Stage Thiol–Acrylate Michael Addition & Photo-Polymerisation (TAMAP)

One of the most widely used multi-step processes is the two-stage thiol–acrylate Michael addition and photo-polymerisation (TAMAP) reaction developed by Yakacki *et al*. [13]. TAMAP uses a thiol–acrylate "click" reaction to partially crosslink the LC polydomain into a gel-like state, which is then aligned into a monodomain, typically via a stress-based mechanical deformation. Followed by a photo-polymerisation reaction based on the excess acrylate groups remaining unreacted in the first step. This second crosslinking step stabilises the monodomain. This method is not without its flaws. The thiol–acrylate "click" reaction uses a base catalyst, which initiates the reaction as soon as it is introduced to the solution. This is a major disadvantage of this procedure, heavily limiting the time for manoeuvring of the solution before initial crosslinking. Thus, making this method unsuitable for large-scale production and restricting its applicability for multiple coating techniques. Moreover, if the reaction rate exceeds the solvent evaporation rate, another issue might emerge, as the trapping of solvent could lead to irregularities in the LCE film.

### 1.3.3 Two-Step Wavelength-Selective Photo-Polymerisation (TWSP)

As an alternative, in this work a two-step wavelength-selective photo-polymerisation (TWSP) reaction is proposed. In this new procedure, the first crosslinking step is done by free-radical polymerisation of acrylate groups under blue light (400-450 nm) [14], [15] irradiation, in the isotropic phase ($> T_{NI}$). Next, the pre-LCE film is aligned when in the nematic phase ($< T_{NI}$). Then, the film, still in nematic phase, is illuminated with ultraviolet (UV) light (< 400 nm) [15], which photo-initiates a cationic ring-opening polymerisation of oxetane groups. In the end, a permanently programmed monodomain LCE film capable of large and reversible "hands-free" actuation under thermal stimulus is obtained. The photo nature of this methodology allows for greater spatio-temporal control over both crosslinking steps. Distinguishing this new procedure for its remarkable capability of influencing LC behaviour. The simplicity, controllability, precision, lack of time-dependency, and scalability of this procedure make it a promising and superior choice for synthesising and programming LCEs. This work will detail the development of this procedure, as well as characterise thermo-mechanics, actuation performance, and material properties. Moreover, the integration of the TWSP method with four-dimensional (4D) printing will also be investigated.

# 2

# MATERIALS AND METHODS

## 2.1 Oligomer Synthesis

For the oligomerisation step, two distinct types of mesogens were used to make the oligomers, in both the mesogen:chain extender molar ratio was 1:0.9. The first mixture was comprised of 79.5 wt. % 1,4-Bis[4-(6-acryloyloxyhexyloxy)benzoyloxy]-2-methylbenzene (RM82) (Figure A 1) and 19.9 wt. % 2,2′-(Ethylenedioxy)diethanethiol (DODT) (Figure A 3). And the second 76.2 wt. % 4-(6-(acryloyloxy)hexyloxy)phenyl-4-(6-(acryloyloxy)hexyloxy)benzoate (C6BAPE) (Figure A 2) and 23.2 wt. % DODT. Note that in both, a 0.6 wt. % of 1,8-Diazabicyclo[5.4.0]undec-7-ene (DBU) (Figure A 4) was used as the base catalyst, and they were dissolved in dichloromethane (DCM). All aforementioned compounds were commercially obtained. Once all compounds were in solution, the mixture was stirred for ~ 2 h. Then, it was poured onto a dish for overnight solvent evaporation in a vacuum at room temperature (RT).

## 2.2 Reaction Mixture & TWSP Procedure

To make the reaction mixture, 71.4 wt. % of oligomer was combined with 17.9 wt. % of acrylate-oxetane crosslinker (Figure A 5), synthesis detailed in section A.2, and two commercially obtained photo-initiators, 3.6 wt. % of the Irgacure 819 (Figure A 6) and 7.1 wt. % of the triarylsulfonium hexafluorophosphate salts (THPS) (Figure A 7). The mixture was dissolved in DCM, stirred for ~ 2h, and then spread onto the substrate, after which the solvent was left to evaporate overnight at RT. The first crosslinking step was done by free-radical photopolymerisation of acrylates under 20 mW/cm$^2$ of blue light irradiation (400-450 nm) [14] at 60 ºC for 5 min, in a nitrogen ($N_2$) atmosphere to prevent $O_2$ inhibition. Next, the pre-LCE film was cooled down to 0 ºC or - 5 ºC for the RM82- or C6BAPE-based oligomer samples, respectively, and the alignment was made by stretching or stamping with a mould. Then, at this temperature, the second crosslinking step was executed via the cationic ring-opening photopolymerisation of oxetanes under UV light (< 400 nm) [15] illumination. The exposure dose was 30 mW/cm$^2$ for 10 min. Figure A 9 shows an overview of the TWSP. Section A.4 details the optimisation of the initiators' concentration and exposure doses.

## 2.3 One-pot Mixture

For the one-pot procedure, RM82 was directly combined with DODT in various molar ratios, *i.e.*, 1:0.9, 1:1, 0.9:1, 0.8:1, and 0.7:1 (RM82:DODT), in the mixture. Except for these

changing amounts of RM82 and DODT the percentages of the other compounds in the mixture remained the same, 17.9 wt. % of acrylate-oxetane, 3.6 wt. % Irgacure 819, and 7.1 wt. % THPS, dissolved in DCM. Note that in this case, no base catalyst was added.

## 2.4 Characterisation Techniques

The degree of polymerisation (DP), *i.e.*, average chain length, of the oligomers, as well as their number-averaged molecular weight (Mn), were determined from the proton nuclear magnetic resonance ($^1$H-NMR) spectra measured on a 400MHz Bruker Advance III HD spectrometer. For these measurements, each oligomer was diluted in deuterated chloroform (99.8 atom% D). The data was processed using Mnova software. Gel permeation chromatography (GPC) measurements with a Shimadzu UV-3102 PC apparatus were executed to obtain the polydispersity index (PDI) of the oligomers. For this, tetrahydrofuran (THF) as the solvent and polydopamine (PDA) at 254 nm (with 4 nm intervals) as the detector were used. The phase transition temperatures of the oligomers were obtained via differential scanning calorimetry (DSC) measurements in TA instruments Discovery DSC 2500. The temperature ranged from -50 to 150 °C with heating and cooling rates of 3 °C/min. Ultraviolet-visible (UV-vis) absorption spectra of the initiators (100 ppm concentration in ethanol) were extracted by a PerkinElmer Lambda 750 spectrophotometer with a 150 mm integrated sphere detector. The absorption measurements were taken between 150-550 nm with 1 nm intervals, and a response of 0.20 s by the detector. To determine the conversion of acrylates and oxetanes, Fourier-transform infrared spectroscopy (FTIR) measurements were performed in a Varian 670-IR spectrometer. This data was interpreted via the Varian Resolution 4.0 software. To estimate the S, X-ray diffraction (XRD) measurements were executed on a Ganesha lab instrument equipped with a Genix-Cu ultralow divergence source that generates X-ray photons with a wavelength and flux of 0.154 nm and 1×108 photons $s^{-1}$, respectively. Diffraction patterns were obtained using a Pilatus 300 K silicon pixel detector with 487×619 pixels of 172×172 $\mu m^2$. Silver behenate was used as a calibration standard. The sample-to-detector distance was 89 mm for wide-angle (WAXS) configuration. To study the stretched LCE films' mechanical properties as well as the degree and temperature range of the actuation, dynamic mechanical thermal analysis (DMA) measurements were executed in TA instruments Q800 DMA. To study the surface topography changes under temperature variations of the stamped samples, interferometry measurements via a Sensofar S Neox were carried out. With a Leica DM6000 polarised optical microscope (POM), the molecules' alignment in the LCE films could be determined. Note that all images were taken with the sample between cross-polarisers. A Hyrel 3D printer was used for the Direct Ink Writing of the LCEs, also known as 4D printing of LCEs. Beforehand, the Autodesk Inventor 3D CAD software was used to make the three-dimensional (3D) design of the shape intended for printing. Then, this design was processed by the PrusaSlice software, which gave the basic Gcode for the programming of the printer machine. However, prior to and during the printing process, changes to the code were made.

# 3

# Results and Discussion

## 3.1 Working Principle Behind the TWSP Method

As an unexplored method in literature, it is pertinent to explain the physicochemical principles that make this methodology feasible. Figure 3 depicts the stages of the TWSP process. First, the reaction mixture, either oligomer-based or one-pot, is prepared for coating the substrate. Then this liquid coating, *i.e.*, in the isotropic phase (> $T_{NI}$), is illuminated with 20 mW/cm² of blue light (400-450 nm) [14] for 5 min in an $N_2$ atmosphere, which initiates the free-radical photo-polymerisation of the acrylates in the system, leading to the formation of a gel-like partially crosslinked LC polydomain. Next, this pre-LCE film is cooled to its nematic phase (< $T_{NI}$), where the desired alignment is instilled, establishing a temporary monodomain in the network. The alignment consists of the re-orientation of the mesogen molecules along a common direction (n). To permanently program this monodomain, a second independent crosslinking step is performed. This time, the pre-LCE film, still < $T_{NI}$, is exposed to 30 mW/cm² of UV irradiation (< 400 nm) [15] for 10 min, resulting in the photo-initiation of the cationic ring-opening polymerisation of the oxetanes. In the end, a fully crosslinked LCE film capable of large and reversible "hands-free" actuation under thermal stimulus is obtained.

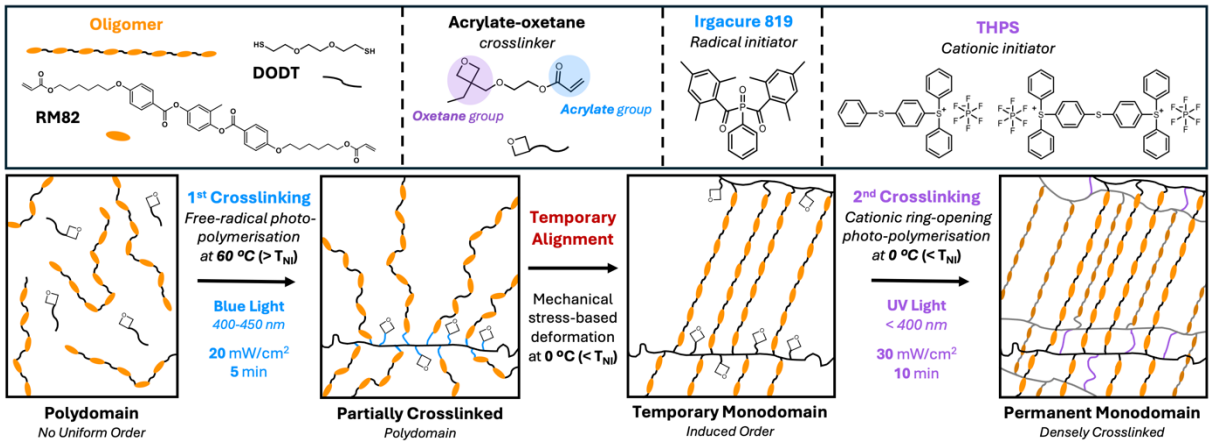

Figure 3 - Schematic illustration of the TWSP process.

## 3.2 Oligomer-based Procedure

As briefly mentioned above, the TWSP method can start with either an oligomer-based or one-pot reaction mixture. The research began by using the former approach, in which the oligomer is first synthesised and then combined in the reaction mixture. Literature is filled with studies where oligomers serve as starting or intermediate materials of polymerisation

reactions. They will be employed in a similar manner in this work. A comprehensive understanding of the TWSP requires a brief introduction to the concept of an oligomer. Built from homologous monomer units as standard polymers, oligomers are a sub-category of polymers, mainly differentiated for the shortness of their chain. Consequently, they possess low molecular weights (< 10 kDa) [51]. Since they are comprised of fewer repeating units, their physical properties are substantially dependent on their DP. Amongst the many properties that make oligomers more attractive for LCE fabrication compared to monomers, one that stands out is the lower $T_g$ of oligomers relative to monomers [52], [53]. For instance, the oligomers synthesised from the RM82 monomer in this research had their $T_g$ between - 20 and - 18 ºC (Table 1), while the melting point of the RM82 monomer by itself is around 86 ºC [54]. Therefore, since oligomers do not crystalise at RT contrary to monomers, this makes them superior choices for systems like the LCE ones, where elasticity is a crucial feature the material must possess.

### 3.2.1 Characterisation of the Synthesised Oligomers

In this oligomer-based TWSP approach, the oligomer is the only LC compound, meaning it will greatly influence the final LCEs' properties. Thus, it is important to structurally and thermally analyse the synthesised oligomers to shed light on crucial LC properties. Moreover, this knowledge can be used to further tailor the final LCE properties. First, to determine the DP and Mn of the oligomers, NMR measurements were performed. With the aid of the Mnova software, the spectra of the *olgRM82-1* (Figure A 12), *olgRM82-2* (Figure A 13), *olgRM82-3* (Figure A 14), and *olgC6BAPE-1* (Figure A 15) were extracted and analysed. The detailed calculations are depicted in section A.5. Table 1 summarises the DP and Mn values of each oligomer.

Table 1 - Characteristic parameters for each synthesised oligomer.

| Oligomers | DP [r. u.] | Mn [g/mol] | PDI [A. U] | Phase Transition Temperatures [°C] | | | | |
|---|---|---|---|---|---|---|---|---|
| | | | | $T_g$ | $T_{SN}$ | | $T_{NI}$ | |
| | | | | | Exo | Endo | Exo | Endo |
| *olgRM82-1* | 12 | 10 182.70 | 2.39 | - 20.37 | 49.78 | 50.81 | 88.77 | 89.53 |
| *olgRM82-2* | 13 | 11 284.19 | 2.46 | - 18.55 | 48.61 | 50.92 | 85.65 | 87.38 |
| *olgRM82-3* | 13 | 11 288.46 | 2.40 | - 18.80 | 50.17 | 51.35 | 87.95 | 88.61 |
| *olgC6BAPE-1* | 11 | 7 611.06 | 2.57 | - 29.22 | 4.19 | 8.53 | 34.82 | 39.05 |

Through GPC measurements, the PDI of the oligomers was also determined. The PDI is determined from the ratio between weight-average molecular weight (Mw) and Mn, meaning that an ideal uniform polymer chain length corresponds to a PDI equal to 1 [55]. However, in practice, such a value is extremely difficult, if not impossible, to reach. The oligomer-specific normalised absorption as a function of time plots are presented in Figure A 16. The parameters extracted are organised in Table A 1. The PDI of each oligomer is indicated in Table 1. The *olgC6BAPE-1* had the highest polydispersity of 2.57, and amongst the three RM82-based oligomers, the first was the least size dispersed (PDI = 2.39). These PDI values are comparable to

those found in literature [56], [57], [58]. The alignment will depend on the LC phase of the material during polymerisation. To determine the phase transition temperatures of the oligomers, DSC measurements were performed. The DSC endothermal (Endo) and exothermal (Exo) curves are shown in Figure A 17, with the respective $T_g$, smectic-to-nematic transition temperature ($T_{SN}$), and $T_{NI}$ peaks marked. Table 1 summarises these values. The transition temperatures remained similar for the RM82-based oligomers but slightly lower for the *olgRM82-2*. However, for the *olgC6BAPE-1*, all transition temperatures were much cooler.

## 3.3 Proof of Concept for the TWSP Methodology

For the TWSP method to work, two independent photo-polymerisation reactions must take place. Hence, neither of the photo-initiators must absorb out of turn. To investigate this, UV-vis spectroscopy measurements of the free-radical initiator, Irgacure 819, and of the cationic initiator, THPS, were performed. The results are shown in Figure 4 (A), where a non-overlapping area on the relevant wavelength range can clearly be seen. Moreover, it can also be seen that the absorption of the initiators overlaps in the UV region, meaning that if the first stage were to involve UV instead of blue light, both polymerisation reactions would happen at once. If that were to occur, the programming of a second shape would not be possible as the film would fully crosslink in the molecular organisation it possessed during UV irradiation.

### 3.3.1 Chemical Properties Analysis via FTIR Characterisation

With the theoretical principle of TWSP established, the experimental trials could begin. For this, three samples, based on *olgRM82-1*, were made: (i) a reference one, without any crosslinking; (ii) one just partially crosslinked with one step; and (iii) another which was fully crosslinked with the two steps. Then, via FTIR measurements, the infrared absorption spectra of these samples were obtained (Figure 4 (B)). A thorough inspection of these spectra reveals a significant decrease in absorption at certain wavenumbers in some samples relative to others. The nature of these changes lies in the chemical bond interactions. The most visible characteristic acrylate peaks (highlighted in blue) found were at ~ 1640 $cm^{-1}$, resulting from the stretching of the C=C bond [59], and ~ 1410 $cm^{-1}$ and ~ 810 $cm^{-1}$, related to the bending bands of the C-H bond in-plane and out-of-plane, respectively [60]. For all of these, a major decrease in infrared absorption intensity can be seen when comparing the reference sample (not crosslinked) with the other two samples. This suggests a nearly full conversion of acrylate groups after the first crosslinking step. On the other hand, the characteristic oxetane peak (purple highlighted) is found at ~ 985 $cm^{-1}$ related to the C-O-C bond [43], [61]. The intensity of this peak remains constant after the first crosslinking step relative to the reference (not crosslinked) sample. However, it significantly decreases in intensity after the second crosslinking step relative to the first. Hence, this implies that the oxetanes exclusively reacted in the second crosslinking stage. These initial results serve as a proof of concept for the TWSP method. Validating the independent conversion of acrylates and oxetanes in two separate sequential photo-

polymerisation reactions. Additionally, through kinetics FTIR, it was determined that the conversion of acrylates at 1410 $cm^{-1}$ was approximately 88% after nearly 1 min of blue light irradiation, while it took close to 3 min under UV exposure for around 26% of oxetanes to be converted at 985 $cm^{-1}$. Figure A 18 depicts these conversions over time.

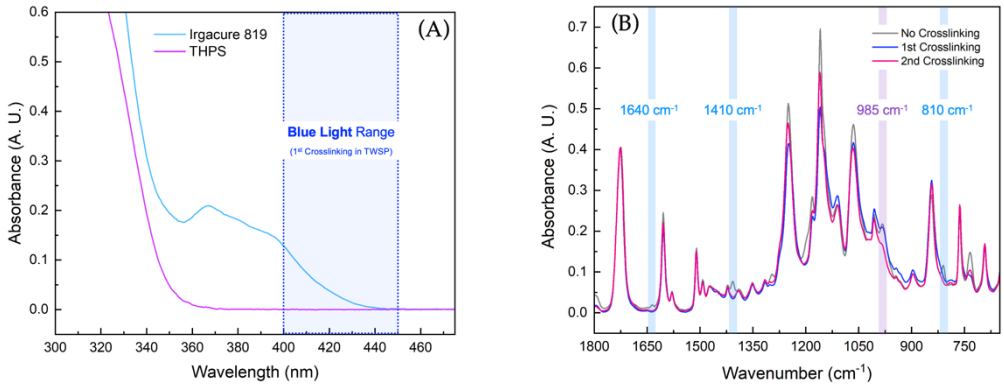


Figure 4 - (A) UV-vis absorption spectra of (—) Irgacure 819 and (—) THPS. (B) Infrared absorption spectra of: (—) No Crosslinking; (—) 1st Crosslinking (partially crosslinked); and (—) 2nd Crosslinking (fully crosslinked) samples. The characteristic peaks of acrylates and oxetanes are highlighted in blue and purple, respectively.

### 3.3.2 Preliminary Thermal Actuation Tests

With the principle working, the next step was to determine if, in practice, actuation was indeed feasible. To do so, a partially crosslinked film based on *olgRM82-1* was mechanically deformed by stretching. This deformation type leads to a contraction-based actuation, in which the LCE film will shrink in the same direction as the alignment and expand in the directions perpendicular to it (Figure 5 (A)) [40]. Figure A 19 demonstrates that with the TWSP method, it is possible to fabricate a reversible LCE thermal actuator. In this case, the polymeric film shrank from 22.5 mm long at RT (Figure A 19 (A)) to 19 mm at 80 ºC (Figure A 19 (B)). Additionally, once cooled down, the film reverted back to its original length.

## 3.4 Impact of Different LC Mesogens on the LCEs Properties

The DSC analysis of the synthesised oligomers shown in section 3.2.1 revealed that the *olgC6BAPE-1* transitioned between phases of matter at much cooler temperatures than the RM82-based oligomers. These differences originate primarily from the distinct chemical structures of the two mesogens. Contrary to the RM82 monomer, which possesses three benzene rings, C6BAPE is comprised of only two. This reduction of the aromatic parcel will lessen the π-π intermolecular interactions in C6BAPE, comparatively to the RM82 monomer. The weaker strength of these intermolecular interactions in the C6BAPE mesogen promotes the decrease in onset transition temperatures [62]. To determine if LCEs with distinct mesogens would exhibit different properties, two homologous samples differentiated only by the mesogen used were fabricated. Both samples were stretched in equal amounts, with a cure strain of 135.3%, when in their partially crosslinked state.

### 3.4.1 Thermo-responsive Actuation: *olgC6BAPE-1 vs olgRM82-2*

The comparative analysis started with the naked-eye observation of the thermo-response of the two polymeric films. Figure 5 (B) shows the initial length and width of the *olgRM82-2* sample. Upon heating to 100 ºC, as exhibited in Figure 5 (C), the LCE film undergoes a loss in its length and a gain in its width, which is in accordance with the contraction-based actuation explanation detailed in section 3.3.2. The same is true for the *olgC6BAPE-1* film as can be observed in Figure 5 (D) and (E). After cooling down, both samples reverted back to their original dimensions at RT, confirming the reversibility of their actuation. However, the *olgC6BAPE-1* sample, just from a naked-eye comparison, seems to shrink less than the *olgRM82-2* film, indicating a smaller actuation ability. A smaller actuation suggests the alignment quality of the *olgC6BAPE-1* film was worse than that of the *olgRM82-2* sample. This implies that the usage of the RM82 monomer instead of the C6BAPE would be favourable for LCEs with better shape-memory properties. These speculations will be further explored in section 3.4.4 by DMA characterisation.

### 3.4.2 Task Performance Ability of the *olgRM82-2* LCE Film

The seemingly larger actuation of the *olgRM82-2* film encouraged the study of its ability to perform a defined task. Thus, the viability of using this material to lift weights was tested. Note that the length reduction of the *olgC6BAPE-1* sample was not sufficiently large to justify this naked-eye experiment. The test consisted of gripping the two extremities of the LCE film, which weighed 27.7 mg, with two metal clips, each weighing 13.54 g. Then, one of the metal clips was placed on a retort stand, and a ruler was put next to it for easy observation of length changes. At RT, Figure 5 (F), the film could hold the weight of the suspended metal clip without ripping, and the visible region of the film measured approximately 10 mm in length. Then, via a heating gun, the film's temperature was increased to around 60 ºC, and the film shrank to ~ 6 mm (Figure 5 (G)). Furthermore, the shrinkage of the sample resulted in the simultaneous lifting of the metal clip, which was much heavier than the film itself. Hence, it was determined that this film was capable of lifting weights at least 488.81 times heavier than itself.

The potential uses for this kind of free-standing polymeric film capable of large reversible contraction-based actuation are numerous. One promising application could be in artificial muscles for soft-robotics or biomedicine. LCE-based materials are already used in this field of research [63], [64], but the ease and controllability of this new methodology could prove to be tremendously beneficial for further development.

### 3.4.3 Alignment & Order Parameter (S): *olgC6BAPE-1 vs olgRM82-2*

The LCEs' actuation emerges from the programming of the alignment. In this case, the stretching of the pre-LCE film should lead to the molecules orienting themselves in the stretching direction. Hence, it was expected the film possessed a planar alignment after deformation. To investigate this, POM measurements in transmission mode were performed. The *olgRM82-*

*2* sample was examined between cross-polarisers where it was seen that when the sample made a 45° angle with the polarisers (Figure 5 (H)), a bright image was observed. Conversely, when the polarisers were rotated and made a 0° angle with the sample (Figure 5 (I)), the image turned dark, resulting from the alignment of the molecules with one polariser. Thus, confirming the film's planar alignment. The planar alignment of this sample, as well as the *olgC6BAPE-1* film, was also validated via cross-polarisers on top of a light-emitting diode (LED) as shown in Figure A 20 (A), (B) and (C), (D), respectively.

Furthermore, the quality of the alignment in both cases was investigated through the determination of the degree of ordering of the molecules. For this, XRD measurements at RT were executed. From the diffraction patterns using the Lovell and Mitchell method [65], the order parameters were estimated (Section A.11). The *olgRM82-2* sample was found to possess an S=0.33 (Figure A 21). This value is between the S=1 of a crystal and the S=0 of a liquid, as was expected. However, the fact that this value is closer to the disordered state than the order one can be justified by the fact that this system is not made up of purely LC materials, containing instead elements like the crosslinker and the DODT, which will inevitably disrupt a perfect alignment. Nevertheless, this S fits between 0.2-0.5, which are commonly obtained S values for this type of LCE actuators [66], [67]. On the other hand, the *olgC6BAPE-1* film showed an unexpectedly low S of 0.034 (Figure A 22 (A)) implying the sample was either very poorly aligned (or not at all) or it was in the isotropic phase rather than the mesophase. As will be seen in section 3.4.4, the *olgC6BAPE-1* film actuates between 11-31 °C, meaning at RT the material is either already or in the process of transitioning to the isotropic phase. Thus, since the XRD measurement was done at RT, this low S value is a consequence not of a poor alignment but because the sample is in the isotropic phase. Additionally, despite the fact that no smectic phase was detected by the DSC analysis of the partially crosslinked films (Figure A 23). The XRD measurements showed a smectic phase in the *olgRM82-2* sample (Figure A 21 (A)).

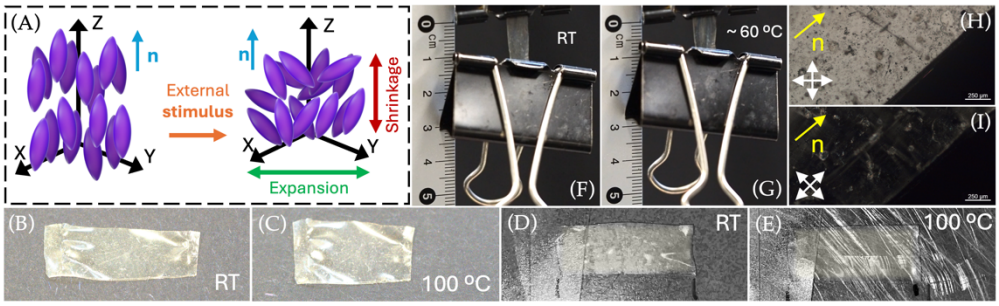


Figure 5 - (A) LC molecules' actuation upon external stimulus schematic. Contraction-based actuation of *olgRM82-2* film: (B) original length and width at RT; (C) length loss and width gain at 100 °C. Contraction-based actuation of *olgC6BAPE-* film: (D) original length and width at RT; (E) length loss and width gain at 100 °C. (F) *olgRM82-2* film holds weight at RT, and (G) at ~ 60 °C it shrinks and lifts the weight. POM images of the *olgRM82-2* film in between cross-polarisers: at (H) 45° (bright image) and (I) 0° (dark image). The yellow arrow is the stretching direction (n).

### 3.4.4 Dynamic Mechanical Behaviour: *olgC6BAPE-1 vs olgRM82-2*

For further characterisation of the samples' material properties, their response to a periodic deformation as a function of frequency or temperature was investigated. To do so, the

148 μm thick *olgC6BAPE-1* sample was cut to 19 mm in length and 6 mm in width. Likewise, the *olgRM82-2* film, with a thickness of 129 μm, also underwent a cutting to the dimensions of 26 mm in length and 10 mm in width. The DMA characterisation began with a temperature ramp (- 50 to 150 ºC range with 3ºC/min steps) and frequency sweep (amplitude of 15 μm was kept constant for a 1 Hz frequency). measurement. From the data extracted, the storage and loss modulus curves, as well as the tan delta curve, were plotted as functions of temperature.

The loss modulus (G'') quantifies the dissipation of energy or permanent structural change within a material resulting from being subjected to an applied force. With the rising temperature, the material becomes less viscous as the molecules undergo rearrangements, resulting in the release of energy as heat [68], [69], [70], [71]. In the case of the *olgC6BAPE-1* sample, as shown in Figure 6 (A)), from approximately - 45 ºC, the G'' starts to increase until reaching a peak at - 13.91 ºC and then declines drastically to close to zero. The maximum change in the polymer's mobility occurs at the temperature of this peak in G''. Thus, according to its chemical definition, this will be $T_g$ of the material [72]. Hence, the $T_g$ of the *olgC6BAPE-1* film is - 13.91 ºC. The initial increase stems from the fact that larger polymer segments are moving cooperatively and simultaneously, there is an increase in the easiness of deforming the material. However, once the $T_g$ is reached, as the temperature continues to rise above it, the molecular frictions diminish, and the dissipation of energy reduces substantially. Consequently, the G'' decreases [73], [74], [75]. Correspondingly, the G'' of the *olgRM82-2* sample (Figure 6 (C)) also rose rapidly at around - 40 ºC until the $T_g$ of - 10.50 ºC was reached, after which it quickly decreased.

On the other hand, the storage modulus (G') relates to the material's capacity to elastically store energy, meaning its energy recovery ability after deformation [70], [76]. As such, it is inevitably associated with the stiffness of the network, which tends to be higher in the glassy state since the polymer chains freeze in a rigid configuration limiting molecular motion (generally leading to a higher order). The G' curve can be divided into three principal regions. For lower temperatures ($< T_g$), the network will be stiffer as the material is in its glassy state. This results in a constant G' at a maximum of 276.29 MPa for the *olgC6BAPE-1* sample (Figure 6 (A)) and 425.89 MPa for the *olgRM82-2* sample (Figure 6 (C)). Then, as the temperature rises, the G' steadily decreases as a consequence of the polymer chains' enhanced mobility (*i.e.,* transition to soft-matter state). Eventually, this mobility will begin to stabilise, and only small, less significant variations will be measured. Thus, the G' will more or less stabilise in values of ~ 0.19 MPa for the *olgC6BAPE-1* film (Figure 6 (A)) and ~ 1.25 MPa for the *olgRM82-2* sample (Figure 6 (C)). Hence, the total variation of the G' with the change in temperature is ~ 276.10 MPa for the *olgC6BAPE-1* sample and almost double this value ~ 424.64 MPa for the *olgRM82-2* film. This suggests that the energy storage ability of the *olgRM82-2* sample is higher than that of the *olgC6BAPE-1* film, which in turn would imply the *olgRM82-2* sample is more elastic and, as such, more likely to recover closer to its original state after the applied force is removed [77]. However, this is not of particular relevance to this work since the goal is to have free-

standing films where no external force is being applied. In practice, it was found that both samples actuated autonomously in a fully reversible manner.

The ratio of the G'' (viscous response) to the G' (elastic response) is designated as tan delta (tanδ), *i.e.*, tanδ = G'' / G' [78]. In other words, tanδ indicates the relative degree of energy dissipation versus energy elastically stored in the material [79]. Moreover, tanδ is directly associated with the damping ratio (ζ), *i.e.*, amplitude reduction of the oscillation resulting from the energy lost from the system to overcome an applied stress, *i.e.*, tanδ = 2ζ [80]. There is a debate in the scientific community about which peak, the G'' or the tanδ, corresponds to the $T_g$ of the polymer. The $T_g$ values obtained for the partially crosslinked samples through DSC measurements, shown in Figure A 23, were closer to those of the G'' peaks. Therefore, the $T_g$ in this work will be defined as the peak in the G''. LCEs are distinguished from other polymers for demonstrating a "dynamic soft elasticity" feature, meaning an ability to absorb the strain being applied without loss of elastic energy. In other words, when heated to the $T_{NI}$, the local director axis' internal rotation leads the material to recover to a rubbery plateau [80], [81]. In the tanδ curve of the *olgRM82-2* sample (Figure 6 (C)), two peaks are observed. The first one, at 2.94 ºC, is associated with the transition from glassy to nematic, while the second, at 36.54 ºC, most likely stems from the material's "dynamic soft elasticity". There are other factors that can cause this second peak to appear, namely differences in the crosslinking density of the networks forming, which could lead to (resonance) phase separation in micro- and nano-lengths [80]. However, to achieve such a difference in crosslinking density, typically, the network is swelled after the first and before the second crosslinking [82], [83], which was not the case in this research. Furthermore, Figure 6 (D) shows the sample's actuation temperature at 33 ºC, which is close to the value of the second tanδ peak at 36.54 ºC. As such, the "dynamic soft elasticity" theory is the better match in this case. Conversely, in the *olgC6BAPE-1* film, only one peak at 6.52 ºC is found in its tanδ curve (Figure 6 (A)). This most likely stems from a measurement error. A straight line is seen from ~ 18 to 33 ºC in the G' curve. This means that the machine was only able to measure these two points and none in between, suggesting the modulus dropped to such low values that it was below the threshold for the minimum force of the equipment. Therefore, all indicates there would be a second peak which was simply not measured.

To measure the LCE film's actuation, another type of DMA characterisation was executed, this time a controlled forced (0.001 N) temperature ramp (- 50 to 150 ºC range with 3ºC/min steps) measurement. The strain percentage curve of the *olgC6BAPE-1* film, presented in Figure 6 (B), shows that the shrinkage of the material leads to a variation in strain of 17.39%. While the *olgRM82-2* sample's strain changes a total of 35.32% (Figure 6 (D)). This value is nearly double that of the *olgC6BAPE-1* film. Suggesting that an LCE produced based on the RM82 mesogen possesses a far larger actuation capability than one based on the C6BAPE mesogen. This result is in accord with and serves as validation regarding the previous speculations concerning the higher shrinkage ability of the sample composed by the oligomer with the RM82 mesogen stated in section 3.4.1. Moreover, it was found that 90% of the *olgRM82-2*

sample's actuation falls in the temperature window from 33 ºC to 90 ºC, a range of 57 ºC (Figure 6 (D)). Conversely, the *olgC6BAPE-1* film actuated in 90% across 20 ºC, between 11 and 31 ºC, a much cooler and shorter window compared to the previous case. This corroborates that a mesogen that transitions between states of matter at lower temperatures leads to the production of an LCE film that also actuates at lower temperatures. Furthermore, the larger actuation ability of the *olgRM82-2* sample comes at the cost of its actuation sharpness, in the sense that the LCEs actuation is spread over a bigger and less restrictive temperature range. This might make the usage of these RM82-based polymeric films less favourable for certain applications which require actuation in a very controlled and limited environment. Nevertheless, the fact that the *olgC6BAPE-1* film actuates at RT is not ideal, as it adds an additional constraint of having to cool down the sample.

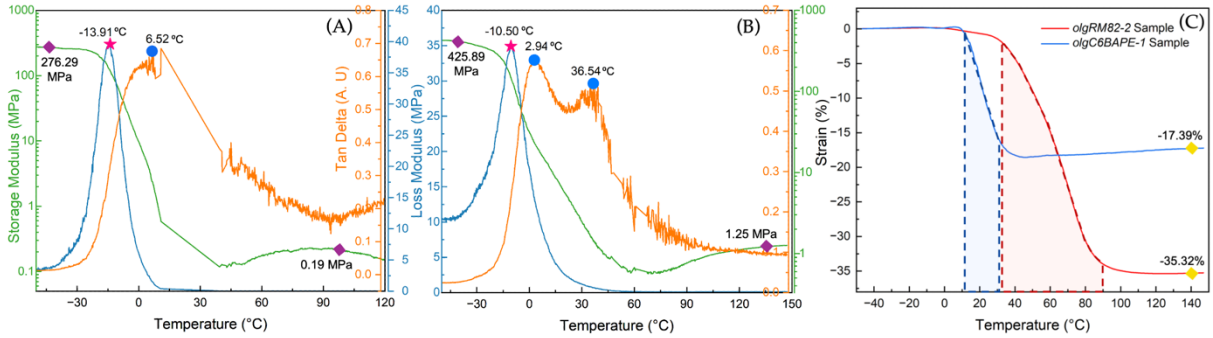


Figure 6 – G', G'', and tanδ *vs* temperature plots of the (A) *olgC6BAPE-1* and (B) *olgRM82-2* samples. (C) Strain *vs* temperature plot of the *olgC6BAPE-1* and *olgRM82-2* samples.

These results indicate that for homologous prepared samples, the change of the LC mesogen by itself can alone drastically change the LCEs' actuation properties. The reasoning behind these differences, as formerly explained during the introduction of section 3.4, could be related to the lessening in the strength of the intermolecular interactions, which will contribute to the lowering of the required energy for inducing the actuation of the LCE [62].

## 3.5 Distinct Actuation Shapes: Types of Alignments

Until this point, only one type of actuation was explored, but as a new fabrication and processing method, TWSP is not limited to solely one kind of alignment. On the contrary, it should allow for the programming of different alignments. Hence, distinct actuation shapes.

### 3.5.1 Stamping Deformation: Azimuthal Alignment

To explore a different alignment, a homologous sample to the *olgRM82-2* film from section 3.4.1 was made using the *olgRM82-1*. However, this time, after the initial crosslinking, the sample was not stretched but instead stamped with a mould comprised of a 20x20 grid of pillars (*i.e.*, dots), thus 400 in total, each with a diameter and height of 100 µm and 150 µm respectively, and evenly spaced 1 mm apart from the neighbouring dots. The goal was to create azimuthal-aligned dot-shaped indents in the LCE film. Then, this alignment was stabilised,

*i.e.*, permanently programmed, via the second crosslinking step. Figure 7 exhibits the series of steps followed to achieve the chosen dots-based pattern.

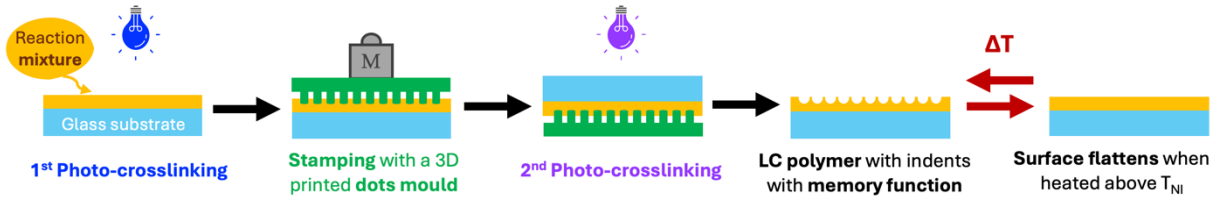


Figure 7 - Illustration of the experimental stages followed in order to stamp the film with the chosen (dots) pattern.

For the text's fluidity, the formerly described sample will be designated as the dots sample. With POM, in between cross-polarisers, an alignment which can be either radial or azimuthal is seen emerging from the centre of the dot (Figure 8 (A)). To study this sample's director field, a first-order retardation plate with a fixed optical path difference between 530 and 560 nm was inserted in POM. With this accessory, it is possible to study the optical sign's orientation (local director) through the birefringence of specific regions. Figure 8 (B) shows that since the director in the yellow regions orients diagonally to the left and in the blue regions it orients diagonally to the right, the overall director field forms a circular alignment, meaning the sample possesses an azimuthal alignment [84].

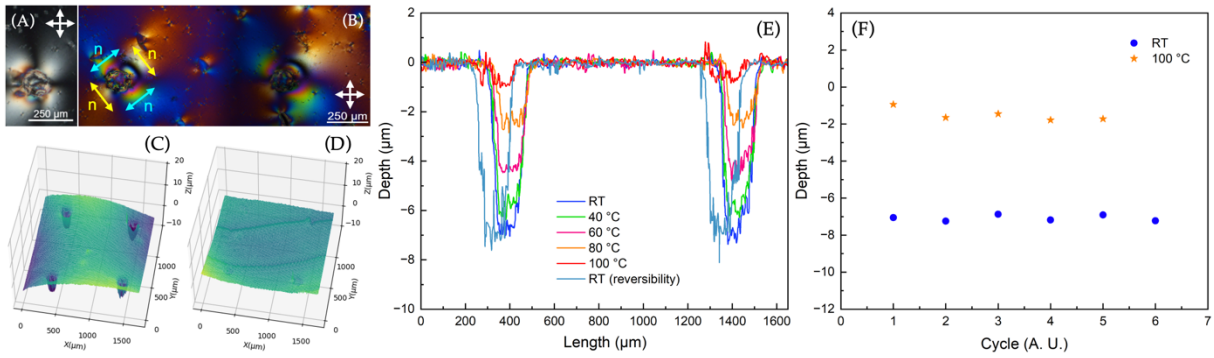


Figure 8 - (A) POM image of a dot from the dots sample. (B) POM with a first-order retardation plate image, where the azimuthal alignment in each dot is seen. (C) 3D plotted interferometry images at RT (relaxed state) and (D) at 100 °C (actuated state). (E) Depth *vs* length plot and (F) depth *vs* cycle plot of the dots sample (168.85 µm thickness).

To investigate the actuation of these micro-sized dots interferometry measurements were performed. The three-dimensional (3D) plots exhibiting the thermal actuation of a couple of representative dots are presented in Figure 8 (C) and (D). The stamping process determines the spatial location of the dots in the sample and forces the molecules to relocate downwards and horizontally to the sides. This results from the appliance of compressive forces (stress-based deformation via the usage of a weight) vertically onto the sample in the specific sites containing dot-shaped bumps. When heated, the depth of the indents progressively decreased until reaching a near-flat state at 100 °C. Then, once the sample was cooled to RT, the indents recovered their original depth. This reversible thermal actuation is illustrated in the depth profiles over temperature shown in Figure 8 (E). The overtime longevity of the actuation capacity and reversibility of this material was also investigated through cyclical measurements of sequential heating and cooling of the sample (Figure A 26 (A)). To further tailor the previous

results for an easier interpretation, a depth *vs* cycle plot of this LCE film's actuation was made, presented in Figure 8 (F). No significant tendency of decrease in depth over time is seen, which implies that this LCE film's actuation ability is viable for repeated long-term purposes.

Through the TWSP process, it is possible to make this type of localised reversible actuation. One promising application is, for instance, for human-machine interactive technologies, *e.g.,* haptic surfaces. As the versatile material that LCEs are, their implementation in multiple haptic applications can already be found in the literature [2], [64], [85], [86]. Nevertheless, the additional spatio-temporal control that the TWSP method offers cannot be matched by competitor procedures, making its implementation for such applications particularly promising.

## 3.6 Crosslinker's Concentration Influence on Actuation

With the goal of decreasing material and time costs, the impact of the crosslinker concentration in the reaction mixture over the properties of the LCEs produced was investigated.

### 3.6.1 Preliminary Trials: Six Samples Stamped with the Dots Mould

Initially, a total of six different concentrations were investigated, namely 17.9, 14.9, 11.7, 8.1, 4.3, and 2.2 wt. % of crosslinker. To facilitate direct comparison, all samples were stamped with the same dots mould described in section 3.5.1, and their actuation was measured across the same temperature interval via interferometry. Note that all the mixtures used contained *olgRM82-1*. The goal was to study the impact of the crosslinker concentration on actuation and possibly even determine if there was a threshold concentration for actuation. However, as can be seen in Figure A 25, the samples actuated reversibly even at very low concentrations of crosslinker. Thus, through this measurement, no clear correlation between these two parameters could be established. Nevertheless, one observation can be made from an attentive inspection of the results shown in Figure A 25, is that the degree of actuation of the material seems to increase with the decrease in crosslinker content. This can be explained by the fact that a larger percentage of crosslinker in the mixture will lead to a higher crosslink density of the network, which in turn can restrict the molecules' freedom of movement and consequently decrease the degree of actuation the LCEs are capable of.

### 3.6.2 No Crosslinker Tests

These results were quite surprising since they suggested the LCEs' actuation ability was not significantly dependent on the amount of crosslinker present in the sample. To further investigate this, tests of samples containing no crosslinker at all were performed. The objective was to see if alignment could still be programmed in a sample made with no crosslinker. Figure 9 (A) confirms that an LCE sample that does not contain a crosslinker can still actuate reversibly when heated and cooled. Figure A 26 (B) shows that this is still true over multiple cycles of heating and cooling. Another interesting fact is that not only is this sample capable of reversible actuation, but it seems to demonstrate a larger actuation, in the sense that the

depth of the dots is bigger relative to the film's thickness, and they also become completely flat when fully actuated. This does not happen in the other samples with a crosslinker, most likely because the acrylate-oxetane molecule itself might slightly disturb the alignment's homogeneity in certain regions. However, in Figure 9 (B), a small tendency can be spotted as the reversibility of the dots seems to be decreasing slightly over the cycles, which was not the case for the samples with crosslinker (Figure 8 (C)).

This is a surprising discovery, but it does not invalidate the working principle explained previously. Since, as was verified with FTIR measurements, when the crosslinker is present in the mixture, the free-radical polymerisation of acrylates and then the cationic ring-opening polymerisation of oxetanes, do happen sequentially. Nevertheless, in the scenario where no crosslinker is present in the mixture, the physical principle responsible for the alignment has changed. After some thought and research of the literature it is suspected that there are acrylate groups that remain unreacted after the first crosslinking step. These acrylates can then react in the second crosslinking step, under UV irradiation, with excess Irgacure 819 since the initiator rarely is consumed in its entirety or with THPS, which, besides cations, can also form reactive radicals [42]. To test the veracity of this theory, a homologous sample to the previous one was made. However, this sample was only partially crosslinked, meaning it only underwent the first crosslinking step. Then, its actuation was measured via interferometry. As shown in Figure 9 (C), the sample actuates once as expected, but it doesn't go back to its initial depth, staying in a flat state instead. Thus, meaning the actuation is not reversible. This result confirms that, indeed, the permanent programming of the monodomain takes place in the second crosslinking step, even if not through a cationic photo-polymerisation. Hence, it can be concluded that LCEs capable of large reversible actuation can be fabricated through the TWSP method even without crosslinker. However, the tailorability of these films is far more limited since the mechanism for this occurrence is more unpredictable. Moreover, these films also show quicker actuation degradation, making them less viable for applications which require a repeated and sustained actuation performance.

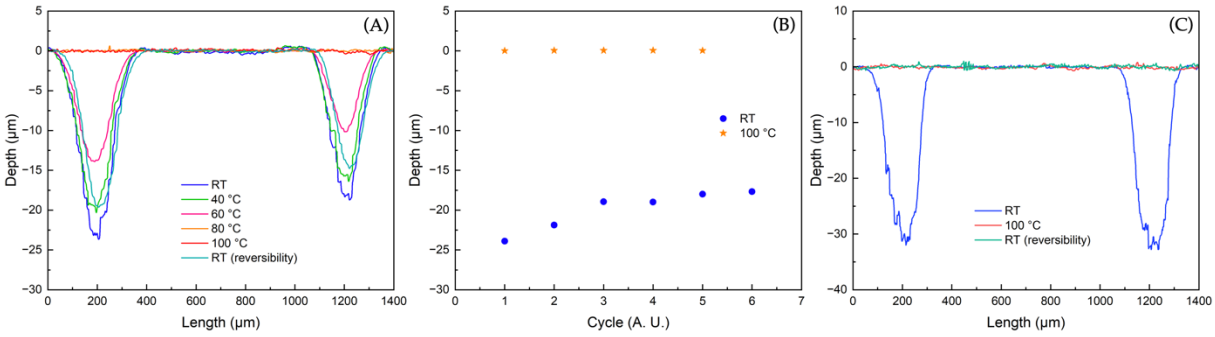


Figure 9 - (A) Depth *vs* length plot and (B) Depth *vs* cycle plot of a fully crosslinked 56.12 µm thick sample with no crosslinker. (C) Depth *vs* length plot of a partially crosslinked 46.70 µm thick sample with no crosslinker.

### 3.6.3 Stretched Samples with Distinct Crosslinker Concentrations

The previous results show that actuation is possible without a crosslinker but at the cost of other important variables, such as controllability over the processing method and the long-

term durability of the polymeric film's actuation. Therefore, it is still pertinent to investigate the practical impact of the crosslinker concentration on the LCEs' actuation ability. As previously seen, interferometry measurements of dots samples were not the best approach for this type of analysis. Therefore, a study of the mechanical response of stretched samples was performed. For this, three samples with crosslinker concentrations of 17.9, 11.7 and 4.3 wt. % were comparatively studied. Note that the first one with 17.9 wt. % corresponds to the *olgRM82-2* film characterised in section 3.4.4, and will serve as the reference sample (called *ref* sample). The other two samples will be referred to as *CC11.7wt%* (11.7 wt. % of crosslinker) and *CC4.3wt%* (4.3 wt. % of crosslinker) samples. After preparation for DMA, the 101 μm thick *CC11.7wt%* sample had a length of 25 mm and a width of 5.5 mm. On the other hand, the *CC4.3wt%* possessed a thickness of 123 μm and was 12.5 mm long and 5 mm wide. All samples underwent the same amount of stretching, with a curing strain of 135.3%, and were all made from *olgRM82-2*.

First, to fully understand the mechanical properties of these LCE films, temperature ramp and frequency sweep measurements were carried out. These DMA measurements are presented in: Figure 6 (C) for *ref* sample; Figure A 27 (A) for *CC11.7wt%* sample; and Figure A 27 (C) for *CC4.3wt%* sample. The main characteristic parameters of the samples are organised in Table 2. It was seen that the total G' variation for the *ref* sample was less than half that of the *CC11.7wt%* sample, and about one-fifth of the *CC4.3wt%* sample. Hence, a clear correlation can be established as the decrease of the crosslinker's concentration directly translates into a higher G' variation. As formerly mentioned in section 3.4.4, a higher change in the G' as a function of temperature, means the material in question possesses a superior capability for storing elastic energy, which in turn translates to a greater ability to closely recover its original shape after being subjected to the appliance of an external force. Therefore, in this case, the sample with the least crosslinker, *i.e.*, CC4.3wt%, is the one that shows better shape recovery following the removal of an applied force. In the G'', a similar tendency was also found, as the decrease of crosslinker content led to an increase of the $T_g$. As for the tanδ curves no significant increase or decrease of the peak's separation was seen, but a shifting tendency to higher temperatures was observed with the decrease in crosslinker.

The main focus was to determine how the concentration of crosslinker affected the LCEs' thermal actuation response, for which controlled force temperature ramp measurements were performed. These DMA measurements are shown in: Figure 6 (D) for *ref* sample; Figure A 27 (B) for *CC11.7wt%* sample; and Figure A 27 (D) for *CC4.3wt%* sample. Once again, Table 2 summarises the relevant parameters extracted. The comparison of the degree of actuation of these films, represented by the total strain variation, revealed that the sample with the middle amount of crosslinker, *i.e.*, CC11.7wt%, was the one that possessed the superior strain variation, and the lowest amount was recorded for the *ref* sample. However, the closeness between the values makes it difficult to draw definitive conclusions since experimental variations can always play a role. Nevertheless, these results suggest, as was previously speculated in section 3.6.1, that lowering the crosslinker concentrations enhances the actuation ability, while also

implying there might be a threshold value of crosslinker concentration in the mixture, for which the actuation reaches its maximum capacity. As for the temperature window corresponding to 90% of the actuation, it was found that the samples with the highest concentration of crosslinker possessed the shortest window. This makes sense since a larger amount of crosslinker allows for a higher degree of control over the TWSP process, which in turn facilitates the making and tailoring of LCE films which actuate in a more restricted temperature range. From these results, it was decided to continue the research with a concentration of 17.9 wt. % crosslinker since it allows for a higher degree of control over the LCEs' properties.

Additionally, through XRD measurements at RT, the S of the samples was determined to be 0.35 for the *CC11.7wt%* sample (Figure A 22 (B)) and 0.41 for the *CC4.3wt%* sample (Figure A 22 (C)). These S values are higher than the 0.33 of the *ref* sample and show a tendency of order increase with the decrease of the crosslinker concentration. This is in accordance with expectations since reducing the amount of non-LC elements in the mixture should increase the system's order, meaning more successful programming of the alignment.

Table 2 – Characteristic parameters of the three stretched samples with different concentrations of crosslinker.

| **Samples** | **G' variation** | **$T_g$** | **Tan delta peaks** | | **Total strain variation** | **Temperature range** *90% of actuation* |
|---|---|---|---|---|---|---|
| | | | *1st* | *2nd* | | |
| *ref* | 424.64 MPa | -10.50 °C | 2.94 °C | 36.54 °C | 35.32% | 33-90 °C |
| *CC11.7wt%* | 1018.74 MPa | -3.53 °C | 4.03 °C | 40.76 °C | 42.86% | 24-95 °C |
| *CC4.3wt%* | 2293.47 MPa | -2.60 °C | 7.28 °C | 44.22 °C | 39.36% | 37-99 °C |

## 3.7 One-pot Procedure

In an attempt to further simplify the TWSP method by eradicating one step, *i.e.*, oligomer synthesis, a one-pot approach was investigated. As conveyed in its denomination, a one-pot procedure consists of the simultaneous mixture of all reaction compounds in solution. The concentrations of each chemical used are enlisted in section 2.3. To achieve samples of the same quality level as those produced with the oligomer-based approach, different mesogen:chain extender molar ratios were experimented with, namely 1:0.9, 1:1, 0.9:1, 0.8:1, and 0.7:1. Note that the remaining TWSP procedure was kept the same. For an easier comparison, all samples were stamped with the same dots mould from section 3.5.1. Their reversible actuation was confirmed via interferometry measurements, as shown in Figure A 28. Unfortunately, these results were not very conclusive regarding the direct impact of the RM82:DODT ratio on the LCEs' actuation. Nonetheless, a thorough surface examination of the individual films yields valuable insights into some of their structural characteristics. As can be observed in Figure 10 (A) and (B), the films containing higher concentrations of mesogen were not only much more brittle after fully crosslinked, showing clear crystallisation signs at the edges, but also tended to relax back to their original configuration much faster, making it very difficult to cure them uniformly with the desired alignment. When the amount of mesogen was reduced, and the chain extender was increased in the mixture, as expected, less brittle and

more flexible samples were obtained (Figure 10 (C) and (D)). However, if the film was not made of an adequate amount of LC material, the degree of LC order was insufficient to uniformly program the alignment across the entire surface, leading to the appearance of blank spots, *i.e.*, regions missing dots (Figure 10 (E)).

### 3.7.1 Comparison of Procedures in TWSP: Oligomer-based *vs* One-pot

With the RM82:DODT molar ratios that more closely manifested the desired properties in the LCE films, namely 0.9:1 and 0.8:1, trials for making stretched samples through this procedure were explored. Yet, due to the less elastic nature of all these films compared to the ones fabricated through the oligomer-based procedure, all the former samples ruptured when stretched during the curing. As such, no DMA controlled force measurements were possible. Thus, a different approach was followed to determine the temperature window of the actuation of one-pot-produced samples. Interferometry measurements across a temperature range from 23.5 to 100 ºC, with 5 ºC steps, of the one-pot dots sample, with 0.9:1 RM82:DODT ratio (Figure A 29 (A)), and of the *olgRM82-2* dots sample (Figure A 29 (B)), were performed. From this data, the correlation between depth and temperature was established, as presented in Figure 10 (F). It was found that approximately 90% of both samples' actuation spreads across a 60 ºC temperature window. However, a small difference can be spotted, as in the *olgRM82-2* dots sample 90% of the actuation occurs between 30-90 ºC, while in the one-pot dots sample it takes place from 25 to 85 ºC. This suggests a very slight shift of the actuation to lower temperatures in the latter sample. Nevertheless, due to the proximity of these values, these measurements alone are insufficient to claim that the one-pot procedure allows for the fabrication of LCEs, which actuate at lower temperatures. As per the actuation degree, the *olgRM82-2* sample lost 72.7% of its original depth when actuated, while the one-pot sample lost 85.4%. This implies the one-pot procedure promotes the fabrication of LCEs capable of larger actuation.

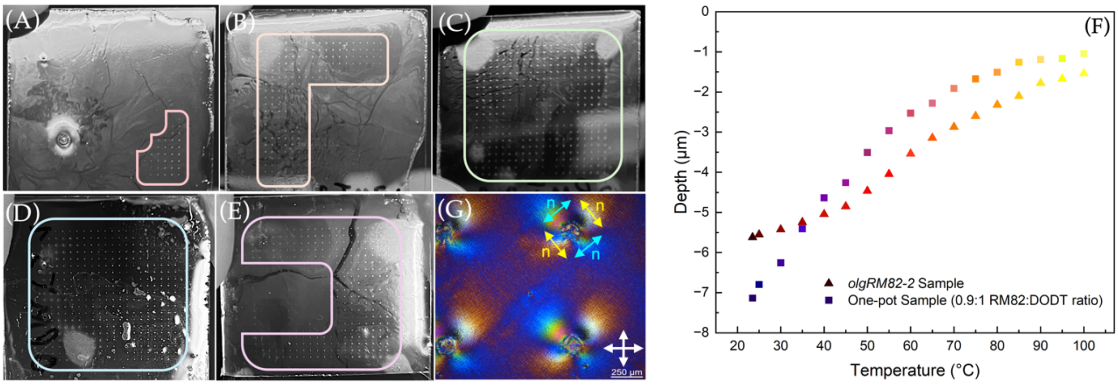


Figure 10 - One-pot dots samples, with the RM82:DODT ratios: (A) 1:0.9; (B) 1:1; (C) 0.9:1; (D) 0.8:1; (E) 0.7:1. The regions with successful alignment programming (dots) are surrounded by different coloured shapes (cooler tones=more dots; warmer tones=less dots). (F) Depth *vs* Length plot of the *olgRM82-2* and a one-pot dots samples. (G) POM with a first-order retardation plate image, where the azimuthal alignment in each dot is seen on the one-pot (0.9:1 RM82:DODT ratio) dots sample.

Even though the one-pot procedure might not be as versatile as the oligomer-based approach, it does allow for alignments such as azimuthal (Figure 10 (G)). Thus, perhaps this

procedure is better suited for applications and alignments that do not require free-standing films, *e.g.*, switchable surfaces.

## 3.8 Comparison of Methods: TWSP *vs* TAMAP

As previously explained, the TAMAP is a method for synthesising and programming LCE actuators. It is comprised of two sequential reactions, one instigated by the introduction of a base catalyst, followed by one photo-initiated. The first reaction creates the gelation of the LC polydomain by partially crosslinking it. Then, the molecules are aligned to achieve the desired temporary monodomain. Finally, the programming of the monodomain is made permanent by a photo-polymerization reaction based on the excess acrylate groups remaining unreacted in the first step. As enumerated previously in section 1.3.2, most of the issues related to this process stem from the first catalyst-based step for crosslinking. This stage is irradicated and replaced with two photo-initiated reactions in the TWSP method, facilitating the control and tailoring of the LCEs properties. This should be the case in principle, but to investigate what actually occurs in practice and draw direct comparisons, a TAMAP stretched sample was fabricated. The reaction mixture contained 75 wt. % of RM82, 19.5 wt. % of DODT, 4.3 wt. % of pentaerythritol crosslinker (Figure A 30), 1.1 wt. % of 2,2-Dimethoxy-2-phenylacetophenone (DMPA) photo-initiator (Figure A 31), and a catalytic amount of the dipropylamine catalyst (Figure A 32). Note that the components were dissolved in DCM for the preparation of the mixture. All chemicals came from commercial purchases. The catalyst was the last compound to be added to the mixture. To fabricate the sample, this mixture was spread evenly on a glass substrate and left for overnight thiol Michael addition reaction at RT. Followed by a 5 h solvent evaporation in a vacuum at 50 ºC. After, the pre-LCE film was removed from the glass and stretched with 135.3% curing strain. Then, at 30 ºC under an $N_2$ atmosphere, the sample was illuminated with 20 mW/cm$^2$ of UV light for 30 min.

To juxtapose the LCE film fabricated via TAMAP, designated as the *TAMAP* sample, with the one produced by TWSP, namely, the *ref* sample characterised in section 3.4.4, the sample's mechanical response was investigated. For this, two types of DMA measurements were performed on the *TAMAP* sample, with a thickness of 164 μm, a length of 11 mm and a width of 5 mm. The plotted DMA curves are presented in Figure A 33. The most relevant parameters obtained from these curves are arranged in Table 3. To facilitate direct comparisons, the parameters corresponding to the *ref* sample are also exhibited in Table 3. The *TAMAP* sample was shown to possess a lower $T_g$ than the *ref* sample. The G' variation in the *TAMAP* sample was more than double that in the *ref* sample. This suggests that the *TAMAP* sample has a higher ability to fully recover its original shape after an applied force is removed. However, since our goal is to make free-standing actuating films, this is not of particular importance. Something worth noting is that the separation between the two tanδ peaks increased in the *TAMAP* sample. This stems from the slightly lower $T_g$ and much higher $T_{NI}$, the latter being a consequence of the higher LC content in this *TAMAP* sample compared to the *ref*. As

for the actuation response, the strain variation of the two samples was not particularly distinct. Nonetheless, the *ref* sample showed a bigger change, implying it might possess a slightly larger actuation capability than the *TAMAP* sample. Furthermore, the temperature window for which 90% of the actuation of the *TAMAP* film took place only spread across 40 ºC of temperature, a significantly shorter actuation range than the 57 ºC of the *ref* sample.

In addition, the S of the *TAMAP* sample was determined to be 0.12 (Figure A 22 (D)), a far lower value than the S=0.33 of the *ref* sample. This higher disorder could be related to the increased mobility in the TAMAP system, which might facilitate the freedom of movement of the molecules and ease the transition to isotropic. This low S translates into a poorer alignment, which is the reason behind the smaller actuation ability of the *TAMAP* sample.

By harnessing the power of two photo-initiated reactions, the TWSP method allows for superior spatio-temporal control over both crosslinking stages. Thus, it enhances the ability to process and manipulate the molecular alignment for greater tailoring of the LCEs properties. Nevertheless, the previously shown DMA results indicate that some mechanical behaviours of these TWSP-produced films could still be optimised in further research. One way of doing so could be by tailoring the crosslinking density in both steps.

Table 3 – Characteristic DMA parameters of the *ref* and the TAMAP samples.

| **Samples** | **G' variation** | **$T_g$** | **Tan delta peaks** | | **Total strain variation** | **Temperature range** *90% of actuation* |
|---|---|---|---|---|---|---|
| | | | *1st* | *2nd* | | |
| *ref* | 424.64 MPa | -10.50 ºC | 2.94 ºC | 36.54 ºC | 35.32% | 33-90 ºC |
| *TAMAP* | 1233.93 MPa | -17.23 ºC | 0.57 ºC | 62.28 ºC | 32.84% | 54-94 ºC |

## 3.9 TWSP Combined with 4D Printing for LCEs Fabrication

To further prove TWSP's superiority compared to other methods, a technique of particular complexity for programming LCEs with intricate alignments was investigated. Namely, 4D printing, also known as Direct Ink Writing, of LCEs. First introduced by Skylar Tibbits in 2014, the term "4D printing" refers to manufacturing procedures that allow for the fabrication of "smart" materials, *i.e.*, materials which can exceed the static 3D systems through their dynamic ability to transform over time [87]. In the case of LCEs manufacturing, 4D printing serves as a tool for actively programming complex alignments. This will result in the material's actuation when exposed to the right stimulus. 4D printing is an intricate, time-dependent technique. This requirement for the initial material to be stable over time makes the combination of 4D printing with the TAMAP, as well as many similar catalyst-based procedures, not feasible. However, the higher control the dual wavelength-selective nature of the TWSP method provides makes it possible to perform these more demanding alignment processes. As a type of additive manufacturing, the 4D printing of an LCE will consist of: (i) designing the 3D structure in a computer-aided design (CAD) software, *e.g.*, Inventor, and saving the design in a stereolithography format (*.stl*); (ii) This is done so that the 3D design can then be processed by software like PrusaSlicer, which will, as the name suggests, slice into layers the 3D shape for

printing. The biggest benefit of this type of software lies in their ability to precisely and uniformly define different regions of the 3D model, calculate the best layer heights and automatically smooth the transition between them for optimal interfaces and printing quality; (iii) preparing and filling the syringe with the printing mixture (described in section 2.2), *olgRM82-3* was used in the case (characterised in section 3.2.1); (iv) importing the Gcode provided by the PrusaSlicer software to the open loop software of the Hyrel 3D Printer and making the needed adjustments; (v) printing the 3D object in a consecutive layer-by-layer manner; (vi) finally the material undergoes the TWSP reaction for permanent programming of this alignment.

### 3.9.1 Design and Modelling of the 3D Shape

CAD modelling plays a crucial role in 4D printing of LCEs, since the way in which the 3D shape is designed must take into account the dimensions, spacing and path of the printing nozzle. The printing path, in particular, is the most important factor of the whole process since it defines the direction in which the molecules will orient [88], [89]. For this work, the 3D shape constructed is shown in Figure 12 (A), and it consisted of a 10x4.88 mm rectangle. In this image, the zigzag-like printing path the nozzle will follow can also be seen. Note that the nozzle used possessed a diameter ($\phi$) of 400 μm, and the spacing between the printed lines ($x$) was 1 μm. Once the shape was constructed as desired, following the steps explained prior, the Gcode associated with the shape was extracted. Nevertheless, before and sometimes even during printing, the Gcode suffered alterations. The final Gcode is presented in section A.21.

### 3.9.2 Programming of Different Alignments in the 4D Printed LCEs

Figure 12 (B) shows one of the many rectangles that were 4D printed. All samples possessed the same dimensions of 10 mm in length, ~ 5 mm in width, and thicknesses of 182 μm. The width value is slightly higher than that of the 3D shape designed with CAD, but that is to be expected as a result of the inevitable flow of material into the gaps between the printed lines. Nevertheless, the biggest achievement was the successful printing of multiple samples with a good degree of reproducibility. From these 4D printed rectangles, three distinct samples were prepared for further characterisation of material properties. The first consisted of a rectangle that was not stretched in any direction since the goal was to observe if actuation was feasible with just the alignment from the printing. In other words, this sample, called *4DP-1*, was fully cured with just the printing alignment. The second sample, referred to as *4DP-2*, was obtained by locking the alignment from printing by free-radical polymerisation of acrylates and then stretching the sample in the same direction as the alignment, with a curing strain of 140%, and performing the cationic ring-opening polymerisation of oxetanes in that state. Finally, the third sample, designated as *4DP-3*, was produced in a similar fashion to the *4DP-2* (140% curing strain), with the crucial difference that for this one, the stretching in the second crosslinking step was done in the perpendicular direction to the alignment from printing.

To confirm if the programming was successful, these samples were placed in between cross-polarisers on top of an LED. Figure 11 (A) and (B) clearly show the alignment instilled

just from the printing process in the *4DP-1* sample. However, compared to the *4DP-2* sample (Figure 11 (E) and (F)), the alignment of *4DP-1* seems worse since in Figure 11 (A) the sample does not become fully dark, *i.e.*, fully aligned with the polarisers, contrary to the *4DP-2* sample. This most likely stems from the fact that during the printing process, the material is heated up to 75 °C in order to be in a more fluidic state, which increases the likelihood that some of the material will flow into the gaps between the printed lines and introduce slight disorder in the system. In the *4DP-2* sample, this disorder is partially corrected by the second re-alignment of the molecules by stretching in the same direction during the second curing stage. Moreover, the comparison of these samples' POM images also supports these observations, as the contrast between Figure 11 (I) and (J) is greater, translating in a superior uniformity of the molecules' alignment in the director direction, compared to what is seen in Figure 11 (G) and (H). It must be noted that in Figure 11 (A) and (E), two bright regions at the top and bottom of both the *4DP-1* and *4DP-2* samples are seen. This likely stems from the design of the nozzle's printing path since in order for a rectangle to be manufactured, the nozzle has to make turns at the top and bottom of each line, resulting in a different alignment (*i.e.*, director orientation) along the width of the sample instead of the length, only at the top and bottom sections of the samples. On the contrary, the *4DP-3* sample demonstrates a cross- or radial-like alignment. This could mean that the alignment induced from printing and from stretching in the perpendicular direction are in some way competing with each other.

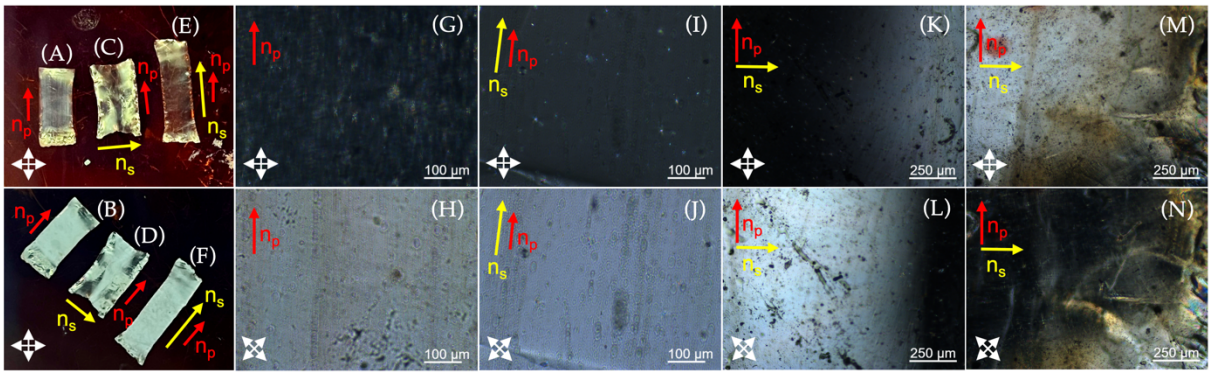


Figure 11 - Observation between cross-polarisers on top of an LED: *4DP-1* at (A) 0° (dark image) and (B) 45° (bright image); *4DP-3* at (C) 0° (dark image) and (D) 45° (bright image); *4DP-2* at (E) 0° (dark image) and (F) 45° (bright image). POM images (cross-polarisers): *4DP-1* at (G) 0° (dark image) and (H) 45° (bright image); *4DP-2* at (I) 0° (dark image) and (J) 45° (bright image); centre of *4DP-3* at (K) 0° (dark image) and (L) 45° (bright image); side of *4DP-3* at (M) 0° (bright image) and (N) 45° (dark image). The red and yellow arrows are the printing ($n_p$) and stretching ($n_s$) alignment directions, respectively.

To investigate further the difference in the alignment quality of the *4DP-1* and *4DP-2* samples, XRD measurements were performed at RT. *4DP-1* showed an S=0.23 (Figure A 22 (E)), while *4DP-2* possessed an S=0.28 (Figure A 22 (F)). This proves that the stretching of the *4DP-2* sample increased its alignment. However, something of note is the lower value of these S compared to the S=0.33 of the *ref* sample, which indicates that printing might not be the best method to obtain good alignments. In other words, despite the fact that 4D printing provides a way of making more complex alignments, this seems to come at the cost of their quality. This

could be a result of material flow into the spaces between printed lines during printing. Other works in literature corroborate these lower S values for 4D printed LCEs [67], [90], [91].

### 3.9.3 Thermo-responsive Actuation of the 4D Printed LCEs

The preliminary study of the thermal response of these samples was done via naked-eye observation and measurement of the length and width changes of the samples when subjected to temperature variations. Figure 12 (C) shows the 10 mm length of the *4DP-1* sample at RT, which shrank 2 mm to a value of 8 mm when heated to 80 ºC (Figure 12 (D)). Moreover, this sample, as expected, expanded in its width from 5 mm at RT to 5.5 mm at 80 ºC. Similarly, the *4DP-2* sample was 13 mm long in its relaxed state at RT (Figure 12 (E)), then lost 3 mm, and became only 10 mm long in its actuated state at 80 ºC (Figure 12 (F)). Additionally, its width of 4 mm at RT also increased to 5 mm at 80 ºC. In the *4DP-3* sample, it was seen that in the direction of stretching, *i.e.*, the width of the sample, it underwent a reduction of 2 mm from 7 mm at RT (Figure 12 (G)) to 5 mm when actuated at 80 ºC (Figure 12 (H)). Notably, contrary to the other samples, the length of the *4DP-3* sample, which would be expected to expand, did not show any change whatsoever when in the actuated state. This can be justified by the fact that even though the alignment from 4D printing would lead the film to contract in that direction (length loss) and expand in the opposite (width gain), this does not happen since there are two competing alignments in the sample. The alignment from stretching wants the sample to contract in the direction opposite the printing alignment (width loss) and expand in the other direction (length gain). In practice, it seems the alignment from stretching overpowers that from printing since the sample shrinks in its width. However, they cancel each other out, and no increase in the length is observed. The resulting actuation of this sample is interesting since it not only contracts in the director's direction like the prior samples, but it also lifts itself up to create a tunnel-like shape, which the other samples did not do (Figure 12 (I) and (J)).

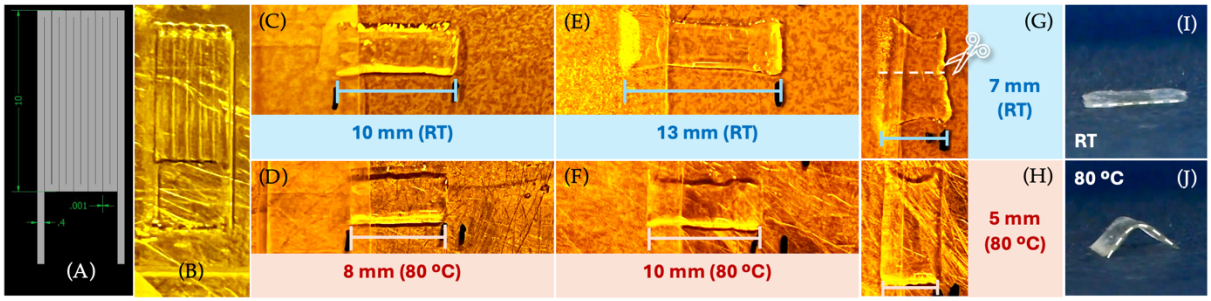


Figure 12 - (A) Image of the 10x4.88 mm rectangle designed in Inventor ($\phi$=400 µm, $x$=1 µm). (B) Picture of one printed rectangle. Actuation of the: *4DP-1* sample (C) 10 mm long at RT, and (D) 8 mm at 80 ºC; *4DP-2* sample (E) 13 mm long at RT, and (F) 10 mm at 80 ºC; *4DP-3* sample (G) 7 mm wide at RT, and (H) 5 mm at 80 ºC. *4DP-3* sample in (I) flat state at RT, and (J) actuated into a tunnel-like shape at 80 ºC.

### 3.9.4 Dynamic Mechanical Behaviour of the 4D-Printed LCEs

DMA measurements were performed to further characterise and compare the material and actuation properties of the 4D-printed samples. Unfortunately, the width of the *4DP-3*

sample, when in its actuated state, went below the minimum threshold of the machine. Thus, it was not possible to perform this mechanical study on the *4DP-3* sample. Therefore, only the *4DP-1* and *4DP-2* samples will be analysed. *4DP-1* had a thickness of 182 μm, a length of 10 mm and a width of 5 mm. Conversely, *4DP-2* was 13 mm long and 4 mm wide, with a thickness of 177 μm.

From the extracted DMA data, the two plots showing the mechanical properties and actuation of each material are presented in Figure A 34. The main parameters found for each sample were organised in Table 4. For both printed samples their $T_g$'s were slightly higher than the previous samples and above 0 ºC. The G' variation of the *4DP-2* sample is relatively close to that of the *ref* sample, while the *4DP-1* sample demonstrates more than double that change. Thus, the *4DP-1* sample displays a greater shape-recovering ability after the removal of an applied external stress. The tanδ peaks of both 4D-printed shapes show a shift towards warmer temperatures, which is in accordance with their higher $T_g$ values. As for the actuation ability, it was seen that the *4DP-2* actuated close to two times more than the *4DP-1* sample, as illustrated by the strain variation of *4DP-2* being nearly double that of *4DP-1*. This result makes sense since the *4DP-2* sample underwent programming in the same direction twice in both stages of the TWSP process. As seen *a priori* in POM, this double programming resulted in a better molecular alignment that translated into a superior actuation. Contrary to most of the cases studied prior, for these samples, a larger actuation capability did not lead to a wider temperature range for actuation. Instead, the *4DP-2* sample managed to actuate in a more restricted temperature range of 60 ºC than the *4DP-1* sample, which actuated across 71 ºC.

On an additional note, in Figure A 34 (B), a peculiar behaviour of the strain curve of the *4DP-1* sample is observed, where two actuating regions seem to be present. From 20 to ~ 70 ºC, a lot of noise is recorded, and the actuation is very slow and gradual, while from ~ 70 to 91 ºC, it suddenly becomes super-fast and sharp. As formerly mentioned in section 3.9.2, the molecules in this sample are not perfectly aligned with the director, contrary to the *4DP-2* sample. This is likely a consequence of material flow into the gaps between printed lines, which disrupt the alignment in certain regions. Thus, the unusual actuation behaviour shown by this sample is presumably a consequence of the disorder present in the alignment.

Table 4 – Characteristic DMA parameters of the *ref* and two 4D printed samples (*4DP-1* and *4DP-2*).

| **Samples** | **G' variation** | **$T_g$** | **Tan delta peaks** | | **Total strain variation** | **Temperature range** *90% of actuation* |
|---|---|---|---|---|---|---|
| | | | *1st* | *2nd* | | |
| *ref* | 424.64 MPa | -10.50 ºC | 2.94 ºC | 36.54 ºC | 35.32% | 33-90 ºC |
| *4DP-1* | 1271.83 MPa | 2.36 ºC | 15.87 ºC | 33.51 ºC | 13.73% | 20-91 ºC |
| *4DP-2* | 563.81 MPa | 1.18 ºC | 17.80 ºC | 40.61 ºC | 30.17% | 30-90 ºC |

# 4

# CONCLUSIONS AND FUTURE PERSPECTIVES

This work introduced a novel TWSP reaction for synthesising and programming LCEs capable of large "hands-free" reversible thermal actuation. The proof of concept for this method was obtained through the demonstration of the independent conversion of acrylates and oxetanes in two separate sequential photo-polymerisation reactions. Through this procedure, different alignments, for instance, planar and azimuthal, were effectively programmed. Their reversible actuation was also proven to be sustained over multiple cycles of heating and cooling. This opens the door for the making and tailoring of a variety of actuation shapes that cater to specific applications. For the case of a planarly aligned LCE film, which actuates in a shrinkage-based manner, one possible implementation could be in artificial muscles for soft-robotics or biomedicine. On the other hand, the azimuthally aligned LCEs show promise for applications that require localised actuation, such as switchable surfaces for human-machine interactive haptics technologies for example. Additionally, it was found that the TWSP method is viable for different LC mesogens, which increases the tailorability capability offered by this procedure. An LCE film with contraction-based actuation was shown to be successful in performing a defined task since it could lift a weight much heavier than the film itself. Furthermore, it was discovered that the TWSP method is viable even without a crosslinker agent. In this scenario, only free-radical reactions take place in both steps. Nonetheless, in these systems, a great deal of control is lost due to the unpredictable nature of the second reaction. On top of that, the LCEs produced with no crosslinker showed a far quicker degradation in their actuation, resulting in shorter lifetimes. Thus, making these types of LCEs unsuitable for applications that require repeated and sustained actuation performance. Moreover, it was found that the TWSP method is feasible with a starting oligomer-based approach but also through a one-pot mixture. Even though the latter showed promise for surface-switching applications, their current higher crystallisation tendency makes it impossible to produce free-standing films using this one-pot approach. Hence, optimisations of this procedure should be explored in future research, possibly through the adjustment of the reaction mixture's compounds. The direct juxtaposition of the TAMAP and TWSP methods revealed that the LCEs fabricated via TWSP reaction showed a larger actuation and higher order parameter. Yet the LCEs made by TAMAP actuated in a more restricted temperature window. These results indicate that the greater control provided by the TWSP reaction allows for the making of LCEs with higher alignment quality and larger actuation. However, more research on the TWSP method is still needed to shorten the temperature range for the actuation of these LCEs. An approach to do so could be by tailoring the crosslinking density in both reaction stages. In addition, the integration of the TWSP reaction with 4D printing showed fruitful results. The main promising

takeaway from this combination was the ability to effectively program alignment in both crosslinking steps. Depending on the chosen direction for the second alignment relative to the alignment from printing, it was possible to either increase the alignment quality (higher S) or make competing alignments for more complex actuation shapes. These results encourage the exploration of the integration of the TWSP reaction with other coating techniques, like bar coating, and/or patterning processes, such as resist-free photo-lithography.

# REFERENCES


[1] P. G. de Gennes and J. Prost, *The Physics of Liquid Crystals*. Clarendon Press, 1993. Accessed: Mar. 26, 2024. [Online]. Available: https://global.oup.com/academic/product/the-physics-of-liquid-crystals-9780198517856

[2] A. Gablier and E. M. Terentjev, 'Flexible force-bearing liquid crystalline elastomer component toward a dynamic braille platform', *Nano Select*, vol. 4, no. 5, pp. 324–332, May 2023, doi: 10.1002/nano.202300026.

[3] Y. Xiao, J. Wu, and Y. Zhang, 'Recent advances in the design, fabrication, actuation mechanisms and applications of liquid crystal elastomers', Jun. 01, 2023, *OAE Publishing Inc.* doi: 10.20517/ss.2023.03.

[4] J. Lagerwall, 'Liquid crystal elastomer actuators and sensors: Glimpses of the past, the present and perhaps the future', *Programmable Materials*, vol. 1, pp. 9–10, 2023, doi: 10.1017/pma.2023.8.

[5] K. Hisano *et al.*, 'Mechano-Optical Sensors Fabricated with Multilayered Liquid Crystal Elastomers Exhibiting Tunable Deformation Recovery', *Adv Funct Mater*, vol. 31, no. 40, p. 2104702, Oct. 2021, doi: 10.1002/ADFM.202104702.

[6] F. L. L. Visschers, M. Hendrikx, Y. Zhan, and D. Liu, 'Liquid crystal polymers with motile surfaces', *Soft Matter*, vol. 14, no. 24, pp. 4898–4912, Jun. 2018, doi: 10.1039/C8SM00524A.

[7] P. Lyu and D. Liu, 'Liquid crystal elastomer soft robotic arm for pick-and-place operation controlled by light', *https://doi.org/10.1117/12.3000162*, vol. 12907, pp. 21–27, Mar. 2024, doi: 10.1117/12.3000162.

[8] B. Gurboga, E. B. Tuncgovde, | Emine Kemiklioglu, E. Kemiklioglu, and E. Faculty, 'Liquid crystal-based elastomers in tissue engineering', *Biotechnol Bioeng*, vol. 119, no. 4, pp. 1047–1052, Apr. 2022, doi: 10.1002/BIT.28038.

[9] R. T. Rihani *et al.*, 'Liquid Crystal Elastomer-Based Microelectrode Array for In Vitro Neuronal Recordings', *Micromachines 2018, Vol. 9, Page 416*, vol. 9, no. 8, p. 416, Aug. 2018, doi: 10.3390/MI9080416.

[10] J. V. Selinger, *Introduction to the Theory of Soft Matter*. in Soft and Biological Matter. Cham: Springer International Publishing, 2016. doi: 10.1007/978-3-319-21054-4.

[11] M. O. Saed, A. H. Torbati, D. P. Nair, and C. M. Yakacki, 'Synthesis of programmable main-chain liquid-crystalline elastomers using a two-stage thiol-acrylate reaction', *Journal of Visualized Experiments*, vol. 2016, no. 107, Jan. 2016, doi: 10.3791/53546.

[12] K. M. Herbert, H. E. Fowler, J. M. McCracken, K. R. Schlafmann, J. A. Koch, and T. J. White, 'Synthesis and alignment of liquid crystalline elastomers', Jan. 01, 2022, *Nature Research*. doi: 10.1038/s41578-021-00359-z.

[13] C. M. Yakacki, M. Saed, D. P. Nair, T. Gong, S. M. Reed, and C. N. Bowman, 'Tailorable and programmable liquid-crystalline elastomers using a two-stage thiol-acrylate reaction', *RSC Adv*, vol. 5, no. 25, pp. 18997–19001, 2015, doi: 10.1039/c5ra01039j.

[14] J. G. Coats, B. Maktabi, M. S. Abou-Dahech, and G. Baki, 'Blue Light Protection, Part I—Effects of blue light on the skin', *J Cosmet Dermatol*, vol. 20, no. 3, pp. 714–717, Mar. 2021, doi: 10.1111/JOCD.13837.

[15] P. Knuschke, 'UV exposure', in *Kanerva's Occupational Dermatology*, Springer International Publishing, 2019, pp. 1145–1178. doi: 10.1007/978-3-319-68617-2_76/TABLES/17.

[16] E. Gregersen and The Editors of Encyclopaedia Britannica, 'Polymer | Description, Examples, Types, Material, Uses, & Facts | Britannica'. Accessed: Jul. 09, 2024. [Online]. Available: https://www.britannica.com/science/polymer

[17] S. Perkins, 'Explainer: What are polymers?' Accessed: Jul. 09, 2024. [Online]. Available: https://www.snexplores.org/article/explainer-what-are-polymers

[18] 'monomer noun - Definition, pictures, pronunciation and usage notes | Oxford Advanced Learner's Dictionary at OxfordLearnersDictionaries.com'. Accessed: Jul. 09, 2024. [Online]. Available: https://www.oxfordlearnersdictionaries.com/definition/english/monomer

[19] R. N. Robertson, *The lively membranes*. Cambridge University Press, 1983.

[20] 'Introduction to Liquid Crystals'. Accessed: Jul. 09, 2024. [Online]. Available: https://uh.edu/~chembi/liquidcrystals.pdf

[21] M. ALLABY, *A Dictionary of Earth Sciences*. Oxford University Press, 2008. doi: 10.1093/ACREF/9780199211944.001.0001.

[22] 'Actuators: what is it, definition, types and how does it work – Progressive Automations'. Accessed: Jul. 09, 2024. [Online]. Available: https://www.progressiveautomations.com/pages/actuators

[23] D. E. Reichle, *The Global Carbon Cycle and Climate Change: Scaling Ecological Energetics from Organism to the Biosphere*. Elsevier, 2023. doi: 10.1016/C2022-0-00267-1.

[24] S. C. Moldoveanu and V. David, *Selection of the HPLC Method in Chemical Analysis, Chapter 4: Basic Information Regarding the HPLC Techniques*. 2017. Accessed: Jul. 09, 2024. [Online]. Available: http://www.sciencedirect.com:5070/book/9780128036846/selection-of-the-hplc-method-in-chemical-analysis

[25] J. Ashley and P. Manikova, 'Fluorescent sensors', *Fundamentals of Sensor Technology: Principles and Novel Designs*, pp. 147–161, Jan. 2023, doi: 10.1016/B978-0-323-88431-0.00022-3.

[26] J. M. ; K. N. ; W. G. ; L. M. ; E. S. ; J. K. ; G. Wignall *et al.*, 'The mesomorphic state', in *Physical Properties of Polymers*, Cambridge University Press, 2004, pp. 316–380. doi: 10.1017/CBO9781139165167.006.

[27] Zhang, Gleeson, and HF, 'Understanding liquid crystal order parameters deduced from different vibrations in polarised Raman spectroscopy', 2018, doi: 10.1080/02678292.2018.1485980.

[28] 'Pi Definition & Meaning - Merriam-Webster'. Accessed: Jul. 16, 2024. [Online]. Available: https://www.merriam-webster.com/dictionary/pi

[29] D. Liu, L. Liu, P. R. Onck, D. J. Broer, and P. Palffy-Muhoray, 'Reverse switching of surface roughness in a self-organized polydomain liquid crystal coating', *Proc Natl Acad Sci U S A*, vol. 112, no. 13, pp. 3880–3885, Mar. 2015, doi: 10.1073/pnas.1419312112.

[30] Z. Liu, H. K. Bisoyi, Y. Huang, M. Wang, H. Yang, and Q. Li, 'Thermo- and Mechanochromic Camouflage and Self-Healing in Biomimetic Soft Actuators Based on Liquid Crystal Elastomers', *Angewandte Chemie - International Edition*, vol. 61, no. 8, Feb. 2022, doi: 10.1002/anie.202115755.

[31] M. Robert H. Shmerling, 'Wondering about goosebumps? Of course you are', *Harvard Health Publishing*, 2020. Accessed: Apr. 22, 2024. [Online]. Available: https://www.health.harvard.edu/blog/wondering-about-goosebumps-of-course-you-are-2020080320688

[32] N. Shirtcliffe, P. Comanns, C. Hamlett, P. Roach, and S. Atherton, 'The Effect of Roughness Geometry on Superhydrophobicity and Related Phenomena', *Comprehensive Nanoscience and Nanotechnology*, vol. 1–5, pp. 291–308, Jan. 2019, doi: 10.1016/B978-0-12-803581-8.10465-5.

[33] K. N. Long, M. L. Dunn, and H. Jerry Qi, 'Mechanics of soft active materials with phase evolution', *Int J Plast*, vol. 26, no. 4, pp. 603–616, Apr. 2010, doi: 10.1016/j.ijplas.2009.10.005.

[34] P. K. Misra, 'Complex Structures', in *Physics of Condensed Matter*, Elsevier, 2012, pp. 567–597. doi: 10.1016/b978-0-12-384954-0.00017-7.

[35] J. P. F. Lagerwall and G. Scalia, 'A new era for liquid crystal research: Applications of liquid crystals in soft matter nano-, bio- and microtechnology', *Current Applied Physics*, vol. 12, no. 6, pp. 1387–1412, Nov. 2012, doi: 10.1016/j.cap.2012.03.019.

[36] S. W. Ula, N. A. Traugutt, R. H. Volpe, R. R. Patel, K. Yu, and C. M. Yakacki, 'Liquid crystal elastomers: an introduction and review of emerging technologies', *Liq Cryst Rev*, vol. 6, no. 1, pp. 78–107, Jan. 2018, doi: 10.1080/21680396.2018.1530155.

[37] P. J. Collings and M. Hird, *Introduction to liquid crystals: Chemistry and physics*, 1st Edition. London: CRC Press, 1997. doi: 10.1201/9781315272801/INTRODUCTION-LIQUID-CRYSTALS-PETER-COLLINGS-JOHN-GOODBY-GEORGE-GRAY-MICHAEL-HIRD.

[38] F. Brömmel, D. Kramer, and H. Finkelmann, 'Preparation of Liquid Crystalline Elastomers', in *Adv Polym Sci*, vol. 250, Springer, Berlin, Heidelberg, 2012, pp. 1–48. doi: 10.1007/12_2012_168.

[39] S. K. Prasad, 'Photostimulated and Photosuppressed Phase Transitions in Liquid Crystals', *Angewandte Chemie International Edition*, vol. 51, no. 43, pp. 10708–10710, Oct. 2012, doi: 10.1002/ANIE.201204619.

[40] T. J. White and D. J. Broer, 'Programmable and adaptive mechanics with liquid crystal polymer networks and elastomers', *Nature Materials 2015 14:11*, vol. 14, no. 11, pp. 1087–1098, Oct. 2015, doi: 10.1038/nmat4433.

[41] G. Fernández, 'Liquid-crystal polymers: Exotic actuators', *Nat Mater*, vol. 12, no. 1, pp. 12–14, 2013, doi: 10.1038/NMAT3526.

[42] D. C. Hoekstra *et al.*, 'Wavelength-Selective Photopolymerization of Hybrid Acrylate-Oxetane Liquid Crystals', *Angewandte Chemie - International Edition*, vol. 60, no. 19, pp. 10935–10941, May 2021, doi: 10.1002/anie.202101322.

[43] A. El-Ghayoury, C. Boukaftane, B. De Ruiter, and R. Van Der Linde, 'Ultraviolet-ultraviolet dual-cure process based on acrylate oxetane monomers', *J Polym Sci A Polym Chem*, vol. 41, no. 4, pp. 469–475, Feb. 2003, doi: 10.1002/pola.10600.

[44] Krzysztof Matyjaszewski and Thomas P. Davis, *Handbook of Radical Polymerization*. John Wiley & Sons, 2002. doi: 10.1002/0471220450.

[45] 'What is free radical polymerization? types, characteristics, reaction mechanism, and typical methods with examples', FUJIFILM Wako Chemicals Europe GmbH. Accessed: Apr. 25, 2024. [Online]. Available: https://specchem-wako.fujifilm.com/europe/en/information/technical-info/radical-polymerizations/

[46] M. Cioffi, 'Rheokinetics', University of Groningen, Groningen, 2022.

[47] M. S. M. Alger, *Polymer science dictionary*. London: Elsevier Applied Science, 1989. Accessed: Apr. 25, 2024. [Online]. Available: https://search.worldcat.org/title/17804399

[48] M. A. Macchione, D. Aristizabal Bedoya, F. N. Figueroa, and M. C. Strumia, 'Synthetic and semi-synthetic polymers for pharmaceutical applications', *Advances and Challenges in Pharmaceutical Technology: Materials, Process Development and Drug Delivery Strategies*, pp. 45–73, Jan. 2021, doi: 10.1016/B978-0-12-820043-8.00005-0.

[49] P. K. Deb, S. F. Kokaz, S. N. Abed, A. Paradkar, and R. K. Tekade, 'Pharmaceutical and Biomedical Applications of Polymers', *Basic Fundamentals of Drug Delivery*, pp. 203–267, Jan. 2019, doi: 10.1016/B978-0-12-817909-3.00006-6.

[50] V. K. Dhote *et al.*, 'Fundamentals of Polymers Science Applied in Pharmaceutical Product Development', *Basic Fundamentals of Drug Delivery*, pp. 85–112, Jan. 2019, doi: 10.1016/B978-0-12-817909-3.00003-0.

[51] L. S. Litvinova, 'SYNTHETIC POLYMERS | Thin-Layer (Planar) Chromatography', *Reference Module in Chemistry, Molecular Sciences and Chemical Engineering*, Jan. 2013, doi: 10.1016/B978-0-12-409547-2.04944-1.

[52] G. Klaerner and R. Padmanabhan, 'Multi-Step/Step-Wise Polymerization of Well-Defined Oligomers', *Reference Module in Materials Science and Materials Engineering*, Jan. 2016, doi: 10.1016/B978-0-12-803581-8.03768-1.

[53] K. Naka, 'Monomers, Oligomers, Polymers, and Macromolecules (Overview)', in *Encyclopedia of Polymeric Nanomaterials*, Springer, Berlin, Heidelberg, 2014, pp. 1–6. doi: 10.1007/978-3-642-36199-9_237-1.

[54] 'Safety Data Sheet according to Regulation (EC) No. 1907/2006 (REACH)'. Accessed: Jul. 01, 2024. [Online]. Available: https://shop.synthon-chemicals.com/en/REACTIVE-MESOGENS/BIFUNCTIONAL/BENZOATES/1-4-Bis-4-6-acryloyloxyhexyloxy-benzoyloxy-2-methylbenzene.html

[55] W.-S. Wei, Y. Xia, S. Ettinger, S. Yang, and A. G. Yodh, 'Molecular heterogeneity drives reconfigurable nematic liquid crystal drops', *Nature*, vol. 576, p. 433, doi: 10.1038/s41586-019-1809-8.

[56] H. J. Hong and S. Y. Park, 'Effects of network structure of main-chain liquid crystal elastomer on its thermal actuation performance', *Journal of Industrial and Engineering Chemistry*, vol. 110, pp. 424–433, Jun. 2022, doi: 10.1016/J.JIEC.2022.03.017.

[57] H. Kim, J. M. Boothby, S. Ramachandran, C. D. Lee, and T. H. Ware, 'Tough, Shape-Changing Materials: Crystallized Liquid Crystal Elastomers', 2017, doi: 10.1021/acs.macromol.7b00567.

[58] Y. J. Jeong and S. Y. Park, 'Light-Responsive Actuator of Azobenzene-Containing Main-Chain Liquid Crystal Elastomers with Allyl Sulfide Dynamic Exchangeable Linkages', *ACS Appl Mater Interfaces*, vol. 16, no. 2, pp. 2788–2801, Jan. 2024, doi: 10.1021/ACSAMI.3C17068/SUPPL_FILE/AM3C17068_SI_007.MP4.

[59] G. SOCRATES, *Infrared and Raman Characteristic Group Frequencies*, Third Edition., vol. Tables and Charts. JOHN WILEY & SONS, LTD, 2001.

[60] P. Boisaubert, N. Kébir, A.-S. Schuller, and F. Burel, 'Photo-crosslinked Non- Isocyanate Polyurethane Acrylate (NIPUA) coatings through a transurethane polycondensation approach', *Polymer (Guildf)*, vol. 206, 2020, doi: 10.1016/j.polymer.2020.122855ï.

[61] B. De Ruiter, A. El-Ghayoury, H. Hofmeier, U. S. Schubert, and M. Manea, 'Two-step curing processes for coating application', in *Progress in Organic Coatings*, Feb. 2006, pp. 154–159. doi: 10.1016/j.porgcoat.2005.09.011.

[62] J. M. McCracken, B. R. Donovan, K. M. Lynch, and T. J. White, 'Molecular Engineering of Mesogenic Constituents Within Liquid Crystalline Elastomers to Sharpen Thermotropic Actuation', *Adv Funct Mater*, vol. 31, no. 16, Apr. 2021, doi: 10.1002/adfm.202100564.

[63] X. Wang *et al.*, 'Braided Liquid Crystal Elastomer Fiber Actuator with Programmable Deformation for Artificial Muscles', *Adv Mater Technol*, vol. 8, no. 19, p. 2300814, Oct. 2023, doi: 10.1002/ADMT.202300814.

[64] L. Zhao *et al.*, 'Bio-Inspired Soft-Rigid Hybrid Smart Artificial Muscle Based on Liquid Crystal Elastomer and Helical Metal Wire', *Small*, vol. 19, no. 17, p. 2206342, Apr. 2023, doi: 10.1002/SMLL.202206342.

[65] M. T. Sims, L. C. Abbott, R. M. Richardson, J. W. Goodby, and J. N. Moore, 'Considerations in the determination of orientational order parameters from X-ray scattering experiments', *Liq Cryst*, vol. 46, no. 1, pp. 11–24, Jan. 2019, doi: 10.1080/02678292.2018.1455227.

[66] S. Okamoto, S. Sakurai, and K. Urayama, 'Effect of stretching angle on the stress plateau behavior of main-chain liquid crystal elastomers', *This journal is Cite this: Soft Matter*, vol. 17, p. 3128, 2021, doi: 10.1039/d0sm02244f.

[67] Lugger and Sean, 'Thermoplastic Liquid Crystal Elastomer Soft Actuators', Eindhoven University of Technology, Eindhoven, 2023. [Online]. Available: www.tue.nl/taverne

[68] J. Lilly Mercy and S. Prakash, 'Investigation of damage processes of a microencapsulated self-healing mechanism in glass fiber-reinforced polymers', *Modelling of Damage Processes in Biocomposites, Fibre-Reinforced Composites and Hybrid Composites*, pp. 133–151, Jan. 2019, doi: 10.1016/B978-0-08-102289-4.00008-4.

[69] J. A. F. F. Rocco, J. E. S. Lima, V. L. Lourenço, N. L. Batista, E. C. Botelho, and K. Iha, 'Dynamic mechanical properties for polyurethane elastomers applied in elastomeric mortar', *J Appl Polym Sci*, vol. 126, no. 4, pp. 1461–1467, Nov. 2012, doi: 10.1002/app.36847.

[70] J. Smorawska, M. Włoch, and E. Głowińska, 'Structure–Property Relationship and Multiple Processing Studies of Novel Bio-Based Thermoplastic Polyurethane Elastomers', *Materials*, vol. 16, no. 18, Sep. 2023, doi: 10.3390/ma16186246.

[71] S. Mok, C. M. Boghdady, and C. Moraes, 'Probing tissue mechanics at the cellular-length scale in cancer microenvironments', in *Micro and Nano Systems for Biophysical Studies of Cells and Small Organisms*, Academic Press, 2021, pp. 71–103. doi: 10.1016/B978-0-12-823990-2.00004-0.

[72] P. Du and X. Wang, *Recent Advances in Smart Self-healing Polymers and Composites*. Elsevier, 2015. Accessed: Jul. 17, 2024. [Online]. Available: http://www.sciencedirect.com:5070/book/9781782422808/recent-advances-in-smart-self-healing-polymers-and-composites

[73] R. F. Landel and L. E. Nielsen, *Mechanical Properties of Polymers and Composites*. CRC Press, 1993. doi: 10.1201/B16929.

[74] A. X. H. Yong, G. D. Sims, S. J. P. Gnaniah, S. L. Ogin, and P. A. Smith, 'Heating rate effects on thermal analysis measurement of Tg in composite materials', *Advanced Manufacturing: Polymer & Composites Science*, vol. 3, no. 2, pp. 43–51, Apr. 2017, doi: 10.1080/20550340.2017.1315908.

[75] H. Xie, C. Li, and Q. Wang, 'A critical review on performance and phase separation of thermosetting epoxy asphalt binders and bond coats', *Constr Build Mater*, vol. 326, Apr. 2022, doi: 10.1016/j.conbuildmat.2022.126792.

[76] I. A. Ansari, G. A. Gupta, J. Ramkumar, and K. K. Kar, 'Fly ash-mixed polymeric media for abrasive flow machining process', in *Handbook of Fly Ash*, Butterworth-Heinemann, 2022, pp. 681–713. doi: 10.1016/B978-0-12-817686-3.00003-7.

[77] A. A. Karim, M. H. Norziah, and C. C. Seow, 'Methods for the study of starch retrogradation', *Food Chem*, vol. 71, no. 1, pp. 9–36, Oct. 2000, doi: 10.1016/S0308-8146(00)00130-8.

[78] J. D. Ferry, *Viscoelastic properties of polymers*, 3rd edition. John Wiley & Sons, Inc., 1980. Accessed: Jul. 17, 2024. [Online]. Available: https://www.wiley.com/en-nl/Viscoelastic+Properties+of+Polymers%2C+3rd+Edition-p-9780471048947

[79] Z. Carl H. and B. Peter, *Comprehensive Composite Materials II*, vol. II. Elsevier, 2018. Accessed: Jul. 17, 2024. [Online]. Available: http://www.sciencedirect.com:5070/referencework/9780081005347/comprehensive-composite-materials-ii

[80] H. J. Farre-Kaga, M. O. Saed, and E. M. Terentjev, 'Dynamic Pressure Sensitive Adhesion in Nematic Phase of Liquid Crystal Elastomers', *Adv Funct Mater*, vol. 32, no. 12, Mar. 2022, doi: 10.1002/adfm.202110190.

[81] M. O. Saed, A. H. Torbati, C. A. Starr, R. Visvanathan, N. A. Clark, and C. M. Yakacki, 'Thiol-acrylate main-chain liquid-crystalline elastomers with tunable thermomechanical properties and actuation strain', *J Polym Sci B Polym Phys*, vol. 55, no. 2, pp. 157–168, Jan. 2017, doi: 10.1002/polb.24249.

[82] A. Hotta and E. M. Terentjev, 'Dynamic soft elasticity in monodomain nematic elastomers', *European Physical Journal E*, vol. 10, no. 4, pp. 291–301, Apr. 2003, doi: 10.1140/epje/i2002-10005-5.

[83] S. R. Flury, A. E. Jaskot, H. C. Ferguson, R. Brighenti, and M. Pancrazio Cosma□, 'Smart actuation of liquid crystal elastomer elements: cross-link density-controlled response', 2021, doi: 10.1088/1361-665X/ac34bf.

[84] M. W. Davidson, 'Polarized Light Microscopy - The First Order (Full Wave) Retardation Plate | Olympus LS', EVIDENT. Accessed: Jul. 25, 2024. [Online]. Available: https://www.olympus-lifescience.com/en/microscope-resource/primer/techniques/polarized/firstorderplate/

[85] H. Bai, S. Li, and R. F. Shepherd, 'Elastomeric Haptic Devices for Virtual and Augmented Reality', *Adv Funct Mater*, vol. 31, no. 39, p. 2009364, Sep. 2021, doi: 10.1002/ADFM.202009364.

[86] X. Dong *et al.*, 'Multisensory Flexible Braille Interactive Device Based on Liquid Crystal Elastomers', *ACS Appl Electron Mater*, vol. 4, no. 8, pp. 3834–3840, Aug. 2022, doi: 10.1021/acsaelm.2c00458.

[87] S. Tibbits, '4D Printing: Multi-Material Shape Change', *Architectural Design*, vol. 84, no. 1, pp. 116–121, Jan. 2014, doi: 10.1002/AD.1710.

[88] K. L. Sampson *et al.*, 'Multimaterial Vat Polymerization Additive Manufacturing', *ACS Appl Polym Mater*, vol. 3, no. 9, pp. 4304–4324, Sep. 2021, doi: 10.1021/ACSAPM.1C00262/ASSET/IMAGES/LARGE/AP1C00262_0010.JPEG.

[89] M. Chen *et al.*, 'Recent Advances in 4D Printing of Liquid Crystal Elastomers', *Advanced Materials*, vol. 35, no. 23, p. 2209566, Jun. 2023, doi: 10.1002/ADMA.202209566.

[90] L. Ren *et al.*, 'Programming Shape-Morphing Behavior of Liquid Crystal Elastomers via Parameter-Encoded 4D Printing', *Cite This: ACS Appl. Mater. Interfaces*, vol. 12, pp. 15562–15572, 2020, doi: 10.1021/acsami.0c00027.

[91] K. Kim *et al.*, '4D Printing of Hygroscopic Liquid Crystal Elastomer Actuators', *Small*, vol. 17, no. 23, p. 2100910, Jun. 2021, doi: 10.1002/SMLL.202100910.

# A

# SUPPORTING INFORMATION

## A.1 Chemical Structure of the Compounds Used

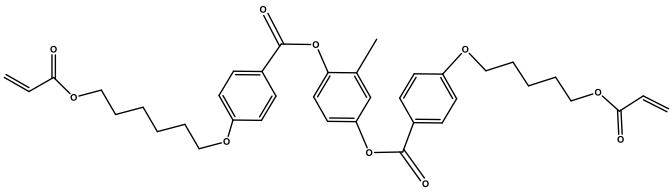

Figure A 1 - Chemical structure of the RM82 LC mesogen.

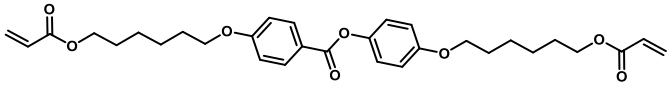

Figure A 2 - Chemical structure of the C6BAPE LC mesogen.

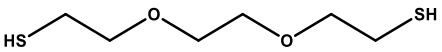


Figure A 3 - Chemical structure of the chain extender DODT.

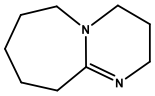


Figure A 4 - Chemical structure of the catalyst DBU.

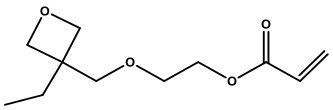

Figure A 5 - Chemical structure of the acrylate-oxetane crosslinker.

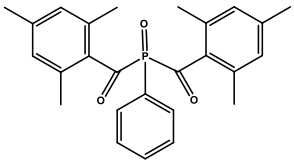

Figure A 6 - Chemical structure of the free-radical photo-initiator Irgacure 819.

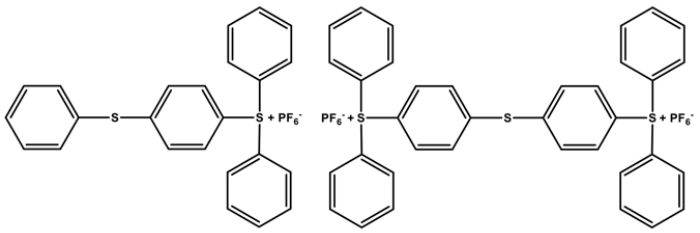


Figure A 7 - Chemical structure of the cationic photo-initiator THPS.

## A.2 Synthesis of the Acrylate-oxetane Crosslinker

The synthesis of the acrylate-oxetane crosslinker followed the procedure of El-Ghayoury A. *et al.* [43]. First, in a 100 mL flask placed in an ice bath and under an argon atmosphere, 1.5 g or 9.36 mmol of 3-(Hydroxyethylmethoxy)-3-ethyloxetane were dissolved in 20 mL of DCM. To this solution 2 mL of triethylamine (TEA) catalyst were added. Next, 1.0 g or 0.89 ml or 11.04 mmol of acryloylchloride was combined in the mixture through the usage of a drop funnel. The resulting mixture was stirred for 30 min at 0 °C. Then, it was stirred overnight at RT. The following day, 200 mL of Water was added, and the compound was extracted with 3 x 100 mL of DCM. The organic layers were collected and dried over $MgSO_4$, and the solvent was evaporated in a vacuum. Finally, 1.45 g or 72% of acrylate-oxetane crosslinker was obtained as a colourless oil.

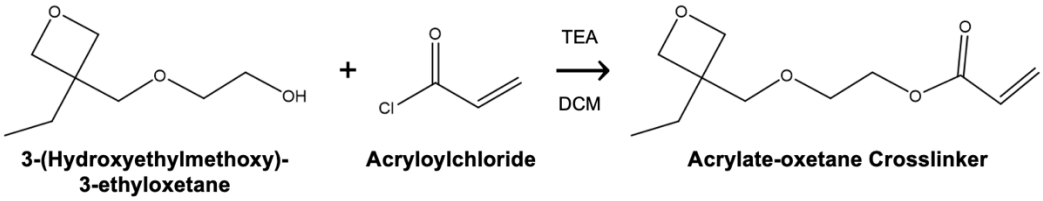


Figure A 8 - Chemical Reaction for the synthesis of the acrylate-oxetane crosslinker.

## A.3 Laboratory Procedure of the TWSP Method

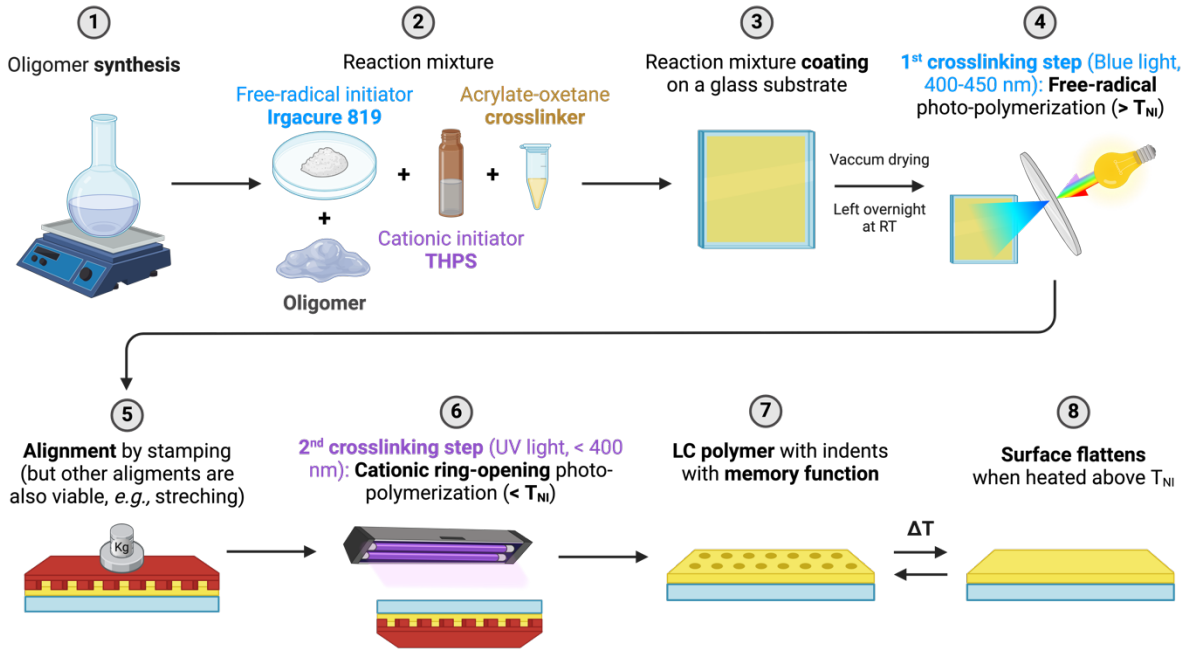


Figure A 9 - Schematic of the laboratory procedure of the TWSP method. Note that this procedure is representative of an oligomer-based and stamping approach. For a one-pot approach, the oligomer synthesis step is irradicated, and step two, now the first, will not include an oligomer in the reaction mixture but instead an LC mesogen and a chain extender.

## A.4 Optimisation of the Photo-initiators' Concentration & Exposure Doses for Each Wavelength of the TWSP Method

The idea for this research and development of this procedure and material stemmed, as many others do, from the inspiration of combining essentially two distinct working physical principles, whose viability was previously proven and reported in other works in literature.

The earliest stage of this research consisted of replicating the works of El-Ghayoury A. *et al.* [43] and Barteld de Ruiter *et al.* to test the feasibility of the acrylate-oxetane crosslinker for a two-stage photo-polymerisation. The principle for the two reactions is identical to what was previously explained in section 3.1, in the sense that the first step consists of the free-radical polymerisation of acrylate groups under blue light irradiation and the second of the cationic ring-opening polymerisation of oxetanes under UV exposure. However, in this case, no LC molecules were added to the mixture, the goal was for acrylate-oxetane molecules to crosslink with each other.

When mimicking the exact same concentrations and exposure doses as the ones used in the work of El-Ghayoury A. *et al.* [43] only conversion of acrylates was observed and not of oxetanes. Moreover, there was still a major excess of acrylates in the system, as their conversion was lower than optimal. To correct this, various trials experimenting with different concentrations of each initiator and distinct exposure doses in both steps were performed. In the end, the best result that was more closely compared to the one from literature (Figure A 10 (A)) was the one shown in Figure A 10 (B). In this case, the concentrations used were 88 w.% of acrylate-oxetane, 4 wt. % of Irgacure 819 and 8 wt. % of THPS, and the exposure doses were 20 mW / cm² for 5 min in the first step (*i.e.*, blue light) and 30 mW / cm² for 10 min in the second (*i.e.*, UV light). Note that as Figure A 10 (B) presents, a longer than 10 min duration of UV light irradiation in the second stage does not lead to further conversion of oxetane groups.

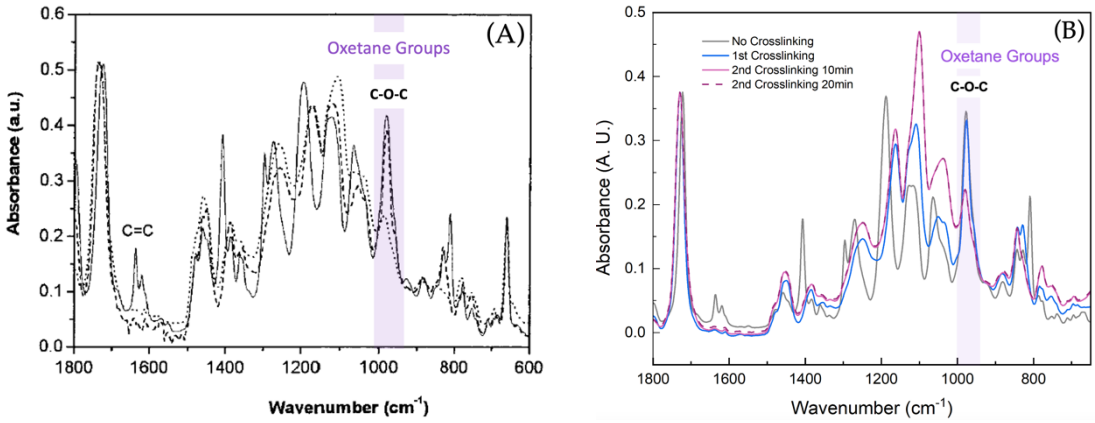


Figure A 10 - Infrared absorption spectra of the dual curing of acrylate-oxetane: (A) Spectra taken as reference from El-Ghayoury A. *et al.* [43]: (—) before cure; (- - -) step 1; and (. . .) step 2. (B) Measured spectra in our research: (—) No crosslinking; (—) 1st Crosslinking, 5 min; (—) 2nd Crosslinking, 10 min and (- - -) 2nd Crosslinking, 20 min. Purple highlighted is the conversion of oxetanes seen through the comparative decrease in intensity of the C-O-C peak.

## A.5 NMR Analysis of the Oligomers

NMR measurements were performed to determine the DP, *i.e.*, average chain length, and Mn of the oligomers. The extraction of the spectra of the *olgRM82-1*, *olgRM82-2*, *olgRM82-3*, and *olgC6BAPE-1*, shown in Figure A 12, Figure A 13, Figure A 14, and Figure A 15, respectively. The Mnova software was used to analyse the collected data.

In an RM82 monomer, there is a ratio of four aromatic protons of the mesogenic core per two acrylic proton groups (Figure A 11). Moreover, the intensity of the peaks comes from the number of protons in the molecule. In an oligomer, multiple RM82 monomers will be connected by DODT, forming the middle part of the molecule. Yet since, in this case, a ratio of more RM82 relative to DODT was followed, the ends of the oligomer produced will always be made of two acrylate groups, just like in the RM82 monomer. As such, to correctly calculate the DP, this 4:2 or 2:1 ratio must be kept. In order to do so, first, the signals at 6.41 (Figure A 12 b), 6.12 (Figure A 12 c) and 5.83 ppm (Figure A 12 d) were normalised to 1. Note that these peaks correspond to the protons on the acrylate groups. Then, these peaks, as well as the peak at 8.13 ppm (Figure A 12 a), which corresponds to the four protons of the mesogenic core, were all integrated. Through these integrals, the following calculations were done to find the DP and Mn of the *olgRM82-1*:

$$DP_{olgRM82-1} = \frac{24.26}{2} = 12.13 \approx 12\ repeating\ units\ (r.u.)$$

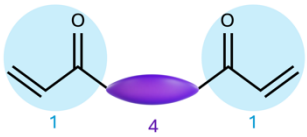


Figure A 11 – Illustration of an RM82 LC monomer: in purple is represented the core of the molecule, where the number 4 relates to the number of aromatic protons of the mesogenic core; in blue are depicted the two acrylate groups always present in this monomer type, each acylate possesses one acrylic proton group.

$$Mn_{olgRM82-1} = (Mn_{r.u.} \times DP) - M_{DODT} =$$
$$= [(672.77 + 182.30) \times 12.13] - 182.30 = 10\,182.70\ g/mol$$

Where $Mn_{r.u.} = M_{RM82} + M_{DODT}$. Note that the need for the subtraction of the molecular mass of the DODT ($M_{DODT}$) comes from the fact that in the oligomer there is always one less DODT section compared to the number of RM82 sections.

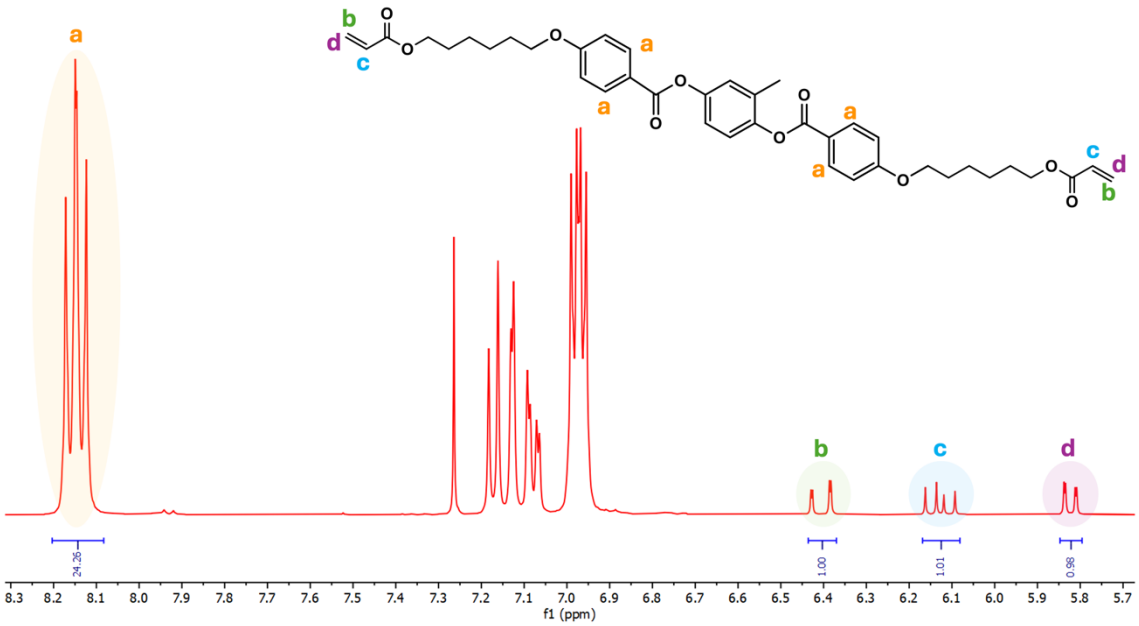


Figure A 12 - $^{1}$H-NMR spectrum of *olgRM82-1*, where **a** relates to four aromatic protons of the mesogenic core, while **b**, **c**, and **d** each correspond to two protons of the acrylate groups at the two extremities of the monomer.

Homologous calculations can be carried out for the *olgRM82-2*:

$$DP_{olgRM82-2} = \frac{26.81}{2} = 13.41 \approx 13\ r.u.$$

$$Mn_{olgRM82-2} = (Mn_{r.u.} \times DP) - M_{DODT} = (855.07 \times 13.41) - 182.30 = 11\,284.19\ g/mol$$

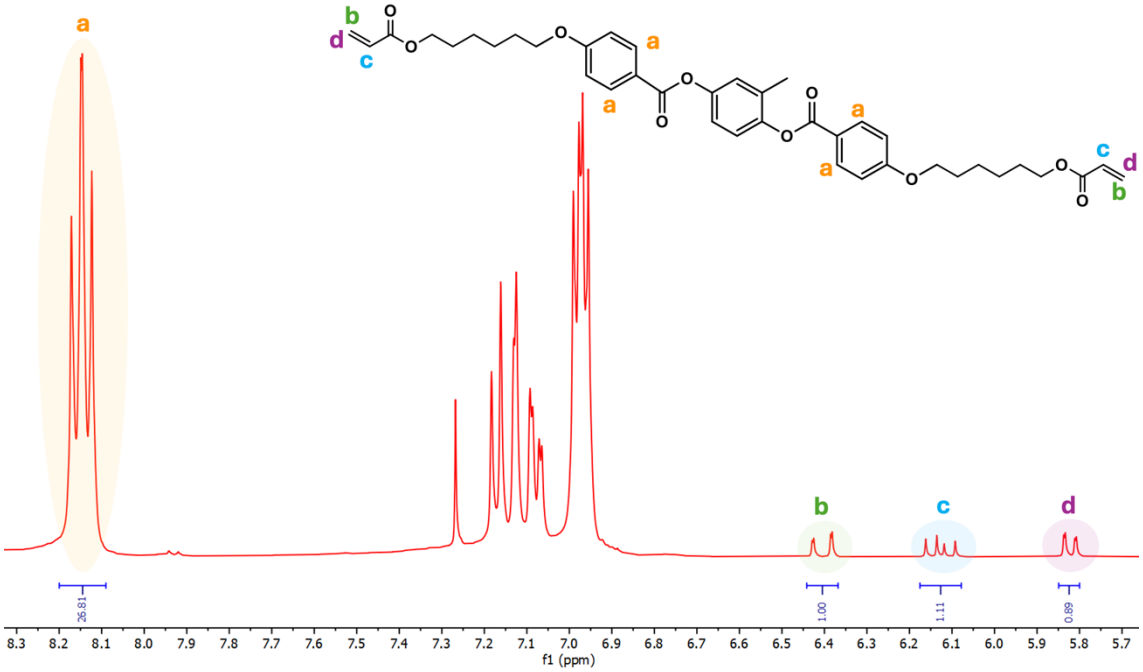


Figure A 13 - $^{1}$H-NMR spectrum of *olgRM82-2*, where **a** relates to four aromatic protons of the mesogenic core, while **b**, **c**, and **d** each correspond to two protons of the acrylate groups at the two extremities of the monomer.

Homologous calculations can be carried out for the *olgRM82-3*:

$$DP_{olgRM82-3} = \frac{26.83}{2} = 13.42 \approx 13\ r.u.$$

$$Mn_{olgRM82-3} = (Mn_{r.u.} \times DP) - M_{DODT} = (855.07 \times 13.42) - 182.30 = 11\,288.46\ g/mol$$

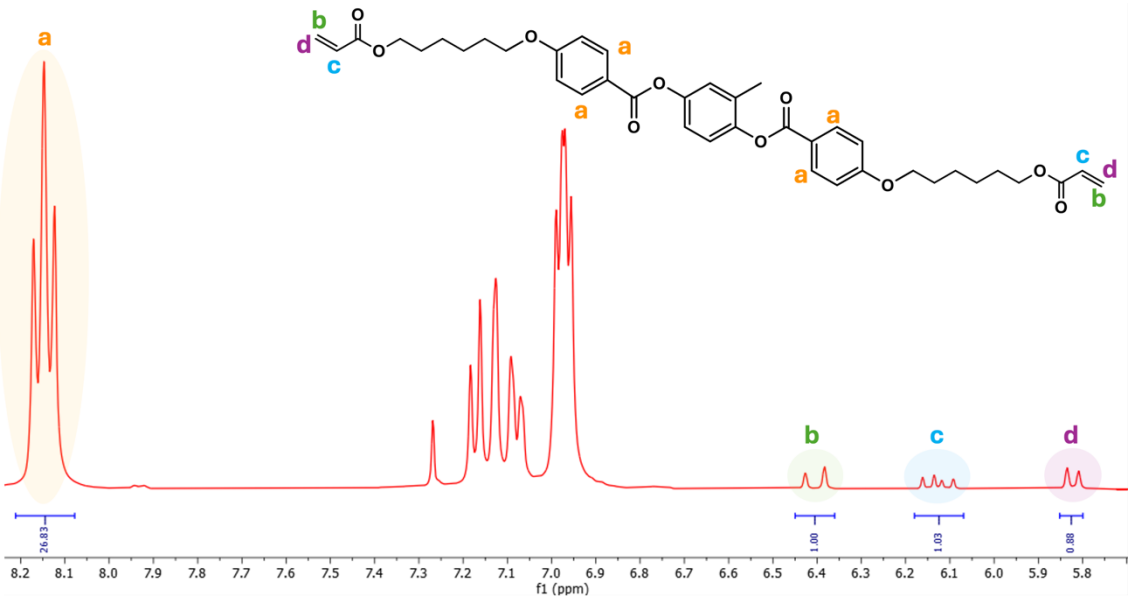


Figure A 14 - $^{1}$H-NMR spectrum of *olgRM82-3*, where **a** relates to four aromatic protons of the mesogenic core, while **b**, **c**, and **d** each correspond to two protons of the acrylate groups at the two extremities of the monomer.

Contrary to the previous cases where the LC mesogen was RM82, when it is C6BAPE instead, the DP corresponds directly to the integral of the aromatic protons peak since the ratio in the monomer is two protons of the mesogenic core per two protons of the two acrylate groups (*i.e.*, 1:1 ratio). The remain calculus are similar with just the molecular weight being different since the mesogen changed:

$$DP_{olgC6BAPE-1} = 10.81 \approx 11\ r.u.$$

$$Mn_{olgC6BAPE-1} = (Mn_{r.u.} \times DP) - M_{DODT} =$$
$$= [(538.64 + 182.30) \times 10.81] - 182.30 = 7\,611.06\ g/mol$$

Where $Mn_{r.u.} = M_{C6BAPE} + M_{DODT}$. Note that the need for the subtraction of the $M_{DODT}$ comes from the fact that in the oligomer there is always one less DODT section compared to the number of C6BAPE sections.

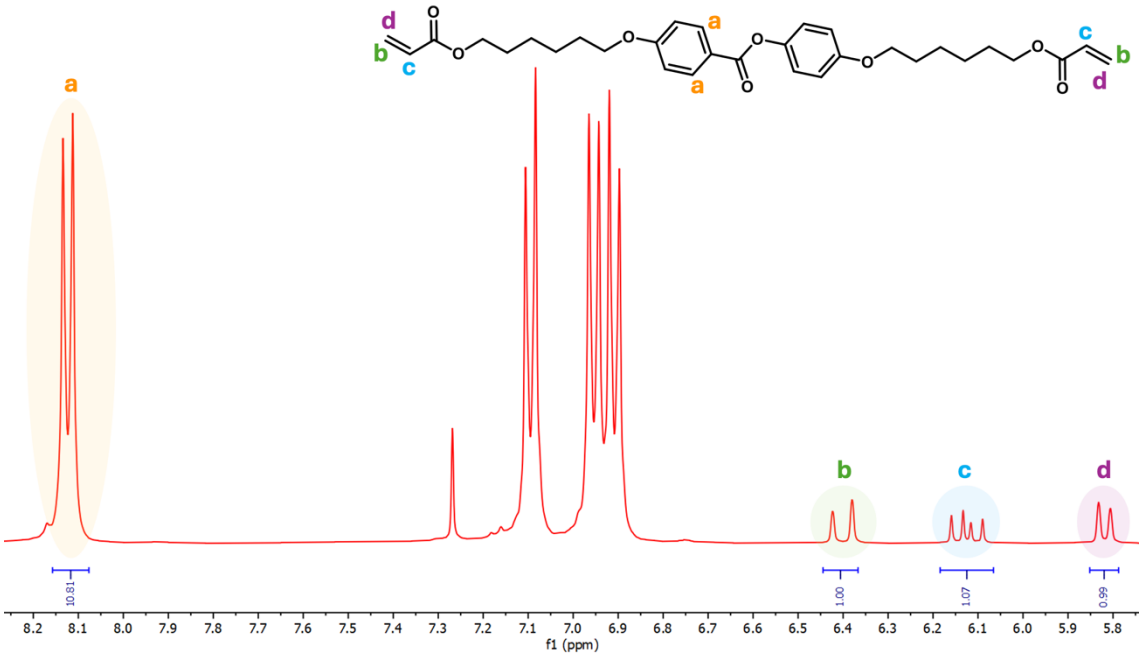


Figure A 15 - $^{1}$H-NMR spectrum of *olgC6BAPE-1*, where **a** relates to two aromatic protons of the mesogenic core, while **b**, **c**, and **d** each correspond to two protons of the acrylate groups at the two extremities of the monomer.

## A.6 GPC Analysis of the Oligomers

To determine the PDI, GPC measurements were effectuated. The different-sized mesogenic cores of RM82 or C6BAPE were detected through their absorptions at a 254 nm wavelength. Note that the detector used was PDA. Figure A 16 shows the normalised absorption as a function of time plot, made from the data extracted from the GPC measurement of each synthesised oligomer. The GPC results were also more neatly organised in Table A 1 to facilitate interpretation. In it the various molecular weights are presented. The fraction of the Mw as the numerator and the Mn as the denominator gives the value of the PDI of each oligomer.

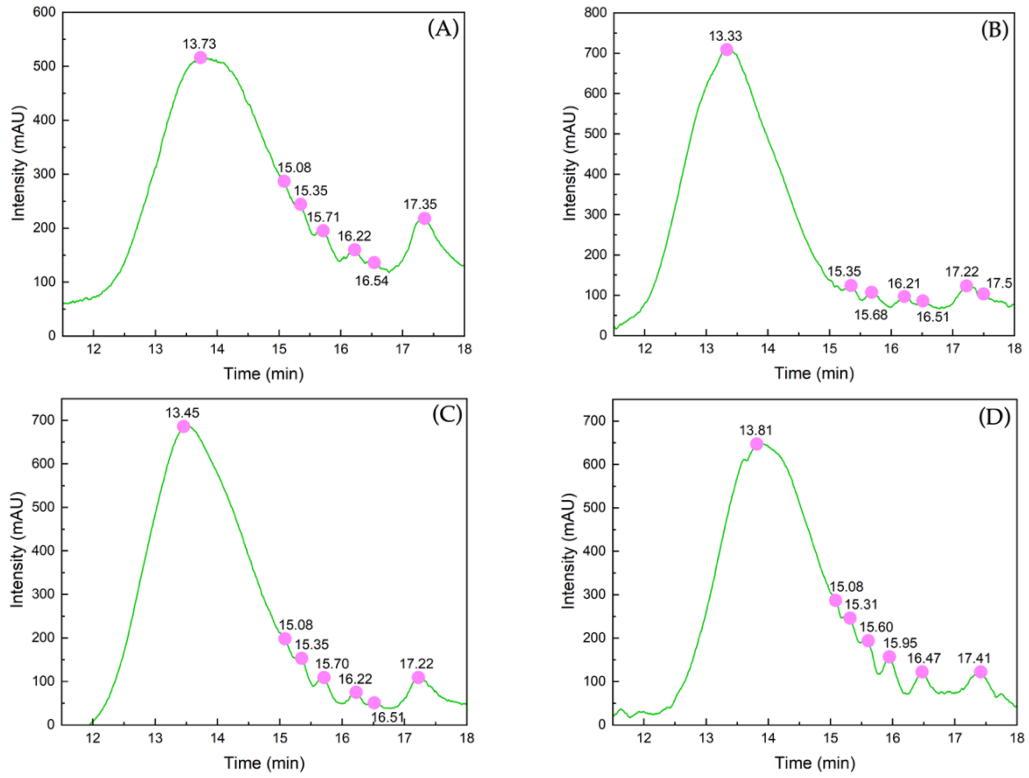


Figure A 16 - GPC plots of (A) *olgRM82-1*, (B) *olgRM82-2*, (C) *olgRM82-3*, (D) *olgC6BAPE-1*.

Comparing the PDI's it can be seen that the oligomer with the C6BAPE mesogen showed the highest polydispersity, and amongst the two RM82-based oligomers, the first was the less size dispersed.

Table A 1 - GPC analysis results for the three oligomers. Where Mn is the number average molecular weight, Mw is the weight average molecular weight, and Mz is Z average molecular weight.

| Oligomer | Mn [g/mol] | Mw [g/mol] | Mz [g/mol] | Mw/Mn | PDI [A. U.] |
|---|---|---|---|---|---|
| *olgRM82-1* | 13 944 | 33 382 | 53 220 | 2.39393 | 2.39 |
| *olgRM82-2* | 18 628 | 45 813 | 73 569 | 2.45939 | 2.46 |
| *olgRM82-3* | 15 597 | 37 398 | 59 736 | 2.39773 | 2.40 |
| *olgC6BAPE-1* | 10 483 | 26 954 | 45 756 | 2.57130 | 2.57 |

## A.7 DSC Analysis of the Oligomers

To investigate the individual phase transitions of the oligomers DSC measurements were performed. Knowing the $T_{NI}$ of the material is crucial for the programming of the alignment. Figure A 17 exhibits the DSC endothermal and exothermal curves of each oligomer, with the respective $T_g$, $T_{SN}$, and $T_{NI}$ peaks marked.

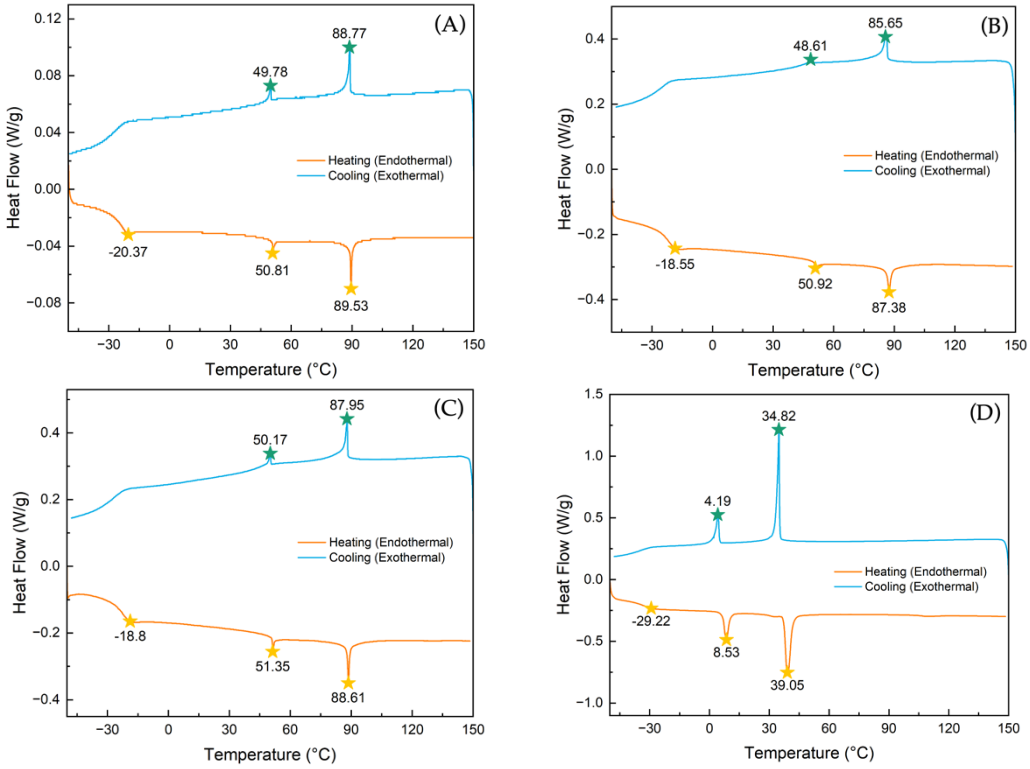


Figure A 17 - DSC Endo and Exo curves of (A) *olgRM82-1*, (B) *olgRM82-2*, (C) *olgRM82-3*, and (D) *olgC6BAPE-1*.

## A.8 Kinetics FTIR: Acrylates & Oxetanes Conversion

With kinetics FTIR measurements, it was possible to determine the intensity decrease of the acrylates peak at 1410 $cm^{-1}$ during the first crosslinking step and of the oxetanes peak at 985 $cm^{-1}$ during the second crosslinking step. From this data, as shown in Figure A 18, it was then possible to calculate the conversion of each of these chemical groups over the irradiation time of the respective crosslinking step they react in, *i.e.*, 5 min for acrylates conversion and 20 min for oxetanes. The reason this measurement was done across 20 min and not 10 min for the second crosslinking step was to confirm that 10 min was indeed sufficient time for the conversion of oxetanes and that after 10 min, oxetanes did not react in a significant manner.

The fitting of these conversion curves was then performed to determine the conversion values. In Figure A 18 (A), exponential growth can be seen until around 1 min, and from then on, the curve goes down. Acrylates, once converted, cannot go back to being unreacted, so the exponential growth seen in the beginning corresponds to the real conversion of acrylates. On

the other hand, the decrease in conversion does not actually translate into an increase of unreacted acrylates but instead is related to the influence of the two adjacent neighbouring peaks, which influence this peak's intensity, inevitably pulling it up slightly and making it seem like its intensity is increasing, which is physically impossible. This is a common issue in kinetics FTIR since the resonant frequencies (or vibrational frequencies) at which absorbance occurs for different chemical bonds tend to influence and even overlap partially with each other. The reason this overlap only becomes significant after 1 min is due to the fact that the near disappearance of this acrylate peak makes it so that the side parts of the other peaks naturally fill that close to empty space. As for the curve of oxetane conversion, presented in Figure A 18 (B), the fit chosen was exponential asymptotic since the decrease in intensity of this peak is exponential in the beginning (approximately the first 3 min) and then saturates and becomes constant. Note that the oscillations observed result mostly from noise. From these fits, it was determined that the conversion of acrylates at 1410 $cm^{-1}$ was ~ 88% after a little less than 1 min of blue light irradiation. Conversely, after ~ 3 min of UV irradiation, ~ 26% of oxetanes at 985 $cm^{-1}$ were converted.

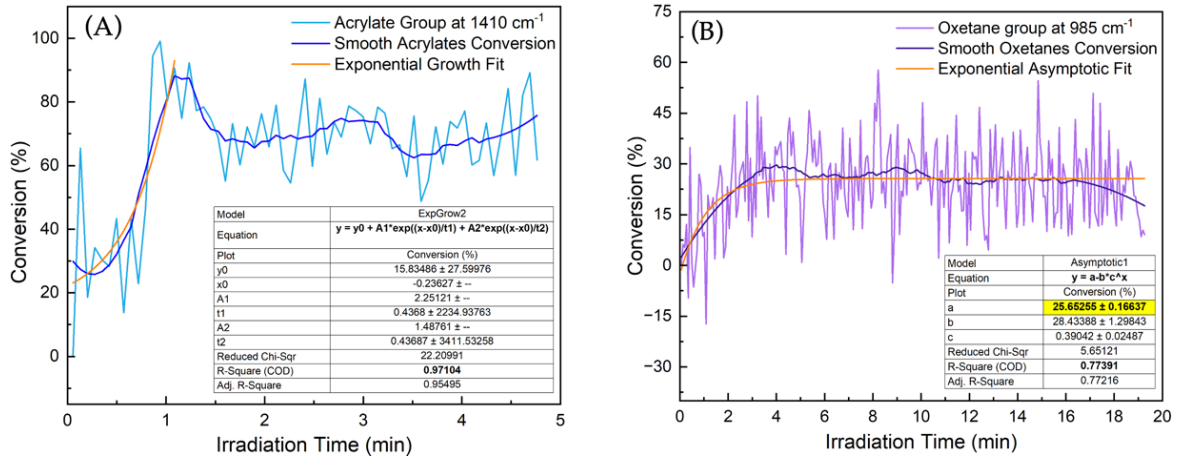


Figure A 18 – Conversion plots calculated from the intensity decrease over irradiation time determined through kinetics FTIR measurements: (A) acrylate group at 1410 $cm^{-1}$ wavenumber (~ 88% conversion after ~ 1min); (B) oxetane group at 985 $cm^{-1}$ wavenumber (~ 26% conversion after ~ 3min).

## A.9 Preliminary Thermal Actuation Tests

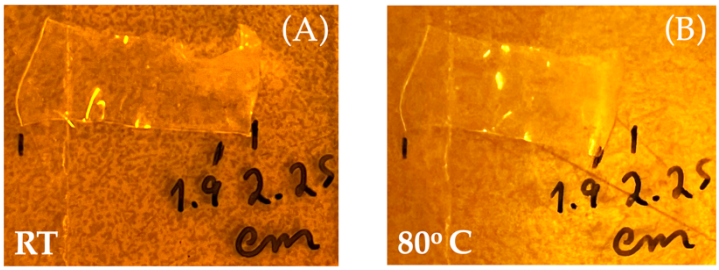


Figure A 19 - Actuation of the fully crosslinked *olgRM82-1* LCE film from a (A) 2.25 cm length at RT to (B) 1.9 cm at 80 °C.

## A.10 Type of Alignment: *olgRM82-2 vs C6BAPE-1*

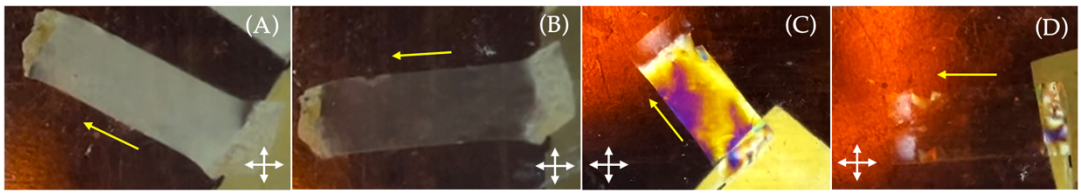


Figure A 20 - Observation between cross-polarisers on top of an LED of the: *olgRM82-2* film at (A) 45º (bright state) and (B) 0º (dark state) with polarisers; and *olgC6BAPE-1* film at a (C) 45º (bright state) and (D) 0º (dark state) with polarisers. Note the yellow arrow indicates the direction of stretching (n).

## A.11 XRD Measurements to Determine the S

The X-ray scattering pattern of an LC material allows for the qualitative and quantitative analysis of the mesophases present at a specific temperature. In this work, all XRD measurements were performed on the LCE films at RT.

First, observing the results shown in Figure A 21 and Figure A 22 from a qualitative lens, two outer vertically symmetric half circumferences can be seen in all the samples except the one containing a different LC mesogen from the rest, namely C6BAPE (Figure A 22 (A)). These half circumferences result from the scattering of the light due to the imperfect alignment of the molecules. The outer symmetric half circumferences are related to the order along the director, while the inner symmetric half circumferences emerge from the additional order orthogonal to the director, which is associated with a smectic phase. In the case of the *olgC6BAPE-1* sample, a full circumference is observed (Figure A 22 (A)), suggesting this film has already transitioned to its full disordered state, *i.e.*, an isotropic phase, at RT. It must be noted that the straight white horizontal lines present in all of the samples, where nothing was measured, come from the equipment itself and not the samples.

From the diffraction patterns it was possible to estimate the order parameters of the samples through the Lovell and Mitchell method detailed in the work of Mark T. Sims *et al.* [65]. For a more detailed explanation of this method for the *olgRM82-2* sample (Figure A 21 (A)), for instance. First, the intensity change as a function of the azimuthal angle variation was extracted from the X-ray scattering pattern. This plot, shown in Figure A 21 (B), possesses two regions where the intensity values decrease significantly, and these correspond to the white lines seen in Figure A 21 (A). Nevertheless, these error regions will not interfere with the estimation of the S, since only a quarter of a rotation (90º) is needed for the calculations. In the case of the *olgRM82-2* sample, the region chosen was from 90º to 182º. Note instead of the number of points corresponding to exactly a 90º rotation, one or two additional points must be taken for correct calculations. These values are then inserted in the equation shown below to determine the S.

$$S = -2 \cdot \frac{1}{2}\left( 3 \cdot \frac{\int_0^{\frac{\pi}{2}} I(\phi) \sin\phi \, (\cos\phi)^2 d\phi}{\int_0^{\frac{\pi}{2}} I(\phi) \sin\phi \, d\phi} - 1 \right)$$

Where S is the order parameter, $I$ is the intensity, and $\phi$ is the azimuthal angle.

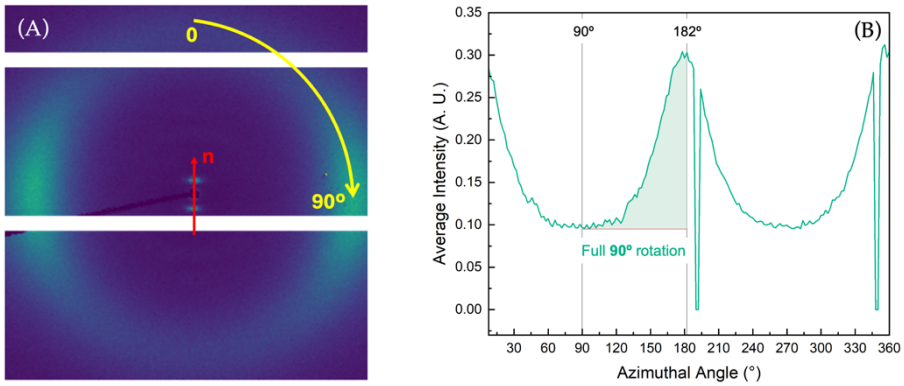


Figure A 21 – (A) X-ray scattering pattern of the *olgRM82-2* stretched sample at RT. (B) Azimuthal profiles of the XRD intensity extracted from the centre of the half circumferences are shown in (A).

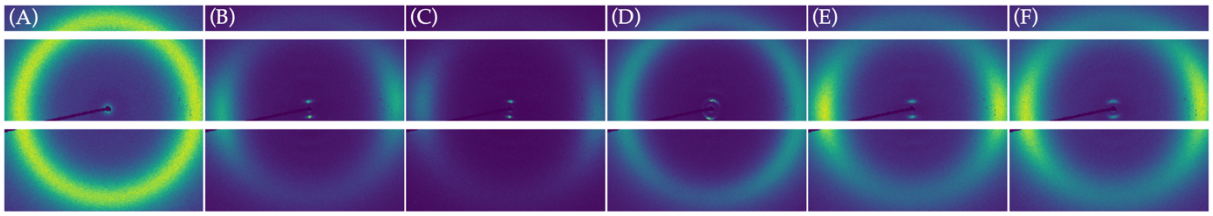


Figure A 22 - X-ray scattering patterns obtained from (A) *olgC6BAPE-1*, (B) *CC11.7wt%*, (C) *CC4.3wt%*, (D) *TAMAP*, (E) *4DP-1*, and (B) *4DP-2* stretched samples at RT.

## A.12 Thermodynamical Analysis: *olgC6BAPE-1 vs olgRM82-2*

The eventual presence of the smectic phase of the oligomer, shown in Figure A 17, after full polymerisation of the LCE films was investigated though DSC analysis. The measurement of partially crosslinked samples, *i.e.*, those that only underwent the first crosslinking stage, showed the absence of a smectic phase. These results are presented in Figure A 23.

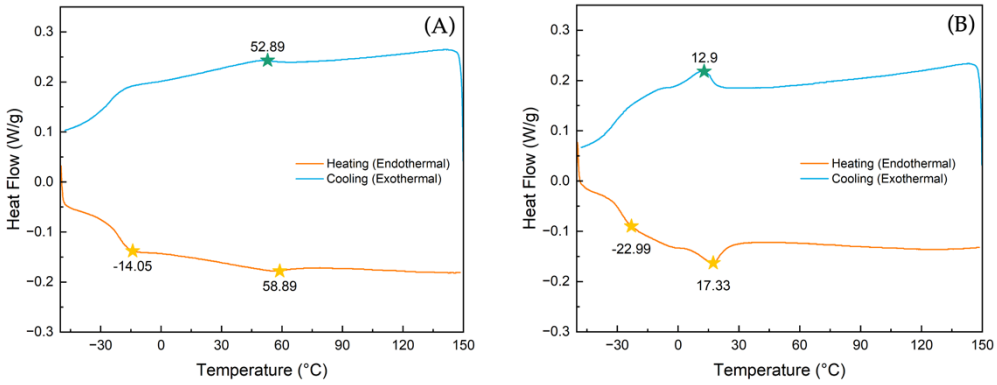


Figure A 23 - DSC Endo and Exo curves of (A) *olgRM82-2* and (B) *olgC6BAPE-1* partially crosslinked samples.

## A.13 Stamped *olgRM82-1* Sample: Azimuthal Alignment

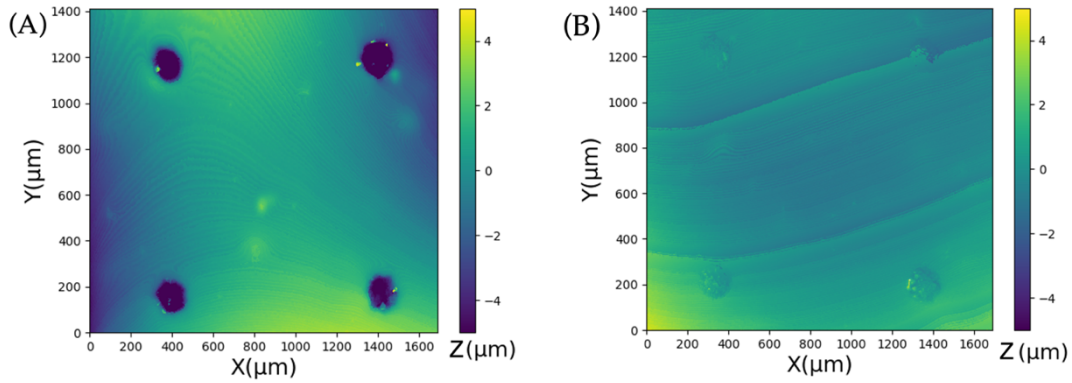


Figure A 24 – Interferometry (surface) measurements of the *olgRM82-1* sample stamped with a dots mould: (A) 2D surface image at RT (relaxed state) and (B) 2D surface image at 100 ºC (actuated state).

# A.14 Variation of Crosslinker's Concentration Trials

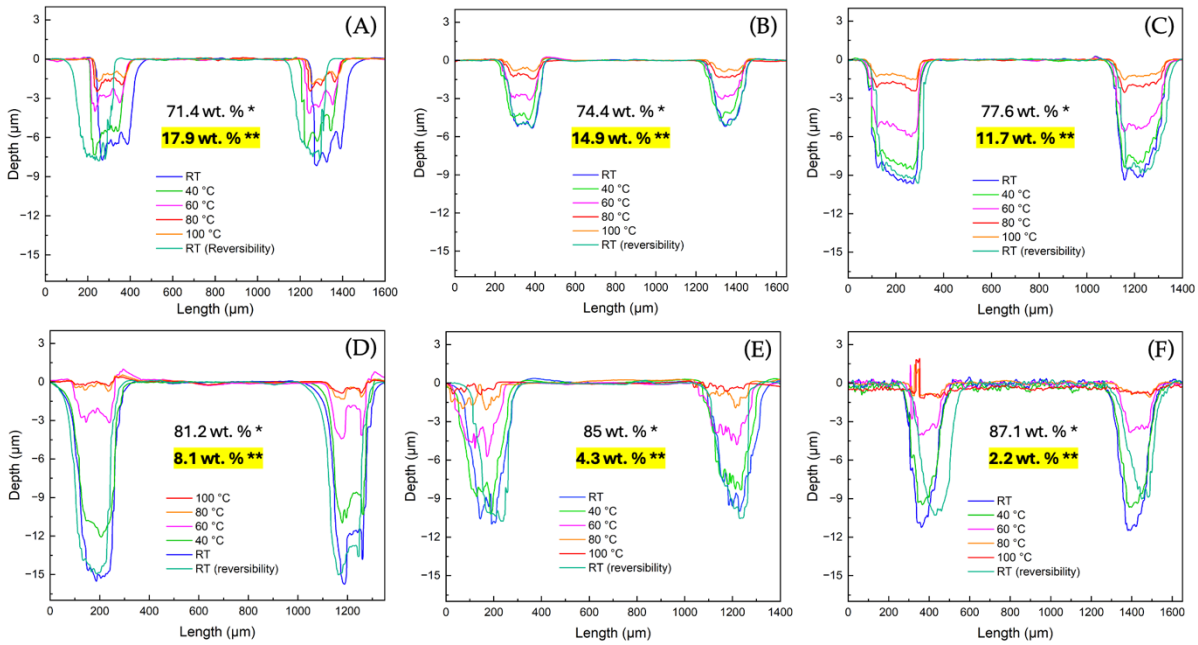


*Concentration of the oligomer (*i.e., olgRM82-1*) | **Concentration of the crosslinker | Concentrations of the initiators were kept the same in all samples

Figure A 25 - Depth *vs* length plots made from the interferometry data collected of dots samples containing different crosslinker concentrations, namely, (A) 17.9, (B) 14.9, (C) 11.7, (D) 8.1, (E) 4.3, or (F) 2.2 wt. % of crosslinker used relative to the weight of the oligomer (*i.e., olgRM82-1*). The film thicknesses were: (A) 66.27, (B) 56.83, (C) 67.58, (D) 54.89, (E) 47.78, and (F) 44.59 $\mu$m.

# A.15 Overtime Actuation Longevity Tests

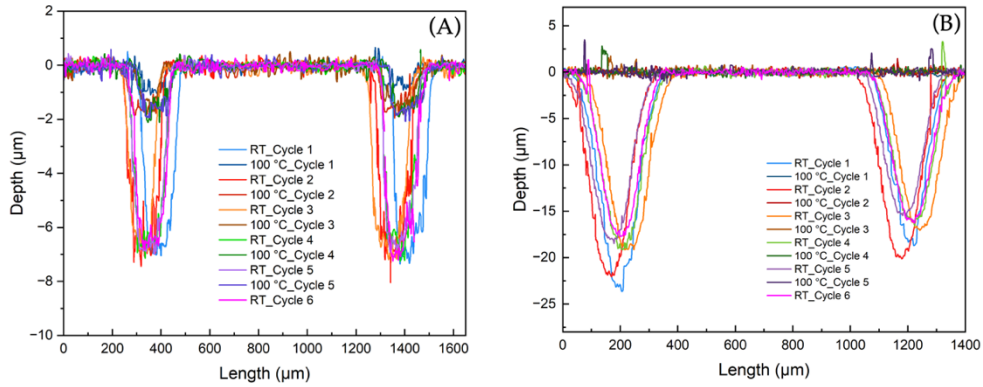


Figure A 26 – Depth *vs* length plots showing the overtime actuation longevity of the dots stamped films over multiplied cycles of heating and cooling: (A) *olgRM82-1* dots sample with 17.9 wt. % of crosslinker, and (B) *olgRM82-1* dots sample with no crosslinker.

# A.16 Crosslinker's Concentration Effect on Actuation

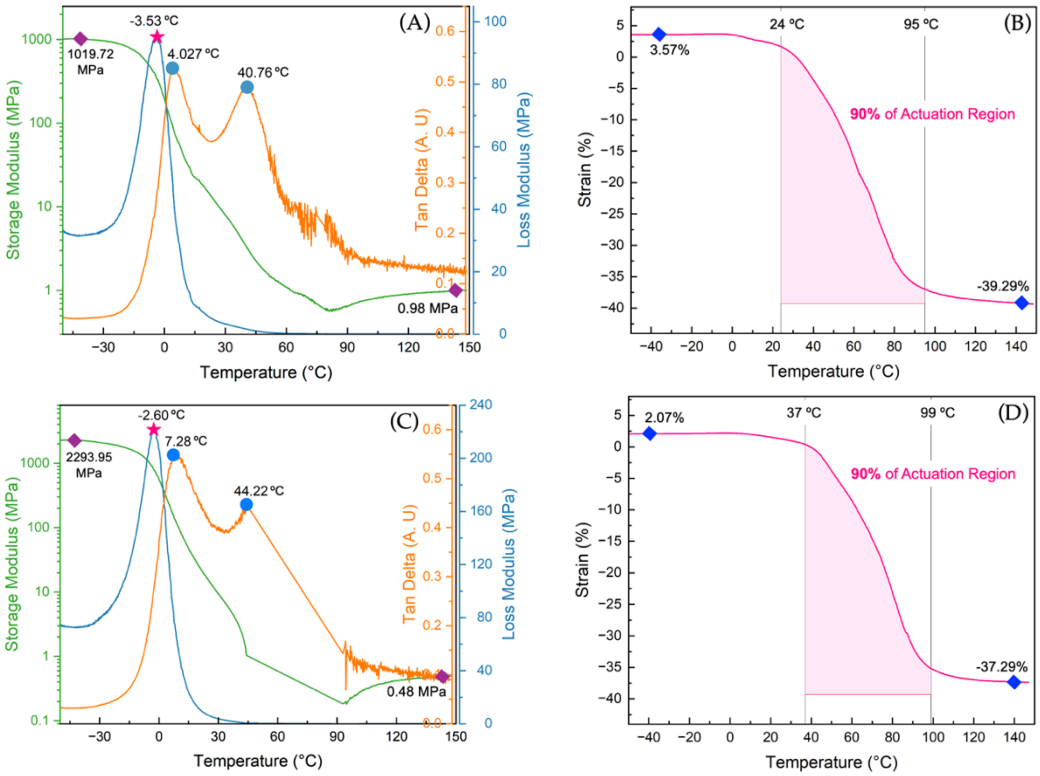


Figure A 27 - Characteristic DMA curves: Temperature Ramp/Frequency Sweep measurement of the (A) *CC11.7wt%* and (C) *CC4.3wt%* samples. Controlled Force/Temperature Ramp measurement of the (B) *CC11.7wt%* and (D) *CC4.3wt%* samples.

# A.17 One-pot Procedure

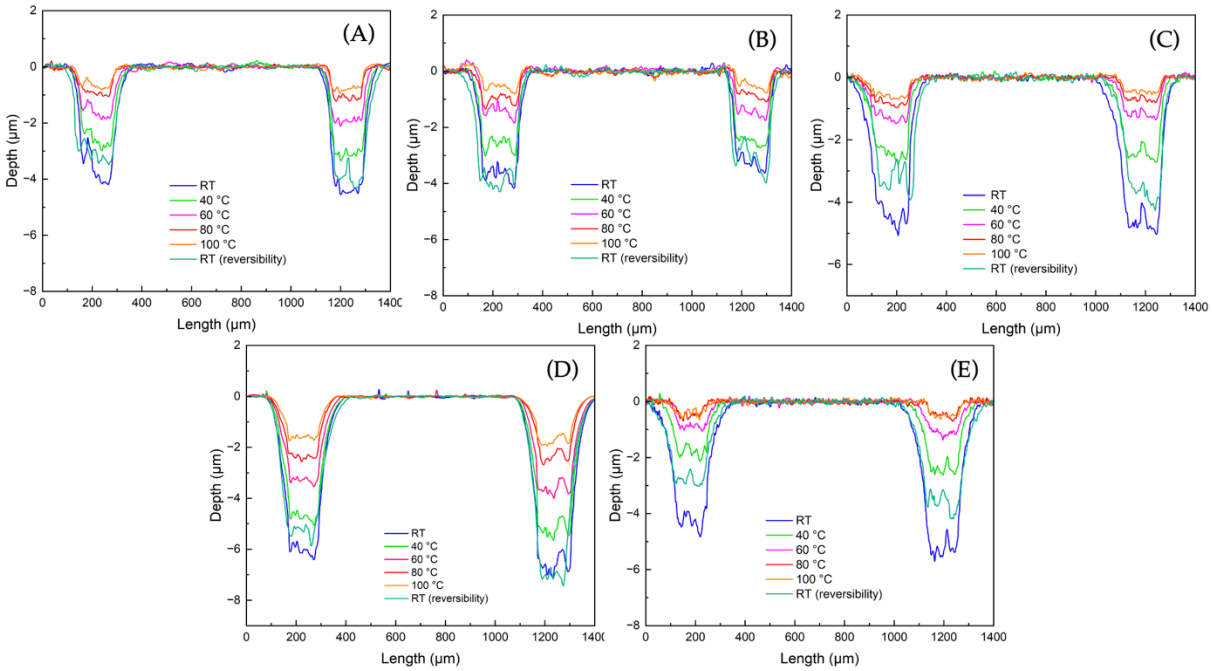


Figure A 28 - Depth *vs* length plots made from the interferometry data collected of dots samples prepared via one-pot TWSP. The ratios of RM82:DODT used, and film thicknesses were: (A) 1:0.9 and 51.37 $\mu$m; (B) 1:1 and 48.34 $\mu$m; (C) 0.9:1 and 51.30 $\mu$m; (D) 0.8:1 and 45.20 $\mu$m; (E) 0.7:1 and 39.05 $\mu$m, respectively.

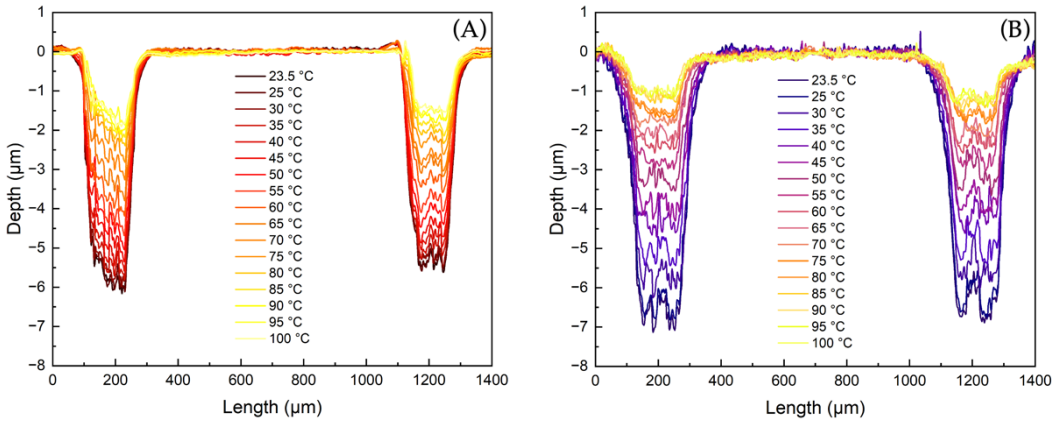


Figure A 29 – Depth *vs* Length plots over a temperature range from 23.5 to 100 °C, with 5 °C steps of (A) *olgRM82-2* dots sample and (B) one-pot ratio sample with 0.9:1 RM82:DODT ratio.

# A.18 TAMAP Method: Chemical Structure of the Components

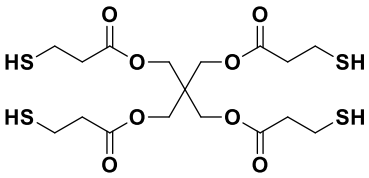


Figure A 30 - Chemical structure of the pentaerythritol crosslinker.

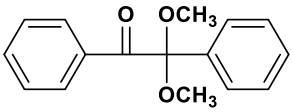


Figure A 31 - Chemical structure of the free-radical photo-initiator DMPA.

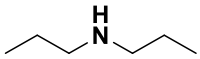

Figure A 32 - Chemical structure of the dipropylamine catalyst.

# A.19 DMA Characterisation of the *TAMAP* Sample

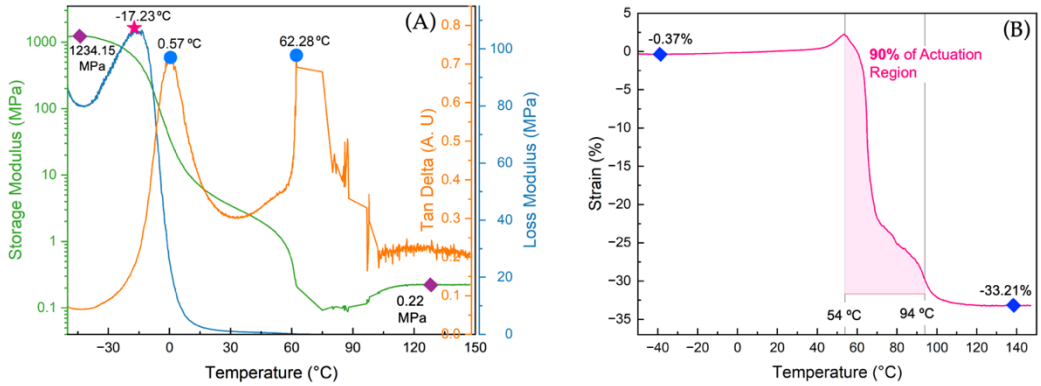


Figure A 33 - Characteristic DMA curves of the *TAMAP* sample: (A) Temperature Ramp/Frequency Sweep measurement and (B) Controlled Force/Temperature Ramp measurement.

# A.20 DMA Characterisation of 4D-Printed Samples

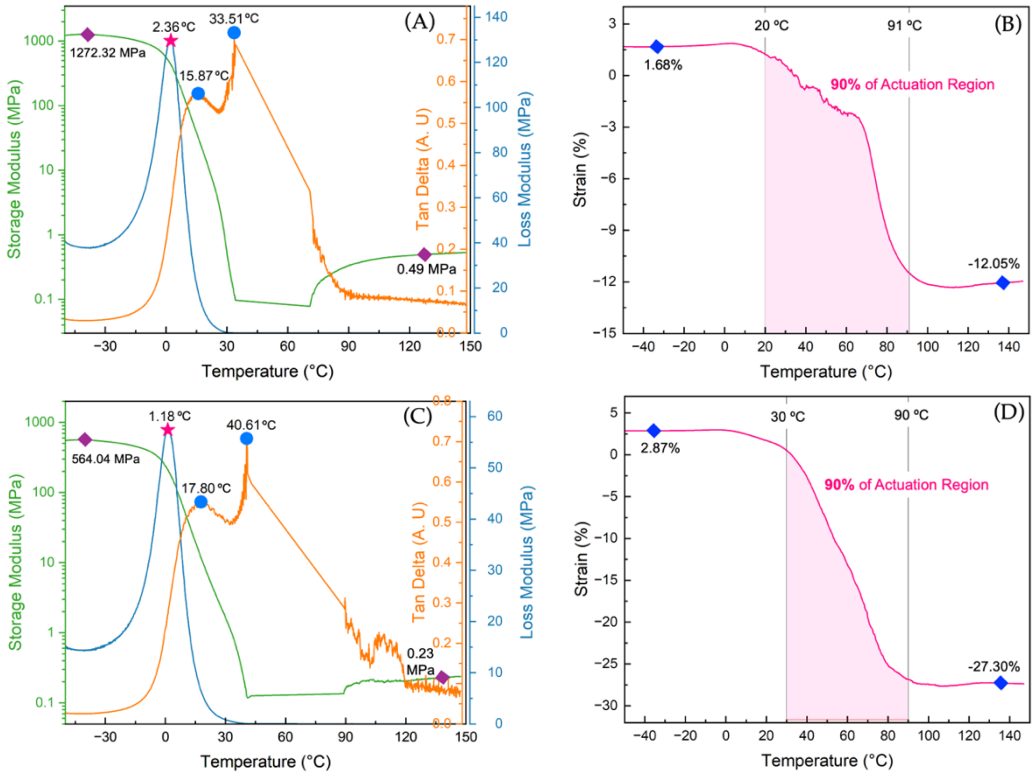


Figure A 34 - Characteristic DMA curves: Temperature Ramp/Frequency Sweep measurement of the (A) *4DP-1* and (C) *4DP-2* samples. Controlled Force/Temperature Ramp measurement of the (B) *4DP-1* and (D) *4DP-2* samples.

# A.21 Gcode Used for 4D Printing

```
; generated by PrusaSlicer 2.7.4+win64 on 2024-06-12 at 10:20:01 UTC
;
; external perimeters extrusion width = 0.45mm
; perimeters extrusion width = 0.45mm
; infill extrusion width = 0.45mm
; solid infill extrusion width = 0.45mm
; top infill extrusion width = 0.40mm
;TYPE:Custom
; \\\\\\\\\ START PRINTER HEADER /////////////
M140 S20
G28 Z0 ; home Z
G28 X0 Y0 ; home X/Y
; Uncomment for UV pen on slot 3 (from the left) to expose the extrusion on port 1
```

; To change the extrusion port here, change S11 to S1X, and to change the position of the UV pen, change T1X

;M620 T13 E1 ; Turn on the UV Pen

;M703 T13 S11 ; Duplicate commands between Head 4 and 1

;M621 T13 P100 ; Set light emission tied to extrusion moves with power PXXX

; \\\\\\\\ END PRINTER HEADER /////////

G21 ; set units to millimeters

G90 ; use absolute coordinates

M82 ; use absolute distances for extrusion

G92 E0

; \\\\\\\\ START EXTRUDER 1 HEADER /////////

T0

M109 S75 ; set temperature and wait for it to be reached

M190 S20 L5 U13 ; Wait for the temperature of the bed to be 25 +- 2??C

M6 T11 O1 X110 Y26 ; slot 1 (Input X,Y from tooloffset)

M660 H0 Z35.6098; Input Z from tooloffset

M229 E0 D0; Ignore the E values and keep the same extrusion as in M221 (pulse)

M221 P9000 S1.0 T11 Z0.03 W0.4; set flow (Pn: Nb of motor pulses (extrusion speed), S: the flow multiplier, Wn: Width of the track (Nozzle Diameter), Zn: layer thickness, Tn: the head)

G0 X0 Y0 ; goes to starting point X, Y

; Priming of extruder 1/4th with one rotation

;M722 S10000 E99999 P-15 I0 T11 ; takes 3.5 sec to complete ; Max value is 99999 and 10k

;G4 P3500 ; time available in ms to complete previous commands

;M722 S10000 E99999 P-15 I0 T11

;G4 P3500

;M722 S10000 E10000 P-15 I0 T11

G4 3000

; Turn off priming at the start of each layer and object

M721 S1 E1 P1 T11 ; no prime

M722 S1 E1 P1 T11 ; prime is ded

; \\\\\\\\ END EXTRUDER 1 HEADER /////////

M107

;LAYER_CHANGE

;Z:0.03

;HEIGHT:0.03

G1 E-2 F2400

G1 Z.03 F900

G92 E0

G1 X4.793 Y.337 F2700

G1 Z.03 F900

```
G1 E2 F2400
G92 E0
;TYPE:External perimeter
;WIDTH:0.406438
G1 F360
G1 X4.793 Y13.937 E.06785
G1 X4.776 Y14.02 E.06827
;WIDTH:0.475067
G1 X4.759 Y14.103 E.06877
G1 X4.593 Y14.137 E.06976
;WIDTH:0.40644
G1 X4.51 Y14.12 E.07018
;WIDTH:0.475066
G1 X4.427 Y14.103 E.07068
G1 X4.392 Y13.937 E.07167
;WIDTH:0.406438
G1 X4.392 Y4.737 E.11757
G1 X4.375 Y4.654 E.11799
;WIDTH:0.475066
G1 X4.358 Y4.571 E.11849
G1 X4.192 Y4.537 E.11948
;WIDTH:0.406438
G1 X4.109 Y4.554 E.1199
;WIDTH:0.475066
G1 X4.026 Y4.571 E.1204
G1 X3.991 Y4.737 E.12139
;WIDTH:0.406438
G1 X3.991 Y13.937 E.16729
G1 X3.974 Y14.02 E.16771
;WIDTH:0.475069
G1 X3.957 Y14.103 E.16821
G1 X3.886 Y14.126 E.16865
G1 X3.625 Y14.102 E.17018
G1 X3.591 Y13.937 E.17116
;WIDTH:0.407436
G1 X3.59 Y4.737 E.21717
G1 X3.573 Y4.654 E.21759
;WIDTH:0.475081
G1 X3.556 Y4.571 E.21809
G1 X3.39 Y4.537 E.21908
;WIDTH:0.406438
```

G1 X3.307 Y4.554 E.2195
;WIDTH:0.475066
G1 X3.224 Y4.571 E.22
G1 X3.189 Y4.737 E.22099
;WIDTH:0.406438
G1 X3.189 Y13.937 E.26689
G1 X3.172 Y14.02 E.26731
;WIDTH:0.475066
G1 X3.155 Y14.103 E.26781
G1 X2.989 Y14.137 E.2688
;WIDTH:0.40644
G1 X2.906 Y14.12 E.26922
;WIDTH:0.475083
G1 X2.823 Y14.103 E.26972
G1 X2.788 Y13.937 E.27071
;WIDTH:0.407438
G1 X2.788 Y4.737 E.31672
G1 X2.771 Y4.654 E.31714
;WIDTH:0.475652
G1 X2.754 Y4.572 E.31763
G1 X2.422 Y4.571 E.31957
G1 X2.387 Y4.737 E.32056
;WIDTH:0.407438
G1 X2.387 Y13.936 E.36657
G1 X2.37 Y14.019 E.36699
;WIDTH:0.476045
G1 X2.353 Y14.102 E.36749
G1 X2.021 Y14.103 E.36943
G1 X1.986 Y13.936 E.37043
;WIDTH:0.407438
G1 X1.986 Y4.737 E.41644
G1 X1.969 Y4.654 E.41686
;WIDTH:0.475652
G1 X1.952 Y4.572 E.41735
G1 X1.62 Y4.571 E.41929
G1 X1.585 Y4.737 E.42028
;WIDTH:0.407436
G1 X1.585 Y13.936 E.46629
G1 X1.568 Y14.019 E.46671
;WIDTH:0.476083
G1 X1.551 Y14.102 E.46721

```
G1 X1.219 Y14.103 E.46915
G1 X1.184 Y13.936 E.47015
;WIDTH:0.40644
G1 X1.184 Y4.737 E.51604
G1 X1.167 Y4.654 E.51646
;WIDTH:0.475066
G1 X1.15 Y4.571 E.51696
G1 X1.079 Y4.548 E.5174
G1 X.818 Y4.572 E.51893
G1 X.784 Y4.737 E.51991
;WIDTH:0.40748
G1 X.783 Y13.936 E.56592
G1 X.766 Y14.019 E.56634
;WIDTH:0.476059
G1 X.749 Y14.102 E.56684
G1 X.417 Y14.103 E.56878
G1 X.382 Y13.936 E.56978
;WIDTH:0.406438
G1 X.382 Y.337 E.63763
;LAYER_CHANGE
;Z:0.06
;HEIGHT:0.03
; ====================
G1 Z.06 F900
; ====================
G1 X.382 Y.337 Z.06 F2700
G1 X4.793 Y.337
G92 E0
G1 F360
G1 X4.793 Y13.937 E.06785
G1 X4.776 Y14.02 E.06827
;WIDTH:0.475067
G1 X4.759 Y14.103 E.06877
G1 X4.593 Y14.137 E.06976
;WIDTH:0.40644
G1 X4.51 Y14.12 E.07018
;WIDTH:0.475066
G1 X4.427 Y14.103 E.07068
G1 X4.392 Y13.937 E.07167
;WIDTH:0.406438
G1 X4.392 Y4.737 E.11757
```

G1 X4.375 Y4.654 E.11799
;WIDTH:0.475066
G1 X4.358 Y4.571 E.11849
G1 X4.192 Y4.537 E.11948
;WIDTH:0.406438
G1 X4.109 Y4.554 E.1199
;WIDTH:0.475066
G1 X4.026 Y4.571 E.1204
G1 X3.991 Y4.737 E.12139
;WIDTH:0.406438
G1 X3.991 Y13.937 E.16729
G1 X3.974 Y14.02 E.16771
;WIDTH:0.475069
G1 X3.957 Y14.103 E.16821
G1 X3.886 Y14.126 E.16865
G1 X3.625 Y14.102 E.17018
G1 X3.591 Y13.937 E.17116
;WIDTH:0.407436
G1 X3.59 Y4.737 E.21717
G1 X3.573 Y4.654 E.21759
;WIDTH:0.475081
G1 X3.556 Y4.571 E.21809
G1 X3.39 Y4.537 E.21908
;WIDTH:0.406438
G1 X3.307 Y4.554 E.2195
;WIDTH:0.475066
G1 X3.224 Y4.571 E.22
G1 X3.189 Y4.737 E.22099
;WIDTH:0.406438
G1 X3.189 Y13.937 E.26689
G1 X3.172 Y14.02 E.26731
;WIDTH:0.475066
G1 X3.155 Y14.103 E.26781
G1 X2.989 Y14.137 E.2688
;WIDTH:0.40644
G1 X2.906 Y14.12 E.26922
;WIDTH:0.475083
G1 X2.823 Y14.103 E.26972
G1 X2.788 Y13.937 E.27071
;WIDTH:0.407438
G1 X2.788 Y4.737 E.31672

G1 X2.771 Y4.654 E.31714
;WIDTH:0.475652
G1 X2.754 Y4.572 E.31763
G1 X2.422 Y4.571 E.31957
G1 X2.387 Y4.737 E.32056
;WIDTH:0.407438
G1 X2.387 Y13.936 E.36657
G1 X2.37 Y14.019 E.36699
;WIDTH:0.476045
G1 X2.353 Y14.102 E.36749
G1 X2.021 Y14.103 E.36943
G1 X1.986 Y13.936 E.37043
;WIDTH:0.407438
G1 X1.986 Y4.737 E.41644
G1 X1.969 Y4.654 E.41686
;WIDTH:0.475652
G1 X1.952 Y4.572 E.41735
G1 X1.62 Y4.571 E.41929
G1 X1.585 Y4.737 E.42028
;WIDTH:0.407436
G1 X1.585 Y13.936 E.46629
G1 X1.568 Y14.019 E.46671
;WIDTH:0.476083
G1 X1.551 Y14.102 E.46721
G1 X1.219 Y14.103 E.46915
G1 X1.184 Y13.936 E.47015
;WIDTH:0.40644
G1 X1.184 Y4.737 E.51604
G1 X1.167 Y4.654 E.51646
;WIDTH:0.475066
G1 X1.15 Y4.571 E.51696
G1 X1.079 Y4.548 E.5174
G1 X.818 Y4.572 E.51893
G1 X.784 Y4.737 E.51991
;WIDTH:0.40748
G1 X.783 Y13.936 E.56592
G1 X.766 Y14.019 E.56634
;WIDTH:0.476059
G1 X.749 Y14.102 E.56684
G1 X.417 Y14.103 E.56878
G1 X.382 Y13.936 E.56978

```
;WIDTH:0.406438
G1 X.382 Y.337 E.63763
;LAYER_CHANGE
;Z:0.09
;HEIGHT:0.03
; ====================
G1 Z.09 F900
; ====================
G1 X.382 Y.337 Z.09 F2700
G1 X4.793 Y.337
G92 E0
G1 F360
G1 X4.793 Y13.937 E.06785
G1 X4.776 Y14.02 E.06827
;WIDTH:0.475067
G1 X4.759 Y14.103 E.06877
G1 X4.593 Y14.137 E.06976
;WIDTH:0.40644
G1 X4.51 Y14.12 E.07018
;WIDTH:0.475066
G1 X4.427 Y14.103 E.07068
G1 X4.392 Y13.937 E.07167
;WIDTH:0.406438
G1 X4.392 Y4.737 E.11757
G1 X4.375 Y4.654 E.11799
;WIDTH:0.475066
G1 X4.358 Y4.571 E.11849
G1 X4.192 Y4.537 E.11948
;WIDTH:0.406438
G1 X4.109 Y4.554 E.1199
;WIDTH:0.475066
G1 X4.026 Y4.571 E.1204
G1 X3.991 Y4.737 E.12139
;WIDTH:0.406438
G1 X3.991 Y13.937 E.16729
G1 X3.974 Y14.02 E.16771
;WIDTH:0.475069
G1 X3.957 Y14.103 E.16821
G1 X3.886 Y14.126 E.16865
G1 X3.625 Y14.102 E.17018
G1 X3.591 Y13.937 E.17116
```

;WIDTH:0.407436
G1 X3.59 Y4.737 E.21717
G1 X3.573 Y4.654 E.21759
;WIDTH:0.475081
G1 X3.556 Y4.571 E.21809
G1 X3.39 Y4.537 E.21908
;WIDTH:0.406438
G1 X3.307 Y4.554 E.2195
;WIDTH:0.475066
G1 X3.224 Y4.571 E.22
G1 X3.189 Y4.737 E.22099
;WIDTH:0.406438
G1 X3.189 Y13.937 E.26689
G1 X3.172 Y14.02 E.26731
;WIDTH:0.475066
G1 X3.155 Y14.103 E.26781
G1 X2.989 Y14.137 E.2688
;WIDTH:0.40644
G1 X2.906 Y14.12 E.26922
;WIDTH:0.475083
G1 X2.823 Y14.103 E.26972
G1 X2.788 Y13.937 E.27071
;WIDTH:0.407438
G1 X2.788 Y4.737 E.31672
G1 X2.771 Y4.654 E.31714
;WIDTH:0.475652
G1 X2.754 Y4.572 E.31763
G1 X2.422 Y4.571 E.31957
G1 X2.387 Y4.737 E.32056
;WIDTH:0.407438
G1 X2.387 Y13.936 E.36657
G1 X2.37 Y14.019 E.36699
;WIDTH:0.476045
G1 X2.353 Y14.102 E.36749
G1 X2.021 Y14.103 E.36943
G1 X1.986 Y13.936 E.37043
;WIDTH:0.407438
G1 X1.986 Y4.737 E.41644
G1 X1.969 Y4.654 E.41686
;WIDTH:0.475652
G1 X1.952 Y4.572 E.41735

```
G1 X1.62 Y4.571 E.41929
G1 X1.585 Y4.737 E.42028
;WIDTH:0.407436
G1 X1.585 Y13.936 E.46629
G1 X1.568 Y14.019 E.46671
;WIDTH:0.476083
G1 X1.551 Y14.102 E.46721
G1 X1.219 Y14.103 E.46915
G1 X1.184 Y13.936 E.47015
;WIDTH:0.40644
G1 X1.184 Y4.737 E.51604
G1 X1.167 Y4.654 E.51646
;WIDTH:0.475066
G1 X1.15 Y4.571 E.51696
G1 X1.079 Y4.548 E.5174
G1 X.818 Y4.572 E.51893
G1 X.784 Y4.737 E.51991
;WIDTH:0.40748
G1 X.783 Y13.936 E.56592
G1 X.766 Y14.019 E.56634
;WIDTH:0.476059
G1 X.749 Y14.102 E.56684
G1 X.417 Y14.103 E.56878
G1 X.382 Y13.936 E.56978
;WIDTH:0.406438
G1 X.382 Y.337 E.63763
;LAYER_CHANGE
;Z:0.12
;HEIGHT:0.03
; ====================
G1 Z.12 F900
; ====================
G1 X.382 Y.337 Z.12 F2700
G1 X4.793 Y.337
G92 E0
G1 F360
G1 X4.793 Y13.937 E.06785
G1 X4.776 Y14.02 E.06827
;WIDTH:0.475067
G1 X4.759 Y14.103 E.06877
G1 X4.593 Y14.137 E.06976
```

;WIDTH:0.40644
G1 X4.51 Y14.12 E.07018
;WIDTH:0.475066
G1 X4.427 Y14.103 E.07068
G1 X4.392 Y13.937 E.07167
;WIDTH:0.406438
G1 X4.392 Y4.737 E.11757
G1 X4.375 Y4.654 E.11799
;WIDTH:0.475066
G1 X4.358 Y4.571 E.11849
G1 X4.192 Y4.537 E.11948
;WIDTH:0.406438
G1 X4.109 Y4.554 E.1199
;WIDTH:0.475066
G1 X4.026 Y4.571 E.1204
G1 X3.991 Y4.737 E.12139
;WIDTH:0.406438
G1 X3.991 Y13.937 E.16729
G1 X3.974 Y14.02 E.16771
;WIDTH:0.475069
G1 X3.957 Y14.103 E.16821
G1 X3.886 Y14.126 E.16865
G1 X3.625 Y14.102 E.17018
G1 X3.591 Y13.937 E.17116
;WIDTH:0.407436
G1 X3.59 Y4.737 E.21717
G1 X3.573 Y4.654 E.21759
;WIDTH:0.475081
G1 X3.556 Y4.571 E.21809
G1 X3.39 Y4.537 E.21908
;WIDTH:0.406438
G1 X3.307 Y4.554 E.2195
;WIDTH:0.475066
G1 X3.224 Y4.571 E.22
G1 X3.189 Y4.737 E.22099
;WIDTH:0.406438
G1 X3.189 Y13.937 E.26689
G1 X3.172 Y14.02 E.26731
;WIDTH:0.475066
G1 X3.155 Y14.103 E.26781
G1 X2.989 Y14.137 E.2688

;WIDTH:0.40644
G1 X2.906 Y14.12 E.26922
;WIDTH:0.475083
G1 X2.823 Y14.103 E.26972
G1 X2.788 Y13.937 E.27071
;WIDTH:0.407438
G1 X2.788 Y4.737 E.31672
G1 X2.771 Y4.654 E.31714
;WIDTH:0.475652
G1 X2.754 Y4.572 E.31763
G1 X2.422 Y4.571 E.31957
G1 X2.387 Y4.737 E.32056
;WIDTH:0.407438
G1 X2.387 Y13.936 E.36657
G1 X2.37 Y14.019 E.36699
;WIDTH:0.476045
G1 X2.353 Y14.102 E.36749
G1 X2.021 Y14.103 E.36943
G1 X1.986 Y13.936 E.37043
;WIDTH:0.407438
G1 X1.986 Y4.737 E.41644
G1 X1.969 Y4.654 E.41686
;WIDTH:0.475652
G1 X1.952 Y4.572 E.41735
G1 X1.62 Y4.571 E.41929
G1 X1.585 Y4.737 E.42028
;WIDTH:0.407436
G1 X1.585 Y13.936 E.46629
G1 X1.568 Y14.019 E.46671
;WIDTH:0.476083
G1 X1.551 Y14.102 E.46721
G1 X1.219 Y14.103 E.46915
G1 X1.184 Y13.936 E.47015
;WIDTH:0.40644
G1 X1.184 Y4.737 E.51604
G1 X1.167 Y4.654 E.51646
;WIDTH:0.475066
G1 X1.15 Y4.571 E.51696
G1 X1.079 Y4.548 E.5174
G1 X.818 Y4.572 E.51893
G1 X.784 Y4.737 E.51991

```
;WIDTH:0.40748
G1 X.783 Y13.936 E.56592
G1 X.766 Y14.019 E.56634
;WIDTH:0.476059
G1 X.749 Y14.102 E.56684
G1 X.417 Y14.103 E.56878
G1 X.382 Y13.936 E.56978
;WIDTH:0.406438
G1 X.382 Y.337 E.63763
;LAYER_CHANGE
;Z:0.15
;HEIGHT:0.03
; ====================
G1 Z.15 F900
; ====================
G1 X.382 Y.337 Z.15 F2700
G1 X4.793 Y.337
G92 E0
G1 F360
G1 X4.793 Y13.937 E.06785
G1 X4.776 Y14.02 E.06827
;WIDTH:0.475067
G1 X4.759 Y14.103 E.06877
G1 X4.593 Y14.137 E.06976
;WIDTH:0.40644
G1 X4.51 Y14.12 E.07018
;WIDTH:0.475066
G1 X4.427 Y14.103 E.07068
G1 X4.392 Y13.937 E.07167
;WIDTH:0.406438
G1 X4.392 Y4.737 E.11757
G1 X4.375 Y4.654 E.11799
;WIDTH:0.475066
G1 X4.358 Y4.571 E.11849
G1 X4.192 Y4.537 E.11948
;WIDTH:0.406438
G1 X4.109 Y4.554 E.1199
;WIDTH:0.475066
G1 X4.026 Y4.571 E.1204
G1 X3.991 Y4.737 E.12139
;WIDTH:0.406438
```

G1 X3.991 Y13.937 E.16729
G1 X3.974 Y14.02 E.16771
;WIDTH:0.475069
G1 X3.957 Y14.103 E.16821
G1 X3.886 Y14.126 E.16865
G1 X3.625 Y14.102 E.17018
G1 X3.591 Y13.937 E.17116
;WIDTH:0.407436
G1 X3.59 Y4.737 E.21717
G1 X3.573 Y4.654 E.21759
;WIDTH:0.475081
G1 X3.556 Y4.571 E.21809
G1 X3.39 Y4.537 E.21908
;WIDTH:0.406438
G1 X3.307 Y4.554 E.2195
;WIDTH:0.475066
G1 X3.224 Y4.571 E.22
G1 X3.189 Y4.737 E.22099
;WIDTH:0.406438
G1 X3.189 Y13.937 E.26689
G1 X3.172 Y14.02 E.26731
;WIDTH:0.475066
G1 X3.155 Y14.103 E.26781
G1 X2.989 Y14.137 E.2688
;WIDTH:0.40644
G1 X2.906 Y14.12 E.26922
;WIDTH:0.475083
G1 X2.823 Y14.103 E.26972
G1 X2.788 Y13.937 E.27071
;WIDTH:0.407438
G1 X2.788 Y4.737 E.31672
G1 X2.771 Y4.654 E.31714
;WIDTH:0.475652
G1 X2.754 Y4.572 E.31763
G1 X2.422 Y4.571 E.31957
G1 X2.387 Y4.737 E.32056
;WIDTH:0.407438
G1 X2.387 Y13.936 E.36657
G1 X2.37 Y14.019 E.36699
;WIDTH:0.476045
G1 X2.353 Y14.102 E.36749

G1 X2.021 Y14.103 E.36943
G1 X1.986 Y13.936 E.37043
;WIDTH:0.407438
G1 X1.986 Y4.737 E.41644
G1 X1.969 Y4.654 E.41686
;WIDTH:0.475652
G1 X1.952 Y4.572 E.41735
G1 X1.62 Y4.571 E.41929
G1 X1.585 Y4.737 E.42028
;WIDTH:0.407436
G1 X1.585 Y13.936 E.46629
G1 X1.568 Y14.019 E.46671
;WIDTH:0.476083
G1 X1.551 Y14.102 E.46721
G1 X1.219 Y14.103 E.46915
G1 X1.184 Y13.936 E.47015
;WIDTH:0.40644
G1 X1.184 Y4.737 E.51604
G1 X1.167 Y4.654 E.51646
;WIDTH:0.475066
G1 X1.15 Y4.571 E.51696
G1 X1.079 Y4.548 E.5174
G1 X.818 Y4.572 E.51893
G1 X.784 Y4.737 E.51991
;WIDTH:0.40748
G1 X.783 Y13.936 E.56592
G1 X.766 Y14.019 E.56634
;WIDTH:0.476059
G1 X.749 Y14.102 E.56684
G1 X.417 Y14.103 E.56878
G1 X.382 Y13.936 E.56978
;WIDTH:0.406438
G1 X.382 Y.337 E.63763
;LAYER_CHANGE
;Z:0.18
;HEIGHT:0.03
; ====================
G1 Z.18 F900
; ====================
G1 X.382 Y.337 Z.18 F2700
G1 X4.793 Y.337

```
G92 E0
G1 F360
G1 X4.793 Y13.937 E.06785
G1 X4.776 Y14.02 E.06827
;WIDTH:0.475067
G1 X4.759 Y14.103 E.06877
G1 X4.593 Y14.137 E.06976
;WIDTH:0.40644
G1 X4.51 Y14.12 E.07018
;WIDTH:0.475066
G1 X4.427 Y14.103 E.07068
G1 X4.392 Y13.937 E.07167
;WIDTH:0.406438
G1 X4.392 Y4.737 E.11757
G1 X4.375 Y4.654 E.11799
;WIDTH:0.475066
G1 X4.358 Y4.571 E.11849
G1 X4.192 Y4.537 E.11948
;WIDTH:0.406438
G1 X4.109 Y4.554 E.1199
;WIDTH:0.475066
G1 X4.026 Y4.571 E.1204
G1 X3.991 Y4.737 E.12139
;WIDTH:0.406438
G1 X3.991 Y13.937 E.16729
G1 X3.974 Y14.02 E.16771
;WIDTH:0.475069
G1 X3.957 Y14.103 E.16821
G1 X3.886 Y14.126 E.16865
G1 X3.625 Y14.102 E.17018
G1 X3.591 Y13.937 E.17116
;WIDTH:0.407436
G1 X3.59 Y4.737 E.21717
G1 X3.573 Y4.654 E.21759
;WIDTH:0.475081
G1 X3.556 Y4.571 E.21809
G1 X3.39 Y4.537 E.21908
;WIDTH:0.406438
G1 X3.307 Y4.554 E.2195
;WIDTH:0.475066
G1 X3.224 Y4.571 E.22
```

G1 X3.189 Y4.737 E.22099
;WIDTH:0.406438
G1 X3.189 Y13.937 E.26689
G1 X3.172 Y14.02 E.26731
;WIDTH:0.475066
G1 X3.155 Y14.103 E.26781
G1 X2.989 Y14.137 E.2688
;WIDTH:0.40644
G1 X2.906 Y14.12 E.26922
;WIDTH:0.475083
G1 X2.823 Y14.103 E.26972
G1 X2.788 Y13.937 E.27071
;WIDTH:0.407438
G1 X2.788 Y4.737 E.31672
G1 X2.771 Y4.654 E.31714
;WIDTH:0.475652
G1 X2.754 Y4.572 E.31763
G1 X2.422 Y4.571 E.31957
G1 X2.387 Y4.737 E.32056
;WIDTH:0.407438
G1 X2.387 Y13.936 E.36657
G1 X2.37 Y14.019 E.36699
;WIDTH:0.476045
G1 X2.353 Y14.102 E.36749
G1 X2.021 Y14.103 E.36943
G1 X1.986 Y13.936 E.37043
;WIDTH:0.407438
G1 X1.986 Y4.737 E.41644
G1 X1.969 Y4.654 E.41686
;WIDTH:0.475652
G1 X1.952 Y4.572 E.41735
G1 X1.62 Y4.571 E.41929
G1 X1.585 Y4.737 E.42028
;WIDTH:0.407436
G1 X1.585 Y13.936 E.46629
G1 X1.568 Y14.019 E.46671
;WIDTH:0.476083
G1 X1.551 Y14.102 E.46721
G1 X1.219 Y14.103 E.46915
G1 X1.184 Y13.936 E.47015
;WIDTH:0.40644

```
G1 X1.184 Y4.737 E.51604
G1 X1.167 Y4.654 E.51646
;WIDTH:0.475066
G1 X1.15 Y4.571 E.51696
G1 X1.079 Y4.548 E.5174
G1 X.818 Y4.572 E.51893
G1 X.784 Y4.737 E.51991
;WIDTH:0.40748
G1 X.783 Y13.936 E.56592
G1 X.766 Y14.019 E.56634
;WIDTH:0.476059
G1 X.749 Y14.102 E.56684
G1 X.417 Y14.103 E.56878
G1 X.382 Y13.936 E.56978
;WIDTH:0.406438
G1 X.382 Y.337 E.63763
;LAYER_CHANGE
;Z:0.21
;HEIGHT:0.03
; ====================
G1 Z.21 F900
; ====================
G1 X.382 Y.337 Z.21 F2700
G1 X4.793 Y.337
G92 E0
G1 F360
G1 X4.793 Y13.937 E.06785
G1 X4.776 Y14.02 E.06827
;WIDTH:0.475067
G1 X4.759 Y14.103 E.06877
G1 X4.593 Y14.137 E.06976
;WIDTH:0.40644
G1 X4.51 Y14.12 E.07018
;WIDTH:0.475066
G1 X4.427 Y14.103 E.07068
G1 X4.392 Y13.937 E.07167
;WIDTH:0.406438
G1 X4.392 Y4.737 E.11757
G1 X4.375 Y4.654 E.11799
;WIDTH:0.475066
G1 X4.358 Y4.571 E.11849
```

G1 X4.192 Y4.537 E.11948
;WIDTH:0.406438
G1 X4.109 Y4.554 E.1199
;WIDTH:0.475066
G1 X4.026 Y4.571 E.1204
G1 X3.991 Y4.737 E.12139
;WIDTH:0.406438
G1 X3.991 Y13.937 E.16729
G1 X3.974 Y14.02 E.16771
;WIDTH:0.475069
G1 X3.957 Y14.103 E.16821
G1 X3.886 Y14.126 E.16865
G1 X3.625 Y14.102 E.17018
G1 X3.591 Y13.937 E.17116
;WIDTH:0.407436
G1 X3.59 Y4.737 E.21717
G1 X3.573 Y4.654 E.21759
;WIDTH:0.475081
G1 X3.556 Y4.571 E.21809
G1 X3.39 Y4.537 E.21908
;WIDTH:0.406438
G1 X3.307 Y4.554 E.2195
;WIDTH:0.475066
G1 X3.224 Y4.571 E.22
G1 X3.189 Y4.737 E.22099
;WIDTH:0.406438
G1 X3.189 Y13.937 E.26689
G1 X3.172 Y14.02 E.26731
;WIDTH:0.475066
G1 X3.155 Y14.103 E.26781
G1 X2.989 Y14.137 E.2688
;WIDTH:0.40644
G1 X2.906 Y14.12 E.26922
;WIDTH:0.475083
G1 X2.823 Y14.103 E.26972
G1 X2.788 Y13.937 E.27071
;WIDTH:0.407438
G1 X2.788 Y4.737 E.31672
G1 X2.771 Y4.654 E.31714
;WIDTH:0.475652
G1 X2.754 Y4.572 E.31763

G1 X2.422 Y4.571 E.31957
G1 X2.387 Y4.737 E.32056
;WIDTH:0.407438
G1 X2.387 Y13.936 E.36657
G1 X2.37 Y14.019 E.36699
;WIDTH:0.476045
G1 X2.353 Y14.102 E.36749
G1 X2.021 Y14.103 E.36943
G1 X1.986 Y13.936 E.37043
;WIDTH:0.407438
G1 X1.986 Y4.737 E.41644
G1 X1.969 Y4.654 E.41686
;WIDTH:0.475652
G1 X1.952 Y4.572 E.41735
G1 X1.62 Y4.571 E.41929
G1 X1.585 Y4.737 E.42028
;WIDTH:0.407436
G1 X1.585 Y13.936 E.46629
G1 X1.568 Y14.019 E.46671
;WIDTH:0.476083
G1 X1.551 Y14.102 E.46721
G1 X1.219 Y14.103 E.46915
G1 X1.184 Y13.936 E.47015
;WIDTH:0.40644
G1 X1.184 Y4.737 E.51604
G1 X1.167 Y4.654 E.51646
;WIDTH:0.475066
G1 X1.15 Y4.571 E.51696
G1 X1.079 Y4.548 E.5174
G1 X.818 Y4.572 E.51893
G1 X.784 Y4.737 E.51991
;WIDTH:0.40748
G1 X.783 Y13.936 E.56592
G1 X.766 Y14.019 E.56634
;WIDTH:0.476059
G1 X.749 Y14.102 E.56684
G1 X.417 Y14.103 E.56878
G1 X.382 Y13.936 E.56978
;WIDTH:0.406438
G1 X.382 Y.337 E.63763
G1 E-1.36237 F2400

```
G92 E0
M107
;TYPE:Custom
; \\\\\\\\ START EXTRUDER 1 FOOTER/ / / / / / / / /
;M721 S10000 E99999 P-15 I0 T11 ; takes 3.5 sec to complete ; Max value is 99999 and 10k
;G4 P3500 ; time available in ms to complete previous commands
;M721 S10000 E99999 P-15 I0 T11
;G4 P3500
;M721 S10000 E10000 P-15 I0 T11
;G4 P800
M104 75
; \\\\\\\\ END EXTRUDER 1 FOOTER/ / / / / / / / /
; \\\\\\\\ START EXTRUDER 1 FOOTER/ / / / / / / / /
;M721 S10000 E99999 P-15 I0 T11 ; takes 3.5 sec to complete ; Max value is 99999 and 10k
;G4 P3500 ; time available in ms to complete previous commands
;M721 S10000 E99999 P-15 I0 T11
;G4 P3500
;M721 S10000 E10000 P-15 I0 T11
;G4 P800
M104 75
; \\\\\\\\ END EXTRUDER 1 FOOTER/ / / / / / / / /
; \\\\\\\\ START EXTRUDER 1 FOOTER/ / / / / / / / /
;M721 S10000 E99999 P-15 I0 T11 ; takes 3.5 sec to complete ; Max value is 99999 and 10k
;G4 P3500 ; time available in ms to complete previous commands
;M721 S10000 E99999 P-15 I0 T11
;G4 P3500
;M721 S10000 E10000 P-15 I0 T11
;G4 P800
M104 75
; \\\\\\\\ END EXTRUDER 1 FOOTER/ / / / / / / / /
; \\\\\\\\ START PRINTER FOOT/ / / / / / / / /
M104 S0 ; turn off temperature
G0 Z100
G28 X0  ; home X axis
G28 Y0  ; home Z axis
M84     ; disable motors
G53 ; clear offsets
M30 ; end
; \\\\\\\\ END PRINTER FOOT/ / / / / / / / /
; objects_info = {"objects":[]}
; filament used [mm] = 4.46, 0.00, 0.00
```

; filament used [cm3] = 0.01, 0.00, 0.00
; total filament used [g] = 0.00
; total filament cost = 0.00
; total filament used for wipe tower [g] = 0.00
; estimated printing time (normal mode) = 2m 37s
; estimated first layer printing time (normal mode) = 21s
; prusaslicer_config = begin
; arc_fitting = disabled
; autoemit_temperature_commands = 0
; avoid_crossing_curled_overhangs = 0
; avoid_crossing_perimeters = 1
; avoid_crossing_perimeters_max_detour = 10
; bed_custom_model =
; bed_custom_texture =
; bed_shape = -32.5x-25,42.5x-25,42.5x25,-32.5x25
; bed_temperature = 20,20,20
; before_layer_gcode = ; ====================
; between_objects_gcode =
; binary_gcode = 0
; bottom_fill_pattern = monotonic
; bottom_solid_layers = 3
; bottom_solid_min_thickness = 0
; bridge_acceleration = 0
; bridge_angle = 0
; bridge_fan_speed = 100,100,100
; bridge_flow_ratio = 1
; bridge_speed = 60
; brim_separation = 0.4
; brim_type = outer_only
; brim_width = 0
; color_change_gcode =
; complete_objects = 0
; cooling = 0,0,0
; cooling_tube_length = 5
; cooling_tube_retraction = 91.5
; default_acceleration = 0
; default_filament_profile =
; default_print_profile =
; deretract_speed = 0,0,0
; disable_fan_first_layers = 3,3,3
; dont_support_bridges = 1

; draft_shield = disabled

; duplicate_distance = 6

; elefant_foot_compensation = 0

; enable_dynamic_fan_speeds = 0,0,0

; enable_dynamic_overhang_speeds = 0

; end_filament_gcode = "; \\\\\\\\\\\\\\\\ START EXTRUDER 1 FOOTER/////////\n\n;M721 S10000 E99999 P-15 I0 T11 ; takes 3.5 sec to complete ; Max value is 99999 and 10k\n;G4 P3500 ; time available in ms to complete previous commands\n;M721 S10000 E99999 P-15 I0 T11\n;G4 P3500\n;M721 S10000 E10000 P-15 I0 T11\n;G4 P800\n\nM104 [first_layer_temperature]\n\n; \\\\\\\\\\\\\\\\ END EXTRUDER 1 FOOTER/////////\n\n\n";"; \\\\\\\\\\\\\\\\ START EXTRUDER 1 FOOTER/////////\n\n;M721 S10000 E99999 P-15 I0 T11 ; takes 3.5 sec to complete ; Max value is 99999 and 10k\n;G4 P3500 ; time available in ms to complete previous commands\n;M721 S10000 E99999 P-15 I0 T11\n;G4 P3500\n;M721 S10000 E10000 P-15 I0 T11\n;G4 P800\n\nM104 [first_layer_temperature]\n\n; \\\\\\\\\\\\\\\\ END EXTRUDER 1 FOOTER/////////\n\n\n";"; \\\\\\\\\\\\\\\\ START EXTRUDER 1 FOOTER/////////\n\n;M721 S10000 E99999 P-15 I0 T11 ; takes 3.5 sec to complete ; Max value is 99999 and 10k\n;G4 P3500 ; time available in ms to complete previous commands\n;M721 S10000 E99999 P-15 I0 T11\n;G4 P3500\n;M721 S10000 E10000 P-15 I0 T11\n;G4 P800\n\nM104 [first_layer_temperature]\n\n; \\\\\\\\\\\\\\\\ END EXTRUDER 1 FOOTER/////////\n\n\n"

; end_gcode = \n\n; \\\\\\\\\\\\\\\\ START PRINTER FOOT/////////\n\nM104 S0 ; turn off temperature\nG0 Z100\n\nG28 X0 ; home X axis\nG28 Y0 ; home Z axis\nM84 ; disable motors\nG53 ; clear offsets\nM30 ; end\n\n; \\\\\\\\\\\\\\\\ END PRINTER FOOT/////////\n\n

; external_perimeter_acceleration = 0

; external_perimeter_extrusion_width = 0

; external_perimeter_speed = 100%

; external_perimeters_first = 1

; extra_loading_move = -2

; extra_perimeters = 0

; extra_perimeters_on_overhangs = 0

; extruder_clearance_height = 20

; extruder_clearance_radius = 20

; extruder_colour = #FF0000;#00FF00;#FF0000

; extruder_offset = 0x0,0x0,0x0

; extrusion_axis = E

; extrusion_multiplier = 1,1,1

; extrusion_width = 0

; fan_always_on = 0,0,0

; fan_below_layer_time = 60,60,60

; filament_colour = #1384C8;#1384C8;#1384C8
; filament_cooling_final_speed = 3.4,3.4,3.4
; filament_cooling_initial_speed = 2.2,2.2,2.2
; filament_cooling_moves = 4,4,4
; filament_cost = 0,0,0
; filament_density = 0,0,0
; filament_diameter = 1.75,1.75,1.75
; filament_load_time = 0,0,0
; filament_loading_speed = 28,28,28
; filament_loading_speed_start = 3,3,3
; filament_max_volumetric_speed = 0,0,0
; filament_minimal_purge_on_wipe_tower = 15,15,15
; filament_multitool_ramming = 0,0,0
; filament_multitool_ramming_flow = 10,10,10
; filament_multitool_ramming_volume = 10,10,10
; filament_notes = ;;
; filament_purge_multiplier = 100%,100%,100%
; filament_ramming_parameters = "120 100 6.6 6.8 7.2 7.6 7.9 8.2 8.7 9.4 9.9 10.0| 0.05 6.6 0.45 6.8 0.95 7.8 1.45 8.3 1.95 9.7 2.45 10 2.95 7.6 3.45 7.6 3.95 7.6 4.45 7.6 4.95 7.6";"120 100 6.6 6.8 7.2 7.6 7.9 8.2 8.7 9.4 9.9 10.0| 0.05 6.6 0.45 6.8 0.95 7.8 1.45 8.3 1.95 9.7 2.45 10 2.95 7.6 3.45 7.6 3.95 7.6 4.45 7.6 4.95 7.6";"120 100 6.6 6.8 7.2 7.6 7.9 8.2 8.7 9.4 9.9 10.0| 0.05 6.6 0.45 6.8 0.95 7.8 1.45 8.3 1.95 9.7 2.45 10 2.95 7.6 3.45 7.6 3.95 7.6 4.45 7.6 4.95 7.6"
; filament_settings_id = "FM-RM82 (Check Priming Parameters)";"FM-RM82 (Check Priming Parameters)";"FM-RM82 (Check Priming Parameters)"
; filament_soluble = 0,0,0
; filament_spool_weight = 0,0,0
; filament_stamping_distance = 0,0,0
; filament_stamping_loading_speed = 20,20,20
; filament_toolchange_delay = 0,0,0
; filament_type = PLA;PLA;PLA
; filament_unload_time = 0,0,0
; filament_unloading_speed = 90,90,90
; filament_unloading_speed_start = 100,100,100
; filament_vendor = (Unknown)
; fill_angle = 45
; fill_density = 0%
; fill_pattern = stars
; first_layer_acceleration = 0
; first_layer_acceleration_over_raft = 0
; first_layer_bed_temperature = 20,20,20
; first_layer_extrusion_width = 0

; first_layer_height = 0.03
; first_layer_speed = 100%
; first_layer_speed_over_raft = 30
; first_layer_temperature = 75,75,75
; full_fan_speed_layer = 0,0,0
; fuzzy_skin = none
; fuzzy_skin_point_dist = 0.8
; fuzzy_skin_thickness = 0.3
; gap_fill_enabled = 1
; gap_fill_speed = 20
; gcode_comments = 0
; gcode_flavor = repetier
; gcode_label_objects = disabled
; gcode_resolution = 0.001
; gcode_substitutions =
; high_current_on_filament_swap = 0
; host_type = prusalink
; idle_temperature = 25,25,25
; infill_acceleration = 0
; infill_anchor = 600%
; infill_anchor_max = 50
; infill_every_layers = 1
; infill_extruder = 1
; infill_extrusion_width = 0
; infill_first = 0
; infill_overlap = 25%
; infill_speed = 80
; interface_shells = 0
; ironing = 0
; ironing_flowrate = 15%
; ironing_spacing = 0.1
; ironing_speed = 15
; ironing_type = top
; layer_gcode = ; ====================
; layer_height = 0.03
; machine_limits_usage = time_estimate_only
; machine_max_acceleration_e = 10000,5000
; machine_max_acceleration_extruding = 1500,1250
; machine_max_acceleration_retracting = 1500,1250
; machine_max_acceleration_travel = 1500,1250
; machine_max_acceleration_x = 9000,1000

; machine_max_acceleration_y = 9000,1000
; machine_max_acceleration_z = 500,200
; machine_max_feedrate_e = 120,120
; machine_max_feedrate_x = 500,200
; machine_max_feedrate_y = 500,200
; machine_max_feedrate_z = 12,12
; machine_max_jerk_e = 2.5,2.5
; machine_max_jerk_x = 10,10
; machine_max_jerk_y = 10,10
; machine_max_jerk_z = 0.2,0.4
; machine_min_extruding_rate = 0,0
; machine_min_travel_rate = 0,0
; max_fan_speed = 100,100,100
; max_layer_height = 0.1,0.051,0.1
; max_print_height = 200
; max_print_speed = 80
; max_volumetric_extrusion_rate_slope_negative = 0
; max_volumetric_extrusion_rate_slope_positive = 0
; max_volumetric_speed = 0
; min_bead_width = 85%
; min_fan_speed = 35,35,35
; min_feature_size = 25%
; min_layer_height = 0.01,0.049,0.01
; min_print_speed = 10,10,10
; min_skirt_length = 0
; mmu_segmented_region_interlocking_depth = 0
; mmu_segmented_region_max_width = 0
; multimaterial_purging = 140
; notes =
; nozzle_diameter = 0.4,0.4,0.4
; only_retract_when_crossing_perimeters = 0
; ooze_prevention = 1
; output_filename_format = [input_filename_base].gcode
; overhang_fan_speed_0 = 0,0,0
; overhang_fan_speed_1 = 0,0,0
; overhang_fan_speed_2 = 0,0,0
; overhang_fan_speed_3 = 0,0,0
; overhang_speed_0 = 15
; overhang_speed_1 = 15
; overhang_speed_2 = 20
; overhang_speed_3 = 25

; overhangs = 1
; parking_pos_retraction = 92
; pause_print_gcode =
; perimeter_acceleration = 0
; perimeter_extruder = 1
; perimeter_extrusion_width = 0
; perimeter_generator = classic
; perimeter_speed = 6
; perimeters = 10000
; physical_printer_settings_id =
; post_process =
; print_settings_id = PrintSettings-RM82
; printer_model =
; printer_notes =
; printer_settings_id = PrinterSettings-RM82
; printer_technology = FFF
; printer_variant =
; printer_vendor =
; raft_contact_distance = 0.1
; raft_expansion = 1.5
; raft_first_layer_density = 90%
; raft_first_layer_expansion = 3
; raft_layers = 0
; remaining_times = 0
; resolution = 0.0005
; retract_before_travel = 10,2,2
; retract_before_wipe = 0%,0%,0%
; retract_layer_change = 0,0,0
; retract_length = 2,2,2
; retract_length_toolchange = 10,10,10
; retract_lift = 0,0,0
; retract_lift_above = 0,0,0
; retract_lift_below = 0,0,0
; retract_restart_extra = 0,0,0
; retract_restart_extra_toolchange = 0,0,0
; retract_speed = 40,40,40
; seam_position = rear
; silent_mode = 0
; single_extruder_multi_material = 0
; single_extruder_multi_material_priming = 1
; skirt_distance = 0.25

; skirt_height = 1
; skirts = 0
; slice_closing_radius = 0.0001
; slicing_mode = close_holes
; slowdown_below_layer_time = 5,5,5
; small_perimeter_speed = 100%
; solid_infill_acceleration = 0
; solid_infill_below_area = 70
; solid_infill_every_layers = 0
; solid_infill_extruder = 1
; solid_infill_extrusion_width = 0
; solid_infill_speed = 20
; spiral_vase = 0
; staggered_inner_seams = 0
; standby_temperature_delta = -50
; start_filament_gcode = "\n; \\\\\\\\\\\\\\\\ START EXTRUDER 1 HEADER //////////\nT0\n\nM109 S[first_layer_temperature] ; set temperature and wait for it to be reached\nM190 S[bed_temperature] L5 U10 ; Wait for the temperature of the bed to be 25 +- 2??C\n\nM6 T11 O1 X110 Y26 ; slot 1 (Input X,Y from tooloffset)\nM660 H0 Z???; Input Z from tooloffset\nM229 E0 D0; Ignore the E values and keep the same extrusion as in M221 (pulse)\nM221 P9000 S1.0 T11 Z[layer_height] W[nozzle_diameter]; set flow (Pn: Nb of motor pulses (extrusion speed), S: the flow multiplier, Wn: Width of the track (Nozzle Diameter), Zn: layer thickness, Tn: the head)\n\nG0 X0 Y0 ; goes to starting point X, Y\n\n; Priming of extruder 1/4th with one rotation\n;M722 S10000 E99999 P-15 I0 T11 ; takes 3.5 sec to complete ; Max value is 99999 and 10k\n;G4 P3500 ; time available in ms to complete previous commands\n;M722 S10000 E99999 P-15 I0 T11\n;G4 P3500\n;M722 S10000 E10000 P-15 I0 T11\nG4 3000\n\n; Turn off priming at the start of each layer and object\nM721 S1 E1 P1 T11 ; no prime\nM722 S1 E1 P1 T11 ; prime is ded\n\n; \\\\\\\\\\\\\\\\ END EXTRUDER 1 HEADER //////////\n\n";"\n; \\\\\\\\\\\\\\\\ START EXTRUDER 1 HEADER //////////\nT0\n\nM109 S[first_layer_temperature] ; set temperature and wait for it to be reached\nM190 S[bed_temperature] L5 U10 ; Wait for the temperature of the bed to be 25 +- 2??C\n\nM6 T11 O1 X110 Y26 ; slot 1 (Input X,Y from tooloffset)\nM660 H0 Z???; Input Z from tooloffset\nM229 E0 D0; Ignore the E values and keep the same extrusion as in M221 (pulse)\nM221 P9000 S1.0 T11 Z[layer_height] W[nozzle_diameter]; set flow (Pn: Nb of motor pulses (extrusion speed), S: the flow multiplier, Wn: Width of the track (Nozzle Diameter), Zn: layer thickness, Tn: the head)\n\nG0 X0 Y0 ; goes to starting point X, Y\n\n; Priming of extruder 1/4th with one rotation\n;M722 S10000 E99999 P-15 I0 T11 ; takes 3.5 sec to complete ; Max value is 99999 and 10k\n;G4 P3500 ; time available in ms to complete previous commands\n;M722 S10000 E99999 P-15 I0 T11\n;G4 P3500\n;M722 S10000 E10000 P-15 I0 T11\nG4 3000\n\n; Turn off priming at the start of each layer and object\nM721 S1 E1 P1 T11 ; no prime\nM722 S1 E1 P1 T11 ; prime is ded\n\n; \\\\\\\\\\\\\\\\ END EXTRUDER

1 HEADER //////////\n\n";"\n; \\\\\\\\\\\\\\\\ START EXTRUDER 1 HEADER //////////\nT0\n\nM109 S[first_layer_temperature] ; set temperature and wait for it to be reached\nM190 S[bed_temperature] L5 U10 ; Wait for the temperature of the bed to be 25 +- 2??C\n\nM6 T11 O1 X110 Y26 ; slot 1 (Input X,Y from tooloffset)\nM660 H0 Z???; Input Z from tooloffset\nM229 E0 D0; Ignore the E values and keep the same extrusion as in M221 (pulse)\nM221 P9000 S1.0 T11 Z[layer_height] W[nozzle_diameter]; set flow (Pn: Nb of motor pulses (extrusion speed), S: the flow multiplier, Wn: Width of the track (Nozzle Diameter), Zn: layer thickness, Tn: the head)\n\nG0 X0 Y0 ; goes to starting point X, Y\n\n; Priming of extruder 1/4th with one rotation\n;M722 S10000 E99999 P-15 I0 T11 ; takes 3.5 sec to complete ; Max value is 99999 and 10k\n;G4 P3500 ; time available in ms to complete previous commands\n;M722 S10000 E99999 P-15 I0 T11\n;G4 P3500\n;M722 S10000 E10000 P-15 I0 T11\nG4 3000\n\n; Turn off priming at the start of each layer and object\nM721 S1 E1 P1 T11 ; no prime\nM722 S1 E1 P1 T11 ; prime is ded\n\n; \\\\\\\\\\\\\\\\ END EXTRUDER 1 HEADER //////////\n\n"

; start_gcode = \n\n; \\\\\\\\\\\\\\\\ START PRINTER HEADER //////////\nM140 S[bed_temperature]\n\nG28 Z0 ; home Z \nG28 X0 Y0 ; home X/Y\n\n; Uncomment for UV pen on slot 3 (from the left) to expose the extrusion on port 1\n; To change the extrusion port here, change S11 to S1X, and to change the position of the UV pen, change T1X\n;M620 T13 E1 ; Turn on the UV Pen\n;M703 T13 S11 ; Duplicate commands between Head 4 and 1\n;M621 T13 P100 ; Set light emission tied to extrusion moves with power PXXX\n\n; \\\\\\\\\\\\\\\\ END PRINTER HEADER //////////\n\n

; support_material = 0

; support_material_angle = 0

; support_material_auto = 0

; support_material_bottom_contact_distance = 0

; support_material_bottom_interface_layers = -1

; support_material_buildplate_only = 0

; support_material_closing_radius = 2

; support_material_contact_distance = 0.2

; support_material_enforce_layers = 0

; support_material_extruder = 1

; support_material_extrusion_width = 0

; support_material_interface_contact_loops = 0

; support_material_interface_extruder = 1

; support_material_interface_layers = 3

; support_material_interface_pattern = rectilinear

; support_material_interface_spacing = 0

; support_material_interface_speed = 100%

; support_material_pattern = rectilinear

; support_material_spacing = 2.5

; support_material_speed = 5

; support_material_style = grid
; support_material_synchronize_layers = 0
; support_material_threshold = 0
; support_material_with_sheath = 1
; support_material_xy_spacing = 50%
; support_tree_angle = 40
; support_tree_angle_slow = 25
; support_tree_branch_diameter = 2
; support_tree_branch_diameter_angle = 5
; support_tree_branch_diameter_double_wall = 3
; support_tree_branch_distance = 1
; support_tree_tip_diameter = 0.8
; support_tree_top_rate = 15%
; temperature = 75,75,75
; template_custom_gcode =
; thick_bridges = 1
; thin_walls = 1
; thumbnails =
; thumbnails_format = PNG
; toolchange_gcode =
; top_fill_pattern = monotonic
; top_infill_extrusion_width = 0
; top_solid_infill_acceleration = 0
; top_solid_infill_speed = 15
; top_solid_layers = 3
; top_solid_min_thickness = 0
; travel_acceleration = 0
; travel_lift_before_obstacle = 0,0,0
; travel_max_lift = 0,0,0
; travel_ramping_lift = 0,0,0
; travel_slope = 0,0,0
; travel_speed = 45
; travel_speed_z = 15
; use_firmware_retraction = 0
; use_relative_e_distances = 0
; use_volumetric_e = 0
; variable_layer_height = 1
; wall_distribution_count = 1
; wall_transition_angle = 10
; wall_transition_filter_deviation = 25%
; wall_transition_length = 100%

```
        ; wipe = 0,0,0
        ; wipe_into_infill = 0
        ; wipe_into_objects = 0
        ; wipe_tower = 0
        ; wipe_tower_acceleration = 0
        ; wipe_tower_bridging = 10
        ; wipe_tower_brim_width = 2
        ; wipe_tower_cone_angle = 0
        ; wipe_tower_extra_flow = 100%
        ; wipe_tower_extra_spacing = 100%
        ; wipe_tower_extruder = 0
        ; wipe_tower_no_sparse_layers = 0
        ; wipe_tower_rotation_angle = 0
        ; wipe_tower_width = 60
        ; wipe_tower_x = 180
        ; wipe_tower_y = 140
        ; wiping_volumes_matrix = 0,140,140,140,0,140,140,140,0
        ; wiping_volumes_use_custom_matrix = 0
        ; xy_size_compensation = 0
        ; z_offset = 0
; prusaslicer_config = end
```

2024 Daniela Roque Tomé

SHAPE PROGRAMMING OF LIQUID CRYSTAL ELASTOMERS BY TWO-STAGE WAVELENGTH-SELECTIVE PHOTO-POLYMERISATION

NOVA SCHOOL OF SCIENCE & TECHNOLOGY